JETP Letters, Vol. 72, No. 7, 2000, pp. 357–359. Translated from Pis'ma v Zhurnal Éksperimental'noĭ i Teoreticheskoĭ Fiziki, Vol. 72, No. 7, 2000, pp. 513–517.

Disintegration of the Primordial ^{4}He by Electromagnetic Cascade in the Early Universe

E. B. Sedel'nikov

Institute of Mathematical Modeling, Russian Academy of Sciences, Miusskaya pl. 4a, Moscow, 125047 Russia

Received April 20, 2000; in final form, September 14, 2000

The results of calculations of ^{3}He + ^{3}H and D production through the disintegration of the primordial ^{4}He by electromagnetic cascade in the early Universe are presented. An electromagnetic cascade initiated by a high-energy particle and developing in cosmic plasma starts to disintegrate ^{4}He intensively after $t \sim 4 \times 10^4$ s. For certain parameters of the source (sorts of particles, energy, and time of appearance in the Universe), this mechanism dominates in the extra production of ^{3}He and ^{3}H. For example, an electromagnetic cascade originating from the thermal proton–antiproton annihilation is mainly responsible for the ^{4}He disintegration in a period of $\sim 4 \times 10^4$–5×10^8 s. © *2000 MAIK "Nauka/Interperiodica".*

PACS numbers: 98.80.Ft; 26.35.+c; 95.30.Cq

Disintegration of the primordial ^{4}He by electromagnetic cascade, along with disintegration by the secondary proton cascade, is the main mechanism of nonequilibrium cosmological nucleosynthesis (NCN). A hypothetical source of high-energy particles generates in the cosmic plasma of the early Universe electromagnetic and proton cascades which disintegrate the primordial ^{4}He into ^{3}He, ^{3}H, and D, thereby distorting the primordial chemical composition.

Recent calculations of the NCN caused by the nucleon–nucleus interactions are presented in [1]. The development of electromagnetic cascades in cosmic plasma has been studied rather well (see [2] and reference therein), and the relevant numerical calculations have been carried out (see, e.g., [3] and recent paper [4]). As part of continuing study of the NCN [1], this work reports the Monte Carlo simulation of the primordial ^{4}He disintegration by the electromagnetic cascade initiated by a high-energy particle source operating during a period of 10^2– 10^{16} s.

The number of nuclei of element A (^{3}He, ^{3}H or D) produced by the electromagnetic cascade can be represented in the form

$$n_A = \int\left(f_{\gamma\gamma}\frac{\sigma_{\gamma^4\mathrm{He}\to \mathrm{AX}} n_{^4\mathrm{He}}}{\Sigma_\gamma^{tot}} + f_{\gamma e}\frac{\sigma_{e^4\mathrm{He}\to \mathrm{AX}} n_{^4\mathrm{He}}}{\Sigma_e^{tot}}\right)dE,$$

where the functions $f_{\gamma\gamma}(E)$ and $f_{\gamma e}(E)$ describe the energy distributions of photons and electrons in the cascade initiated by a photon and $\Sigma_{\gamma(e)}^{tot}$ is the total cross section for photon (electron) interaction with plasma.

The central part in this process is played by the $\gamma\gamma \longrightarrow e^+e^-$, reaction of electron–positron pair production upon the interaction of energetic photons with the relict radiation (RR). The formed electron and positron transfer most of their energy to photons through the inverse Compton scattering by RR. As a result, the number of electrons and photons in the cascade grows in an avalanche-like manner. However, the disintegration of ^{4}He is suppressed by the $n_\gamma\sigma_{\gamma\gamma\to e^+e^-}$ term in Σ_γ^{tot}. Since the RR cools down as the Universe expands, the $\gamma\gamma \longrightarrow e^+e^-$ reaction threshold rises. At the instant it exceeds the ^{4}He disintegration threshold, the secondary photons start to intensively disintegrate helium. (Nevertheless, ^{4}He disintegration by the cascade electrons is still suppressed owing to the $n_\gamma\sigma_{e\gamma\to e\gamma}$ term in Σ_e^{tot}). This effect is illustrated in Fig. 1.

Jumps of ~8 orders of magnitude in the formation of ^{3}He + ^{3}H and in D (calculations were carried out with $n_\gamma/n_B = 10^8$) occur at slightly different times, because the thresholds of the $\gamma^4\mathrm{He} \longrightarrow {}^3\mathrm{He}n$, $\gamma^4\mathrm{He} \longrightarrow {}^3\mathrm{H}p$, and $\gamma^4\mathrm{He} \longrightarrow \mathrm{D}pn$ reactions are different. (A temporal difference caused by the difference in the thresholds of the two first reactions is of the order of the line thickness in Fig. 1). Deuterium is mainly formed by the $\gamma^4\mathrm{He} \longrightarrow \mathrm{D}pn$ reaction, because the cross section for the $\gamma^4\mathrm{He} \longrightarrow \mathrm{DD}$ reaction is considerably lower. It should be noted that the ^{4}He photodisintegration reactions have been studied rather well and a large body of relevant experimental data are available. The simulation was carried out using the results of works [5], where the coordinated data for all ^{4}He photodisintegration channels are presented.

It is seen from Fig. 1 that, not counting the jumpwise increase in the production of ^{3}He + ^{3}H and D upon achieving the threshold of the $\gamma\gamma \longrightarrow e^+e^-$ reaction, the

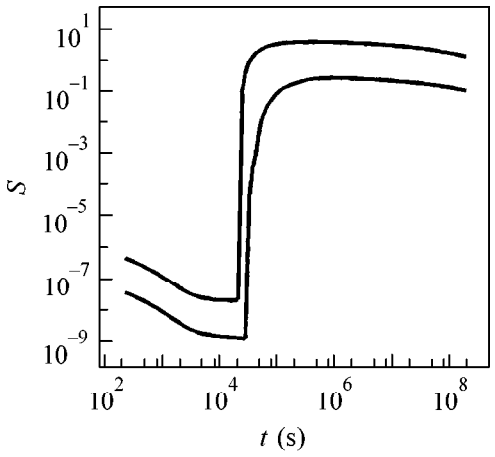

Fig. 1. Amounts of the (upper curve) ^{3}He + ^{3}H and (lower curve) D nuclei additionally produced by the electromagnetic cascade initiated by a photon with energy $E_\gamma = 20$ GeV vs. the time of cascade appearance in the Universe.

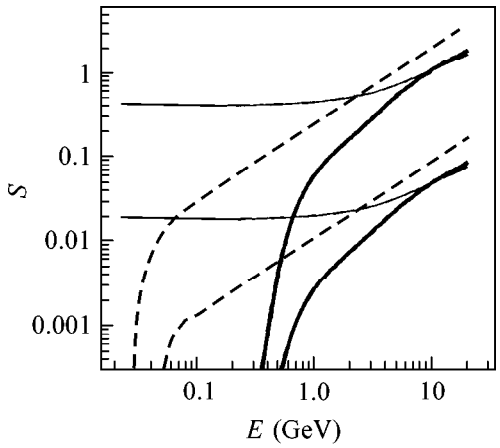

Fig. 2. Amounts of the (upper curves) ^{3}He + ^{3}H and (lower curves) D nuclei produced by the electromagnetic cascade initiated by (bold solid lines) proton, (thin solid lines) antiproton, and (dashed lines) photon vs. their energy for $t = 2 \times 10^5$ s.

number of produced nuclei decreases with aging of the Universe. This is caused by the specific features of electron scattering by RR. A typical energy of RR photons is κT. If $\kappa T/\sqrt{1-\beta^2} < m_e c^2$, where β is the velocity of the electron incident on RR, the inverse Compton scattering proceeds in the Thomson regime, for which the energy distribution of scattered photons can be taken to be uniform with a good accuracy. In the opposite case, the scattering proceeds in the Compton regime, for which the fraction of photons with scattering energy close to the electron energy increasingly grows. In the limiting regime, $\kappa T/\sqrt{1-\beta^2} \gg m_e c^2$, almost all protons acquire electron energy. As the Universe ages, the Compton regime of $e\gamma \longrightarrow e\gamma$ scattering grades (at a fixed electron energy) into the Thomson regime; i.e., all things being the same, the electromagnetic cascade becomes less energetic in the later Universe. The calculations were carried out using rigorous analytical formulas obtained in [6] for differential inverse Compton scattering by blackbody radiation.

If the initial particle is a proton or an antiproton, then, along with the secondary proton cascade, it also initiates the electromagnetic cascade, the higher the energy of the initial particle the greater the energy fraction transferred to the electromagnetic cascade. The amounts of produced ^{3}He + ^{3}H and D are shown in Fig. 2 as functions of the energies of the initial proton, antiproton, and photon (the electron and photon curves virtually coincide) for the time $t = 2 \times 10^5$ s.

A comparison of the curves in Fig. 2 with analogous curves obtained in [1] for the formation of light elements by the secondary proton cascade shows that the curves in Fig. 2 are steeper. Therefore, for a fixed energy of the initial proton or antiproton, the amount of ^{3}He + ^{3}H or D produced by the electromagnetic cascade will become greater than the analogous amount produced by the secondary proton cascade after a certain operation time of the source in the Universe. For ^{3}He + ^{3}H, this time comes considerably earlier than for D. This is due to the fact that, at energies ~75 MeV corresponding to the most intense disintegration of ^{4}He by the proton cascade, the $p^4\mathrm{He} \longrightarrow \mathrm{D}^3\mathrm{He}$ channel makes a considerable contribution to the inelastic cross section $\sigma^{inel}_{p^4\mathrm{He}}$, whereas the photodisintegration of ^{4}He mainly proceeds through the $\gamma^4\mathrm{He} \longrightarrow {}^3\mathrm{He}n$ and $\gamma^4\mathrm{He} \longrightarrow {}^3\mathrm{H}p$ channels; as to the deuterium production channels $\gamma^4\mathrm{He} \longrightarrow \mathrm{D}pn$ and $\gamma^4\mathrm{He} \longrightarrow \mathrm{DD}$, their sum is only a small fraction of the total photodisintegration cross section.

This point is important for cosmological applications. If the ^{4}He disintegration is due only to the secondary proton cascade, then $S_D/S_{^3\mathrm{He}+^3\mathrm{H}} = 0.55$ [1]. If the primordial ^{4}He is disintegrated only by the electromagnetic cascade, then the calculation gives $S_D/S_{^3\mathrm{He}+^3\mathrm{H}} = 0.08$. Thus, if the source operates in the Universe for a long time period, this ratio will change with time. In the general case, the final $S_D/S_{^3\mathrm{He}+^3\mathrm{H}}$ ratio of the additionally produced nuclei is determined by the sorts and energies of the particles ejected from the source, as well as by the moment at which the source appeared in the Universe and by the duration of its operation.

An interesting situation occurs if an antiproton is taken as the initial particle. At low antiproton energies (and at $t < 5 \times 10^8$ s), ^{4}He is disintegrated mainly by the electromagnetic cascade caused by annihilation on hydrogen nuclei, $\bar{p}p \longrightarrow \gamma\gamma$. As the energy increases

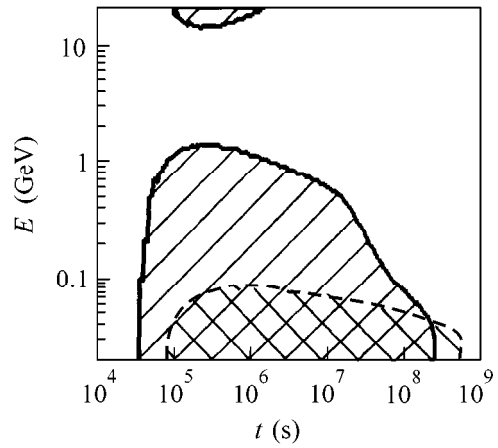

Fig. 3. The domains (shaded; the boundaries are shown by the solid lines) where ^{3}He + ^{3}H are mainly produced through ^{4}He disintegration by the electromagnetic cascade caused by antiproton annihilation on the hydrogen nuclei, $\bar{p}\,p \longrightarrow \gamma\gamma$. In the remaining domain, ^{3}He + ^{3}H are mainly produced through ^{4}He disintegration by the secondary proton cascade and through the annihilation on ^{4}He. The same is true for D, provided that the calculations are carried out with the minimum estimate [7] of the cross section for the $\bar{p}\,^4\mathrm{He} \longrightarrow \mathrm{D}X$ channel; the boundary is shown by the dashed line. The ordinate axis is the antiproton energy. The abscissa axis is the time of annihilation in the Universe.

(and depending on the cosmic time), the ^{4}He disintegration by the secondary proton cascade becomes dominant and, at still higher energies ($E_{\bar{p}} > 15$ GeV and depending on the cosmic time), the electromagnetic cascade again becomes dominant, because, as pointed out above, it absorbs an increasingly greater fraction of the energy of the initial particle (the same is also true for the initial proton). This is illustrated in Fig. 3. As the energy increases, the upper dashed domain expands to the right. A similar domain also appears for D, but it occurs at much higher energies.

Because of the uncertainty in the cross section for the $\bar{p}\,^4\mathrm{He} \longrightarrow \mathrm{D}X$ channel, one cannot determine with certainty to which mechanism—annihilation on helium or helium photodisintegration—dominates in the nonequilibrium production of deuterium at low antiproton energies. If one takes the maximum estimate for this cross section [7], then the low-energy domain of D photoproduction dominance (bounded by the dashed curve in Fig. 3) vanishes; in this case, deuterium is mainly produced through the annihilation on helium, $p^4\mathrm{He} \longrightarrow \mathrm{D}X$, and upon ^{4}He disintegration by the secondary proton cascade.

When calculating the extra production of the nuclei of light elements, one should take into account the mechanism of indirect deuterium production via the reaction $n + p \longrightarrow \mathrm{D}\gamma$. In this case, the neutrons, mainly appearing from the ^{4}He disintegration, have time to join with protons. This process is efficient at $t < 10^5\Omega_B^{2/3}$ s [8], after which the neutrons decay before the reaction.

The nonequilibrium ^{3}He, ^{3}H, and D nuclei appearing upon the disintegration of primordial ^{4}He interact with ^{4}He to produce ^{6,7}Li and ^{7}Be. Preliminary calculations [9] and estimates [10] indicate that lithium (especially ^{6}Li) is a more sensitive indicator of the nonequilibrium processes occurring in the early Universe than ^{3}He and D. Even greater information may be provided by the study of the dependence of the ratios [^{7}Li] : [^{6}Li] : [^{3}He] : [D] of the amounts of produced nuclei as functions of the composition and energy of the particles ejected by a hypothetical particle source and as functions of the source operation time in the Universe.

The reliable calculation of Li and Be production in the NCN encounters certain difficulties associated, first of all, with the lack of experimental data (see [1] for the details), though it holds a considerable interest.

I am grateful to E. I. Livanov for interest in the work and support.

REFERENCES

1. E. V. Sedel'nikov, Pis'ma Zh. Éksp. Teor. Fiz. **69**, 609 (1999) [JETP Lett. **69**, 645 (1999)].
2. R. Svensson and A. A. Zdziarski, Astrophys. J. **349**, 415 (1990); A. A. Zdziarski, Astrophys. J. **335**, 786 (1988).
3. R. J. Protheroe, T. Stanev, and V. S. Berezinsky, Phys. Rev. D **51**, 4134 (1995); S. Dimopoulos, R. Esmailzadeh, L. J. Hall, and G. D. Starkman, Astrophys. J. **330**, 545 (1988).
4. K. Jedamzik, Phys. Rev. Lett. **84**, 3248 (2000).
5. S. I. Nagornyĭ, Yu. A. Kasatkin, V. A. Zolenko, *et al.*, Yad. Fiz. **53**, 365 (1991) [Sov. J. Nucl. Phys. **53**, 228 (1991)]; Yu. M. Arkatov, P. I. Vatset, V. I. Voloshchuk, *et al.*, Yad. Fiz. **31**, 297 (1980) [Sov. J. Nucl. Phys. **31**, 157 (1980)]; Yu. M. Arkatov, P. I. Vatset, V. I. Voloshchuk, *et al.*, Pis'ma Zh. Éksp. Teor. Fiz. **28**, 710 (1978) [JETP Lett. **28**, 660 (1978)]; Yu. M. Arkatov, A. V. Bazaeva, P. I. Vatset, *et al.*, Yad. Fiz. **10**, 1123 (1969) [Sov. J. Nucl. Phys. **10**, 639 (1969)].
6. D. Fargion and A. Salis, Usp. Fiz. Nauk **168**, 909 (1998) [Phys. Usp. **41**, 823 (1998)].
7. F. Balestra, S. Bossolasco, M. P. Bussa, *et al.*, Nuovo Cimento A **100**, 323 (1988).
8. Ya. B. Zel'dovich, A. A. Starobinskiĭ, M. Yu. Khlopov, and V. M. Chechetkin, Pis'ma Astron. Zh. **3**, 208 (1977) [Sov. Astron. Lett. **3**, 110 (1977)].
9. E. V. Sedel'nikov, Yu. L. Levitan, and I. M. Sobol', Preprint No. 1, IMM RAN (Institute of Mathematical Modeling, Russian Academy of Sciences, 1996).
10. E. V. Sedel'nikov, Pis'ma Astron. Zh. **22**, 889 (1996) [Astron. Lett. **22**, 797 (1996)].

Translated by I. Roĭzen

JETP Letters, Vol. 72, No. 7, 2000, pp. 360–363. Translated from Pis'ma v Zhurnal Éksperimental'noĭ i Teoreticheskoĭ Fiziki, Vol. 72, No. 7, 2000, pp. 518–523.

Correlation Effects in Small-Angle Multiple Neutron Scattering

F. S. Dzheparov* and D. V. L'vov**

Institute of Theoretical and Experimental Physics, Bol'shaya Cheremushkinskaya ul. 25, Moscow, 117259 Russia

** e-mail: dzheparov@vitep5.itep.ru*

*** e-mail: lvov@vitep5.itep.ru*

Received July 24, 2000

The dependence of the spectra of small-angle multiple neutron scattering on the volume fraction occupied by scattering grains is considered. The concentration expansion is used to develop scattering theory in the eikonal approximation. The leading term of the expansion reproduces the standard low-concentration theory (Mollier). Some properties of the first correction term are analyzed, and it is shown that the angular distribution narrows with an increase in concentration, in qualitative agreement with the experimental data. © *2000 MAIK "Nauka/Interperiodica".*

PACS numbers: 61.12.Bt

1. Many of the properties of condensed materials are caused by the compositional inhomogeneities of supra-atomic sizes $a \sim (10^2–10^4)$ Å. Among these are phase precipitates, pores (voids), grains, dislocation clusters, etc. To gain information on these inhomogeneities, the small-angle neutron scattering (SANS) technique is widely used, because the typical single-scattering angle $\Delta\alpha = \Delta p/p$, as determined for thermal neutrons from the obvious relation $\Delta p \sim 1/a$, is $\Delta\alpha \sim (10^{-3}–10^{-5})$ rad.

The experiments on small-angle multiple neutron scattering (SAMNS) have naturally culminated in the studies of dense samples, in which the neutron mean free path $l_c = 1/c\sigma_t$ is comparable with the size a of an elementary scatterer (grain) having total cross section σ_t. Here, c is the number of grains in unit volume (their density or concentration) [1, 2]. The present-day theory of SAMNS pretends to an exhaustive description of the limit $l_c/a \gg 1$ [3, 4]. However, for higher number densities (and for closer l_c and a), the experiment shows sizable deviations from the predictions of this theory [1, 2].

It is the purpose of this work to use the concentration expansion technique [5] with the aim of generalizing the SAMNS theory to not-too-small concentrations. We consider the general features of the theory and demonstrate that the leading correction in the concentration expansion is on the order of $b = \frac{4}{3}\pi ca^3$ and, hence, may not be small even if $l_c \gg a$. The presence of this parameter in the theory may be evident even from the fact that the grains become spatially ordered at large ca^3 values, thereby cardinally changing the scattering spectrum in both quantum and classical cases.

2. The neutron-optical potential of a medium through which neutrons propagate can be written as

$$U(\mathbf{r}) = \sum_{\mathbf{x}} n_{\mathbf{x}} U_0(\mathbf{r} - \mathbf{x}, \alpha_{\mathbf{x}}), \qquad (1)$$

where $U_0(\mathbf{r}, \alpha)$ is the potential of a grain "centered" at $\mathbf{r} = \mathbf{0}$, $\alpha_{\mathbf{x}}$ is a complete set of "internal" parameters specifying the potential (in what follows, the index $\mathbf{x}$ at $\alpha_{\mathbf{x}}$ will be omitted), and $n_{\mathbf{x}}$ is the population of the $\mathbf{x}$ site [5]. It is assumed that the grain centers are positioned in the sites of a lattice with unit-cell volume Ω and that the average value $\langle n_{\mathbf{x}} \rangle = f$. In the $f \longrightarrow 0$, $\Omega \longrightarrow 0$, $f/\Omega = c$ = const limit, the grains are randomly distributed in a continuum space and the correlations in the grain distribution are described by the function $\Omega^{-2}\langle n_{\mathbf{x}} n_{\mathbf{y}} \rangle = C_2(\mathbf{x}, \mathbf{y}) \neq c^2$ [$C_2(\mathbf{x}, \mathbf{y})$ is the pair distribution function] and its straightforward generalizations to the high-order distribution functions.

In the eikonal approximation [6], which is usually sufficient for practical purposes, the scattering amplitude is

$$f(\mathbf{q}) = \frac{p_0}{2\pi i}\int d^2\rho [S(\boldsymbol{\rho}) - 1] \exp(-i\mathbf{q}\boldsymbol{\rho}), \qquad (2)$$

$$S(\boldsymbol{\rho}) = \exp\left(-i\int_{-\infty}^{\infty} \frac{dz}{v} U(\mathbf{r})\right), \quad \mathbf{r} = (\boldsymbol{\rho}, z).$$

In this expression, the momentum of the incident neutron is $\mathbf{p}_0 = (0, 0, p_0)$; v is the neutron velocity; ρ is the impact parameter; $\mathbf{q}$ is the scattering momentum, $\mathbf{q}\mathbf{p}_0 = 0$; and $q \ll p_0$.

The normalized angular distribution of neutron momentum is

$$D(\mathbf{q}) = \Sigma(\mathbf{q})/\Sigma_0, \quad \Sigma(\mathbf{q}) = |f(\mathbf{q})|^2, \qquad \Sigma_0 = \int d^2q\Sigma(\mathbf{q}). \tag{3}$$

As usual, it is assumed that $\Sigma(\mathbf{q})$ is concentrated at small q, so that the limits of integration in Eq. (3) (and further) are taken to be infinite. The theoretical analysis can conveniently be carried out for the Fourier transform

$$D(\boldsymbol{\xi}) = \Sigma(\boldsymbol{\xi})/\Sigma_0, \quad \Sigma(\boldsymbol{\xi}) = \int d^2q\exp(-i\mathbf{q}\boldsymbol{\xi})\Sigma(\mathbf{q}), \qquad \Sigma_0 = \Sigma(\boldsymbol{\xi} = \mathbf{0}). \tag{4}$$

It is clear that

$$\Sigma(\boldsymbol{\xi}) = p_0^2\int d^2\rho[S(\boldsymbol{\rho} - \boldsymbol{\xi}/2) - 1][S^+(\boldsymbol{\rho} + \boldsymbol{\xi}/2) - 1] = p_0^2\int d^2\rho[S(\boldsymbol{\rho} - \boldsymbol{\xi}/2)S^+(\boldsymbol{\rho} + \boldsymbol{\xi}/2) - 1] + \Sigma_0. \tag{5}$$

Next we will assume that the sample sizes are large enough for $\Sigma(\mathbf{q})$ to be considered as a self-averaging quantity in a system with a random grain distribution [i.e., $\Sigma(\mathbf{q}) = \langle\Sigma(\mathbf{q})\rangle$] and evaluate

$$\Delta\Sigma(\boldsymbol{\xi}) = \langle\Sigma(\boldsymbol{\xi}) - \Sigma_0\rangle. \tag{6}$$

Making use of Eqs. (1), (2), and (6) and writing $\mathbf{r} = (\boldsymbol{\rho}, z)$, one gets

$$\Delta\Sigma(\boldsymbol{\xi}) = p_0^2\int d^2\rho\left[\left\langle \exp\left(\sum_{\mathbf{x}} n_{\mathbf{x}}R_{\mathbf{x}}(\boldsymbol{\rho}, \boldsymbol{\xi}, \alpha)\right)\right\rangle - 1\right], \tag{7}$$

$$R_{\mathbf{x}}(\boldsymbol{\rho}, \boldsymbol{\xi}, \alpha) = -i\int_{-\infty}^{\infty}\frac{dz}{V}[U_0(\mathbf{r} - \mathbf{x} - \boldsymbol{\xi}/2, \alpha) - U_0(\mathbf{r} - \mathbf{x} + \boldsymbol{\xi}/2, \alpha)]. \tag{8}$$

Ignoring boundary effects,

$$\Delta\Sigma(\boldsymbol{\xi}) = p_0^2S_s\left[\left\langle \exp\left(\sum_{\mathbf{x}} n_{\mathbf{x}}R_{\mathbf{x}}(\mathbf{0}, \boldsymbol{\xi}, \alpha)\right)\right\rangle - 1\right]. \tag{9}$$

Here, S_s is the cross-sectional area of the sample.

Note that in the classical limit

$$R_{\mathbf{x}}(\boldsymbol{\rho}, \boldsymbol{\xi}, \alpha) \longrightarrow R_{\mathbf{x}}^{cl}(\boldsymbol{\rho}, \boldsymbol{\xi}, \alpha) = i\boldsymbol{\xi}\int_{-\infty}^{\infty}\frac{dz}{V}\frac{\partial U_0(\mathbf{r} - \mathbf{x}, \alpha)}{\partial\mathbf{r}}.$$

3. Let us first consider a system with an uncorrelated random grain distribution. In this case, the exact result can be obtained using the relationship

$$\left\langle \exp\left(\sum_{\mathbf{x}} n_{\mathbf{x}}R_{\mathbf{x}}\right)\right\rangle = \exp\left[c\int_V d^3x\left\langle e^{R_{\mathbf{x}}} - 1\right\rangle_\alpha\right], \tag{10}$$

which is valid in the continuum limit [5] for the $R_{\mathbf{x}}$ function of a rather general form. In Eq. (10), V is the sample volume and $\langle\ldots\rangle_\alpha$ stands for the averaging over the internal grain parameters, which are assumed to be distributed independently for different grains.

Averaging in Eq. (9) with the use of Eq. (10) gives

$$\Delta\Sigma(\boldsymbol{\xi})/p_0^2S_s + 1 = \exp[cl\int d^2\rho\langle\exp(R_{\boldsymbol{\rho}}(\mathbf{0}, \boldsymbol{\xi}, \alpha)) - 1\rangle_\alpha] = \exp[-cl(\sigma_0 - \sigma(\boldsymbol{\xi}))/p_0^2], \tag{11}$$

where $l \gg a$ is the sample thickness and $\sigma(\boldsymbol{\xi})$ and $\sigma_0 = \sigma(\boldsymbol{\xi} = 0) = p_0^2\sigma_t$ are analogous to $\langle\Sigma(\boldsymbol{\xi})\rangle$ and $\langle\Sigma_0\rangle$ in the single-scattering case. As in Eq. (5), the Fourier transform of the single-scattering differential cross section is

$$\sigma(\boldsymbol{\xi}) = \int d^2q\exp(-i\mathbf{q}\boldsymbol{\xi})\sigma(\mathbf{q}) = p_0^2\left\langle\int d^2\rho[S_0(\boldsymbol{\rho} - \boldsymbol{\xi}/2)S_0^+(\boldsymbol{\rho} + \boldsymbol{\xi}/2) - 1]\right\rangle_\alpha + \sigma_0.$$

Here,

$$S_0(\boldsymbol{\rho}) \equiv S_0(\boldsymbol{\rho}, \alpha) = \exp\left(-i\int_{-\infty}^{\infty}\frac{dz}{V}U_0(\mathbf{r}, \alpha)\right).$$

Therefore, one has for the uncorrelated grain distribution

$$D(\boldsymbol{\xi}) = \frac{p_0^2S_s\exp(-cl(\sigma_0 - \sigma(\boldsymbol{\xi}))/p_0^2)}{\Sigma_0} + \frac{\Sigma_0 - p_0^2S_s}{\Sigma_0}.$$

The spectrum of scattered neutrons can be analyzed using the function

$$D(\boldsymbol{\xi}) = D_0(\boldsymbol{\xi}) = \exp[-cl(\sigma_0 - \sigma(\boldsymbol{\xi}))/p_0^2]. \tag{12}$$

The two formulas presented above for $D(\boldsymbol{\xi})$ differ only in the fraction of nonscattered neutrons. Equation (12) coincides with the standard result of the Mollier theory valid in the limit of low grain concentration.

4. For a high grain concentration, the many-body distribution function cannot be factorized into a product of one-particle functions, so that one cannot directly pass from Eq. (9) to Eq. (11). Nevertheless, according to the general cumulant expansion theory [7], one has to expect that, if the correlation in grain distribution vanishes with increasing distance, then

$$D(\boldsymbol{\xi}) = \exp(-lM(\boldsymbol{\xi}, l)),$$

where $M(\boldsymbol{\xi}, l)$ tends to a finite value as $l \longrightarrow \infty$. In this case, it is natural to expand $D(\boldsymbol{\xi})$ in powers of occupa-

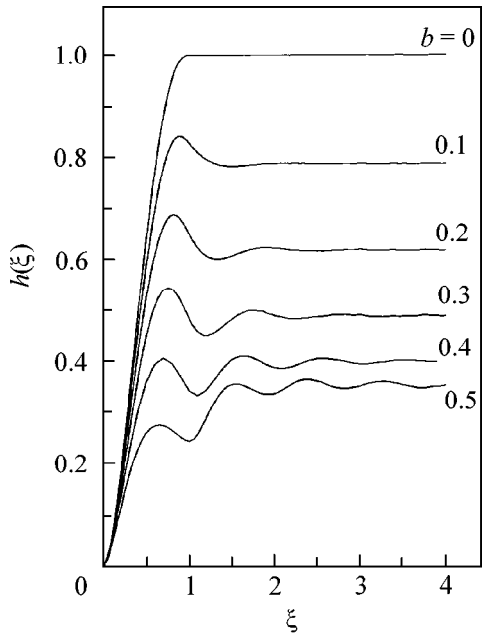

Fig. 1. The function $h(\xi)$ determined from Eq. (21) for different grain specific volumes $b = (4\pi/3)ca^3$, where c is the grain concentration.

tion numbers following the rule [5]

$$\exp\left(\sum_{\mathbf{x}} n_{\mathbf{x}} R_{\mathbf{x}}\right) = \prod_{\mathbf{x}} [1 + n_{\mathbf{x}}(e^{R_{\mathbf{x}}} - 1)] \tag{13}$$

$$= 1 + \sum_{\mathbf{x}} n_{\mathbf{x}}(e^{R_{\mathbf{x}}} - 1) + \frac{1}{2}\sum_{\mathbf{x}\neq\mathbf{y}} n_{\mathbf{x}} n_{\mathbf{y}}(e^{R_{\mathbf{x}}} - 1)(e^{R_{\mathbf{y}}} - 1) + \ldots$$

Introducing $Q_{\mathbf{x}}(\boldsymbol{\xi}, \alpha) = \exp(R_{\mathbf{x}}(0, \boldsymbol{\xi}, \alpha)) - 1$ and averaging Eq. (13) term by term over the occupation numbers and α distribution, one obtains in the continuum limit

$$\left\langle \exp\left(\sum_{\mathbf{x}} n_{\mathbf{x}} R_{\mathbf{x}}\right)\right\rangle = \exp(B),$$

$$B = c\int d^3x \langle Q_{\mathbf{x}}\rangle_\alpha + \frac{c^2}{2}\int d^3x d^3y \kappa(\mathbf{x}, \mathbf{y})\langle Q_{\mathbf{x}} Q_{\mathbf{y}}\rangle_\alpha \tag{14}$$

$$+ \frac{c^2}{2}\int d^3x d^3y (\langle Q_{\mathbf{x}} Q_{\mathbf{y}}\rangle_\alpha - \langle Q_{\mathbf{x}}\rangle_\alpha \langle Q_{\mathbf{y}}\rangle_\alpha) + O(c^3).$$

Here,

$$C_2(\mathbf{x}, \mathbf{y}) = c^2(\kappa(\mathbf{x}, \mathbf{y}) + 1). \tag{15}$$

One can see that, when applied to $D(\boldsymbol{\xi})$, these relationships reproduce $D_0(\boldsymbol{\xi})$ by the first (linear in c) term in B.

5. Let us consider the results given by Eqs. (11) and (14) for the case when the grains are identical spheres with radius a. Setting

$$U_0(\mathbf{r}, \alpha) = U_0\vartheta(r < a), \tag{16}$$

where $\vartheta(z) = 1$ if condition z is true and $\vartheta(x) = 0$ otherwise, and taking into account that there is no internal variable α, one obtains

$$D(\boldsymbol{\xi}) = D(\xi_1, \xi_2) = D_0(\boldsymbol{\xi})\exp\left[\frac{c^2 l}{2}(K(\boldsymbol{\xi}) + O(c))\right],$$

$$K(\boldsymbol{\xi}) = \int d^2x \int d^2y \bar{\kappa}(|\mathbf{x} - \mathbf{y}|) Q_{\mathbf{x}}(\boldsymbol{\xi}) Q_{\mathbf{y}}(\boldsymbol{\xi}),$$

$$\bar{\kappa}(x) = \int_{-\infty}^{\infty} dz \kappa(\sqrt{x^2 + z^2}), \tag{17}$$

$$Q_{\mathbf{x}}(\boldsymbol{\xi}) = e^{-i\phi(\mathbf{x} - \boldsymbol{\xi}/2) + i\phi(\mathbf{x} + \boldsymbol{\xi}/2)} - 1,$$

$$\phi(x) = \frac{2U_0}{v}\sqrt{a^2 - x^2}\vartheta(x < a).$$

Note that, if the Born parameter $\nu = U_0 a/v$ is small, then the leading and the first correction terms in Eq. (17) are on the order of ν^2, while the next terms are of a higher order in ν. Consequently, we arrive at the complete solution of the SAMNS problem for a sample with small ν and finite effective thickness $l_e = l/l_c \propto \nu^2 l$.

A detailed analysis of the pair correlation function in the model of hard spheres was carried out for simple liquids in [8]. We will use the generalized Percus–Yewick model [9], which is in excellent agreement with the molecular dynamics computations. In [9], the $\kappa(r)$ function was calculated for the grain specific volume $b = 0.1$–0.5. This function was found to have the form $\kappa(x) = -\vartheta(x < 2a) + \vartheta(2a < x)f(x)$. The first term in this expression accounts for the sphere hardness, while the second one accounts for the effective attraction that is well known from the theory of pair correlation functions [10]. It has a rather simple statistical origin. Indeed, introducing

$$\Delta n(\mathbf{k}) = n(\mathbf{k}) - \langle n(\mathbf{k})\rangle, \quad n(\mathbf{k}) = \sum_{\mathbf{x}} \exp(-i\mathbf{k}\mathbf{x}) n_{\mathbf{x}}$$

and using the obvious relation $\langle|\Delta n(\mathbf{k})|^2\rangle \geq 0$, one finds that the $\kappa(\mathbf{k}) = \int d^3x \exp(-i\mathbf{k}\mathbf{x})\kappa(\mathbf{x})$ value should satisfy condition

$$1 + c\kappa(\mathbf{k}) \geq 0. \tag{18}$$

If the sphere hardness is only taken into account, i.e., if $f(\mathbf{x}) = 0$, then condition (18) breaks even at $(4\pi/3)c(2a)^3 > 1$, i.e., at $b > 1/8$. Thus, condition (18) places rather strong limits on the allowed models of $\kappa(\mathbf{x})$ correlations at large b values.

The angular distribution in the experiments with double crystal spectrometers is given by a single Fourier transform [2]:

$$I(q) = \frac{1}{\pi}\int_0^{\infty} d\xi \cos(q\xi) D(\xi, 0) = I_s\delta(q) + I_r(q), \tag{19}$$

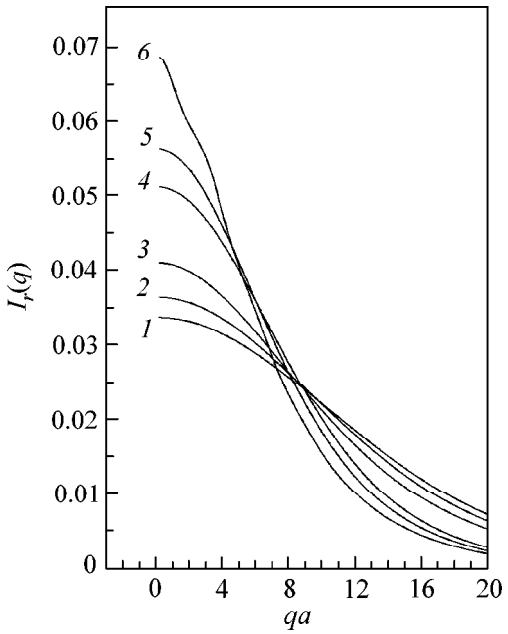

Fig. 2. Intensity $I_r(q)$ of scattered neutrons for samples with the Born parameter $\nu = 0.2$, effective thickness $l_e = l/l_c$, and different grain concentrations. (*1*) $l_e = 40$ and $b = 0$; (*2*) $l_e = 40$ and $b = 0.3$; (*3*) $l_e = 40$ and $b = 0.5$; (*4*) $l_e = 20$ and $b = 0$; (*5*) $l_e = 20$ and $b = 0.3$; and (*6*) $l_e = 20$ and $b = 0.5$.

where $I_r(q)$ is a smooth function and the fraction of nonscattered neutrons is

$$I_s = \exp\left(-\frac{l}{l_c}h_\infty\right), \qquad h_\infty = 1 - cK(\xi \longrightarrow \infty)/(2\sigma_t). \tag{20}$$

The Fourier transform of intensity $D(\xi, 0)$ can be conveniently written in the form

$$D(\xi, 0) = \exp\left(-\frac{l}{l_c}h(\xi)\right). \tag{21}$$

The $h(\xi)$ values are presented in Fig. 1 for different scatterer concentrations. The calculated functions show oscillations, because the pair correlation function oscillates. The $h_\infty = h(\xi \longrightarrow \infty)$ value corresponding to the intensity I_s of the nonscattered neutrons strongly depends on the concentration; namely, it changes from $h_\infty(b = 0) = 1$ to $h_\infty(b = 0.5) \approx 0.35$. The angular distributions of neutrons, as determined from Eqs. (17) and (19), are presented in Fig. 2 for effective thicknesses $l_e = l/l_c = 20$ and $l_e = 40$ corresponding to experiment [1]. One can see that the angular distribution narrows with increasing concentration at a fixed l/l_c. Such a narrowing was experimentally observed in SAMNS on Al powders [1].

We are grateful to H. Glättli, V.K. Ignatovich, and the authors of [1] for helpful discussions. This work was supported by the Russian Foundation for Basic Research, project nos. 00-02-17837 and 00-15-96656.

REFERENCES

1. Yu. G. Abov, Yu. I. Smirnov, D. S. Denisov, *et al.*, in *Proceedings of the National Conference on Application of X-rays, Synchrotron Radiation, Neutrons, and Electrons for Researching Materials, RSNÉ*, Dubna, 1997, Vol. 2, p. 115.
2. Yu. G. Abov, D. S. Denisov, F. S. Dzheparov, *et al.*, Zh. Éksp. Teor. Fiz. **114**, 2194 (1998) [JETP **87**, 1195 (1998)].
3. S. V. Maleev and B. P. Toperverg, Zh. Éksp. Teor. Fiz. **78**, 315 (1980) [Sov. Phys. JETP **51**, 158 (1980)].
4. S. G. Bogdanov and A. Z. Men'shikov, Zh. Éksp. Teor. Fiz. **117**, 122 (2000) [JETP **90**, 109 (2000)].
5. F. S. Dzheparov, V. S. Smelov, and V. E. Shestopal, Pis'ma Zh. Éksp. Teor. Fiz. **32**, 51 (1980) [JETP Lett. **32**, 47 (1980)].
6. L. D. Landau and E. M. Lifshitz, *Quantum Mechanics: Non-Relativistic Theory* (Nauka, Moscow, 1989, 4th ed.; Pergamon, Oxford, 1977, 3rd ed.).
7. R. Kubo, J. Phys. Soc. Jpn. **17**, 1100 (1962).
8. G. N. Sarkisov, Usp. Fiz. Nauk **169**, 625 (1999).
9. R. O. Watts and D. Henderson, Mol. Phys. **16**, 217 (1969).
10. R. Balescu, *Equilibrium and Nonequilibrium Statistical Mechanics* (Wiley, New York, 1975; Mir, Moscow, 1978).

Translated by V. Sakun

JETP Letters, Vol. 72, No. 7, 2000, pp. 364–368. From Pis'ma v Zhurnal Éksperimental'noĭ i Teoreticheskoĭ Fiziki, Vol. 72, No. 7, 2000, pp. 524–529.

Dust Particle Charging and Formation of Dust Structures in the Upper Atmosphere[1]

B. A. Klumov, S. I. Popel, and R. Bingham*

Institute of Geosphere Dynamics, Russian Academy of Sciences, Leninskiĭ pr. 38-6, Moscow, 117979 Russia

** Rutherford Appleton Laboratory, Chilton, Didcot, Oxfordshire, OX 11 OQX, UK*

Received August 17, 2000

We investigate the dust particle charging process in the Earth's upper atmosphere. Calculating the spectra of solar radiation, we study the influence of the photoelectric effect on the charging process. We show that both positively and negatively charged dust particles are present in the upper atmosphere. We consider the mechanisms which can be responsible for the formation of dust structures like noctilucent clouds and polar mesosphere summer echoes. © *2000 MAIK "Nauka/Interperiodica".*

PACS numbers: 94.10.-s; 52.25.Zb; 92.60.Nv

Earth's upper atmosphere reveals some layered structures which are known as noctilucent clouds (NLC) and polar mesosphere summer echoes (PMSE). These structures are believed to be associated with the presence of a large amount of charged dust or aerosol in the upper atmosphere. The problem of formation of dust structures in the Earth's upper atmosphere is considered now in the dusty plasma community as one of the key problems. Furthermore, the great interest in these structures is due to their possible connection with the Earth's global warming process.

NLC probably consist of particles of icy nature. Their appearance is confined to the summer season at the mesospheric altitudes close to 80–85 km at high- and midlatitudes, when the temperature drops down below about 155 K, [e.g., 1]. Under these conditions, the formation of ice particles occurs. Polar mesosphere summer echoes are strong radar echoes which also appear to be associated with dust [2]. PMSE occur in well-defined layers in the 80- to about 95-km altitude region [3]. Because NLC and PMSE are observed at the same season and at the altitude region close to the mesopause, one can assume that NLC and PMSE have the same origin. Both NLC and PMSE are small-scale mesospheric structures. Their width L_c is far less than the height scale H of the atmosphere: $L_c \ll H$; $L_c \simeq$ 100 m–1 km, and $H \approx 7$ km. Many questions remain to be answered about NLC and PMSE, the most important one being the width of the structures.

In this study, we propose the model of NLC as a layer of a charged dusty plasma illuminated by solar radiation [4]. We calculate spectra of solar radiation at NLC altitudes, determine charges of the dust particles, and analyze the possibilities of the formation of dust particle structures. For brevity, the mesospheric dust structures are referred to as "NLC".

We choose the following parameters of the mesosphere and dust particles: the characteristic dust particle size is $a \sim 10^{-7}$–10^{-5} cm, the dust number density is $n_d \sim 10$–10^3 cm^{-3}, the altitudes of NLC formation are $h \simeq 82$–83 km, the width of NLC is $L_c \sim 100$ m–1 km, the vertical optical depth is $L \ll 1$, the neutral number density is $n_n \simeq 2 \times 10^{14}$ cm^{-3}, the water vapor number density is $n_w \sim (10^8$–$10^9)$ cm^{-3}, and the temperature of neutrals is $T_n \leq 155$ K.

The mesospheric ion composition is rather complicated [5]. Different sorts of both positive and negative ions are present. Here, we take into account only positive ions[2] of two kinds. The first one is related to light primary ions like NO^+, N_2^+, O_2^+ and the second one to the so-called proton hydrate ions (PHs) ($H^+(H_2O)_n$, $n \leq 10$). We note that the electron–ion recombination coefficient α_{rec} depends strongly on the kind of ions.

[1] This article was submitted by the authors in English.

[2] The role of the negative ions at NLC altitudes can be evaluated in the following manner. The primary negative ion is O_2^-. The ion is created via the process $e + 2O_2 \longrightarrow O_2^- + O_2$ (the rate constant is $k_1 \simeq 5 \times 10^{-31}$ cm^6 s^{-1}). Main sinks of the O_2^- ion are (a) photodetachment O_2^- + photon $\longrightarrow O_2 + e$ (the rate constant is $\delta_{photo} \sim 0.3$ s^{-1}) and (b) collisional destruction $O_2^- + O \longrightarrow O_2 + O + e$ (the rate constant is $k_2 \simeq 3 \times 10^{-10}$ cm^3 s^{-1}). Balancing the processes, we can easily estimate the O_2^- concentration at NLC altitudes: $[O_2^-] \sim k_1[O_2]^2 n_e/(\delta_{photo} + k_2[O]) \sim 0.1$–$1$ cm^{-3}. This value is far less than the positive ion number density. Thus, we can neglect the role of the negative ions in the mesospheric dust charging process.

The light primary ions have the effective recombination coefficient $\alpha^p_{rec} \sim 10^{-7}$ cm^3 s^{-1}, while $\alpha^c_{rec} \sim 10^{-5}$ cm^3 s^{-1} for PHs ions. Here and below, the superscripts *p* and *c* refer to the primary and PHs ions, respectively.

The temperatures of ions and electrons are believed to be equal to the neutral temperature $T_i = T_e = T_n$. The ionization rate is $q_e \sim 0.1$–10 cm^{-3} s^{-1}.

We have calculated the solar spectra at NLC altitudes using Phodis code [6]. Figure 1 shows the spectrum variations with altitude and solar zenith angle. It is clearly seen that the typical solar spectrum decreases sharply for the wavelengths less than approximately 170 nm (which corresponds to the photon energy ≈7.3 eV), where the cutoff of energetic photons occurs.

The work function of pure ice is about 8.9 eV. Thus, taking into account the form of the solar spectrum at NLC altitudes, we conclude that the photoelectric effect is not significant in the charging process of pure ice grains. However, if (even ice) dust particles contain impurities, then the work function of the substance of the dust can be much less than the cutoff of the solar spectrum. In this case, the photoelectric effect can be very important (even dominant) in the charging process. The effect leads to the existence of both positively and negatively charged dust particles in the mesosphere.

Even under twilight conditions, the solar flux is large enough that the ionization rate due to the photoelectric effect can be comparable to the value of q_e and even greater than this value. In this case, it is necessary to include the photoelectric effect to determine charges of the dust particles in NLC. We note that solar radiation does not affect (with electron production) all dust particles. The origin of the dust particle appears to play the crucial role in the effect. It is believe that the dust grain is created in the cold summer mesosphere via two different mechanisms. (a) The base for the grain creation is the PHs ion. The $H^+(H_2O)_n$ ions are effective seeds for the nucleation processes in the mesosphere [7]. In this case, the dust grain likely consists of pure ice. (b) The base for the grain creation is a small dust particle of meteoritic or volcanic eruption nature. In this case, the grains consist of contaminated ice, so that the photoelectric work function can be reduced significantly for such particles. In both cases, the growth of the dust particle is due to fast absorption of water molecules by the particle.

To evaluate dust particle charging under NLC conditions, we use the model which describes the evolution of the electron density n_e; of the ion density of both kinds n^p_i, n^c_i; and of the dust charge variation. Neglecting the chemistry of negative ions and using the local approximation, we present the set of equations which describes the dust particle charge in the following form:

$$\frac{\partial n_e}{\partial t} = q_e + \sum_j q_{photo,\,j} n^j_d - \sum_j \nu_{e,\,j} n^j_d - \alpha^p_{rec} n_e n^p_i - \alpha^c_{rec} n_e n^c_i,$$

$$\frac{\partial n^p_i}{\partial t} = q_e - \sum_j \nu^p_{i,\,j} n^j_d - \alpha^p_{rec} n_e n^p_i - \beta_c n^p_i,$$

$$\frac{\partial n^c_i}{\partial t} = \beta_c n^p_i - \sum_j \nu^c_{i,\,j} n^j_d - \alpha^c_{rec} n_e n^c_i,$$

$$\frac{\partial Z_{d,\,j}}{\partial t} = q_{photo,\,j} + \nu^p_{i,\,j} + \nu^c_{i,\,j} - \nu_{e,\,j}.$$

Here ν_e, ν_i are the charging rates due to electron and ion collisions with dust particles, q_{photo} is the charging rate due to the photoelectric effect, β_c is the rate of conversion of the primary ions into the PHs ions, and the index *j* describes the dust particles of different sizes. The typical values of β_c under NLC conditions are $\beta_c \sim 0.1$ cm^3/s [7]. In the case of the negative dust charge, we have [8]

$$\nu_e \approx -\pi a^2 (8T_e/\pi m_e)^{1/2} n_e \exp(eq_d/aT_e),$$

$$\nu_i = \sqrt{\frac{\pi}{2}} a^2 v_{Ti} e n_i \left[2\exp\left\{ -\frac{v_i^2}{2v_{Ti}^2} \right\} + \frac{\sqrt{2\pi}(1 + v_i^2/v_{Ti}^2)\,\mathrm{erf}\{v_i/\sqrt{2}v_{Ti}\}}{v_i/v_{Ti}} - \frac{2eq_d}{am_i v_{Ti}^2} \frac{\sqrt{2\pi}\,\mathrm{erf}\{v_i/\sqrt{2}v_{Ti}\}}{v_i/v_{Ti}} \right].$$

For the situation of the positive dust charge, the charging rates are [9]

$$\nu_e \approx -\pi a^2 (8T_e/\pi m_e)^{1/2} n_e (1 + eq_d/aT_e),$$

$$\nu_i = \sqrt{\frac{\pi}{2}} a^2 v_{Ti} n_i \left\{ 2\exp\left(-\frac{v_i^2 + v^2_{\min,\,i}(q_d)}{2v_{Ti}^2} \right) \times \cosh\left(\frac{v_i v_{\min,\,i}(q_d)}{v_{Ti}^2} \right) + \sqrt{\frac{\pi}{2}} \frac{v_{Ti}}{v_i} \left(1 + \frac{v_i^2}{v_{Ti}^2} - \frac{2eq_d}{am_i v_{Ti}^2} \right) \times \left[\mathrm{erf}\left(\frac{v_{\min,\,i}(q_d) + v_i}{\sqrt{2}v_{Ti}} \right) - \mathrm{erf}\left(\frac{v_{\min,\,i}(q_d) - v_i}{\sqrt{2}v_{Ti}} \right) \right] \right\}.$$

In the above formulas, $q_d = -Z_d e$ is the dust particle average charge, $-e$ is the electron charge, $v_{\min,\,i}(q_d) = (2eq_d/am_i)^{1/2}$, m_α is the mass of the particle of the kind α, and erf(x) is the error function.

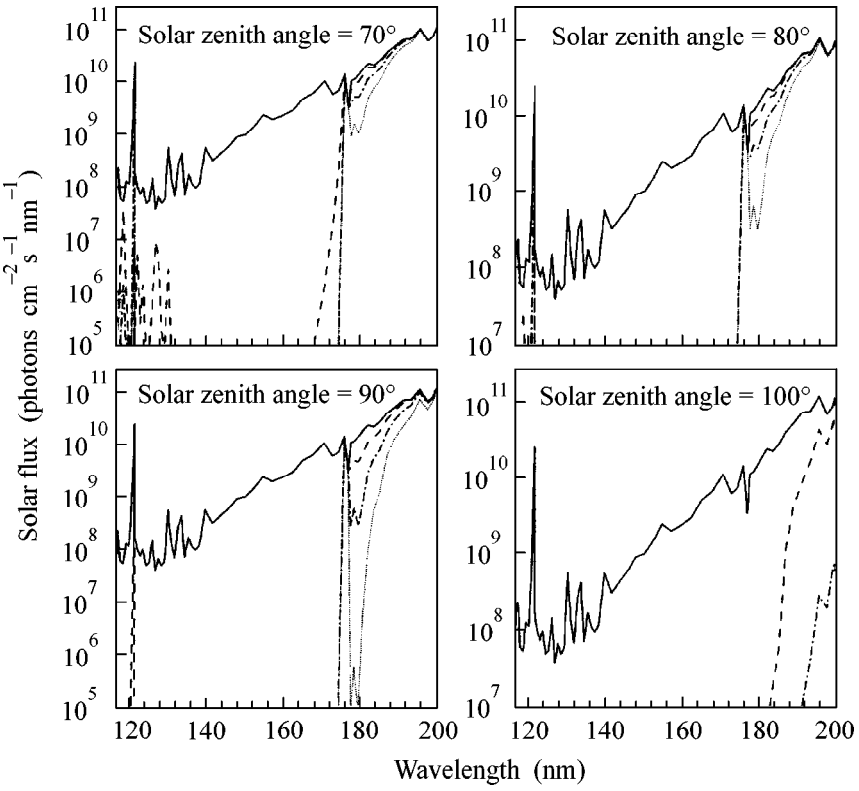

Fig. 1. Solar spectra at mesospheric altitudes for various solar zenith angles. Spectra correspond to the altitude of (solid line) 100 km, (dashed line) 90 km, (dash–dotted line) 80 km, and (dotted line) 70 km.

The photoelectric rate q_{photo} is given by the formula

$$q_{photo} = \frac{\pi\beta a^2}{\hbar} \int\limits_{\omega_R - (e^2 Z_d/a\hbar)}^{\infty} \frac{\Phi(\omega)}{\omega} d\omega.$$

Here, $\Phi(\omega)$ is the solar flux at the mesospheric altitudes, β is the probability of emission of an electron under the action of one photon on the dust particle surface, $\hbar$ is Planck's constant, and $\hbar\omega_R$ is the photoelectric work function. The limits of integration correspond to the fact that only photons with frequencies $\omega > \omega_R - (e^2 Z_d/a\hbar)$ can result in photoelectric current generation (i.e., the electrons emitted due to the action of these photons can go away from the dust grain surface to infinity). In our case, $\hbar\omega_R$ is equal to several eV, while $e^2 Z_d/a \sim kT_n \sim 0.01$ eV $\ll \hbar\omega_R$. Thus, the dependence of the lower limit of the integral on the dust particle charge is negligible.

Figure 2 shows the temporal dependences of the ion and electron number densities and the dust charge variation for two different ionization rates $q_e = 0.1$ cm^{-3} s^{-1} and $q_e = 10$ cm^{-3} s^{-1}. The dust parameters are $n_d \simeq 10^3$ cm^{-3} and $a \simeq 10^{-5}$ cm for both cases.

In the steady state and in the absence of charged dust particles, the densities of electrons and ions at NLC altitudes are determined by the ionization rate q_e and the mean recombination coefficient α_{rec}: $n_e \simeq n_i \simeq \sqrt{q_e/\alpha_{rec}}$. To take into account both day and night conditions, the initial time is chosen just before twilight. When the dust particles immerse into the mesosphere, they acquire the charges q_d, which can be positive even under twilight conditions, the charges being negative at night. The typical values of q_d for NLC parameters are $q_d/e \sim$ 10–20 during the day and at twilight and $q_d/e \simeq -2$ at night.

As it is mentioned above, NLC is accompanied by the presence of dust particles and, moreover, they can be associated with dust layers. Significant electron depletion occurs in the region occupied by the dust particles at night. The presence of solar radiation results in significant depletion of ions, the magnitude of the electron density in this case being larger than the equilibrium one. The depletions create the diffusion fluxes of electrons (ions) on the dust layer at night (day) time. We note that both positively and negatively charged dust grains and the corresponding depletions were observed in the polar summer mesosphere [e.g., 10]. We believe that the depletions play a definite role in the process of NLC formation.

Let us consider the spatial evolution of the dusty layer under the mesospheric conditions. For simplicity, we assume that the dust particles have the same sizes. Below, we omit the index j in the equations.

We use the one-dimensional model (the x axis is directed downward), which is to some extent analogous to the model of a self-organizing dusty layer [11] but has important differences from the latter model. In our case, the dusty layer can be charged both positively and negatively, depending on solar zenith angle. If the dusty layer is charged positively, then the significant depletion of ions inside the layer occurs and the diffusive ion flux affects the dusty layer. Furthermore, the negatively charged pure ice particles tend to squeeze the dusty layer. If the layer is charged negatively (at night), the depletions of electrons and ions appear and the layer (being under the action of the fluxes of electrons and ions) also have a tendency to squeeze. To describe the spatial evolution of such a dusty layer, we use the continuity equation for the dust particles, the local approximation for both electrons and ions, and the Poisson equation. The local approximation gives four nonlinear algebraic equations:

$$q_e + q_{photo} n_d = \nu_e n_d + \alpha^p_{rec} n_e n_i^p + \alpha^c_{rec} n_e n_i^c,$$

$$q_e = \nu_i^p n_d + \alpha^p_{rec} n_e n_i^p + \beta_c n_i^p,$$

$$\beta_c n_i^p = \alpha^c_{rec} n_e n_i^c, + \nu_i^c n_d,$$

$$q_{photo} + \nu_i^p + \nu_i^c = \nu_e.$$

The lifetime of electrons (ions) $\tau_{e(i)}$ is mainly determined by the charging process $\tau_{e(i)} \sim \nu^{-1}_{e(i)}$. The lifetime $\tau_{e(i)}$ is far less than the characteristic diffusion time $\tau_d^{e(i)}$, where $\tau_d^{e(i)} \sim L_c^2/D_{e(i)} \sim L_c^2 n_n \sigma_n^{e(i)}/v_{e(i)}$, $\sigma_n^{e(i)}$ is the cross section for elastic collisions between electrons (ions) and neutrals. Thus, the local approximation is suitable under NLC conditions.

Using the assumption of the stationary dust particle structure, we present the continuity equation for the dust particles in the form

$$\partial(n_d u_d)/\partial x = \nu_d n_d.$$

Here, the term $\nu_d n_d$ describes the accretion processes. We note that the existence of both positively and negatively charged dust particles accelerates the accretion processes.

For the dust particles, we take into account the momentum transfer in collisions with other dust particles, ions, and neutrals (the momentum transfer in collisions with electrons is negligibly small):

$$m_d n_d u_d \frac{\partial u_d}{\partial x}$$

$$= -eZ_d n_d \frac{\partial \varphi}{\partial x} - \nu_i m_i n_i (u_i - u_d) + m_d n_d g,$$

where φ is the electrostatic potential, u_α is the velocity of particles of the kind α, and g is the gravity.

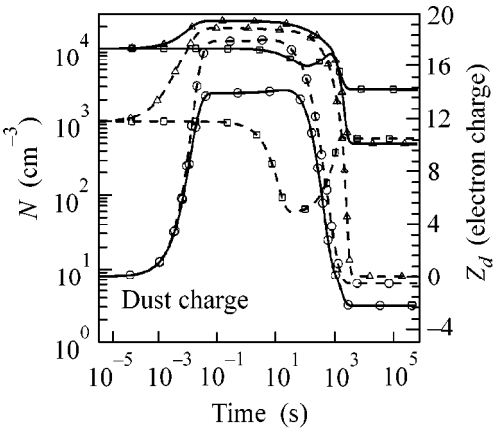

Fig. 2. Ions (square), electron (triangle) number densities, and dust charge (circle) variations versus time in the polar summer mesosphere. Solid and dashed lines correspond to various (10^3 cm^{-3} and 10^4 cm^{-3}) initial plasma densities, respectively. The dust number density is $n_d \simeq 10^3$ cm^{-3}, and the dust size is $a \simeq 10^{-5}$ cm. The dust photoelectric work function is 7 eV.

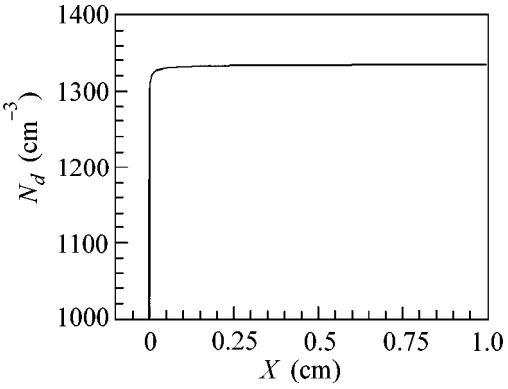

Fig. 3. Spatial dependence of the dust number density showing sharp boundary of NLC.

The Poisson equation takes the form

$$\partial^2\varphi/\partial x^2 = 4\pi e(n_e + Z_d n_d - n_i).$$

Assuming that the dust particles have zero velocity, we can evaluate the electric fields in the mesosphere under NLC conditions:

$$E_x = -\partial\varphi/\partial x \simeq m_d g/eZ_d \sim 1 \text{ V/m}.$$

We note that such electric fields were observed in the lower mesosphere and in the vicinity of NLC [12]. Figure 3 shows the spatial structure of the dust layer calculated on the basis of the above set of equations. We note that the dust structure has sharp boundaries.

As for the width L_c of NLC, this value can be estimated as $L_c \sim v_\alpha/\nu_{\alpha,d}$, where v_α is the velocity of the charged particles of the kind α, $\nu_{\alpha,d}$ is the particle–dust collision rate {it is assumed that the fluxes of particles

of the kind α result in the squeezing of the dusty layer (cf. [11])}. For electrons and ions, it gives $L_c \sim d_{e,i}^2/a$. Under the mesospheric conditions, $L_c \sim 10^5$ cm. This value is of the order of the observable width of NLC. The scaling will be discussed in more detail in following publications.

The solar spectrum at NLC altitudes has a cutoff at wavelengths shorter than ≃170 nm due to atmospheric absorption of solar radiation. Since the photoelectric work function for the dust particles varies strongly (from about a few eV for contaminated dust up to about 9 eV for pure ice) depending on the particle origin, we conclude that there are both positively and negatively charged dust particles in the polar summer mesosphere. This fact can be important both for NLC formation and for the understanding of the nature of V/m mesospheric electric fields.

Charging of the dust particles results in significant electron depletion at nighttime, while significant ion depletion occurs in the daytime and even at twilight. In both cases, the diffusive fluxes of electrons and ions are created, the fluxes having a tendency to squeeze the dusty layer. We have shown that the mesospheric dusty layers have sharp boundaries and their width is of the order of the observable width of NLC.

This work was supported in part by INTAS (grant no. 97-2149) and INTAS-RFBR (grant no. IR-97-775).

REFERENCES

1. J. N. Cho and J. Röttger, J. Geophys. Res. **102** (D2), 2001 (1997).
2. J. Havnes *et al.*, J. Geophys. Res. **101** (A5), 10839 (1996).
3. V. Nussbaumer *et al.*, J. Geophys. Res. **101** (D14), 19161 (1996).
4. O. Havnes *et al.*, J. Atmos. Terr. Phys. **52**, 637 (1990).
5. G. C. Reid, J. Geophys. Res. **94**, 14653 (1989).
6. A. Kylling, http://kaja.gi.alaska.edu.
7. T. Sigiyama, J. Geophys. Res. **99**, 3915 (1994).
8. S. I. Popel *et al.*, Phys. Plasmas **3**, 4313 (1996).
9. S. I. Popel *et al.*, Phys. Plasmas **7**, 2410 (2000).
10. F. Balsiger *et al.*, Geophys. Res. Lett. **23**, 93 (1996).
11. V. N. Tsytovich, Com. Plasma Physics Contr. Fus., Part C **1**, 41 (1999).
12. A. M. Zadorozhny *et al.*, Geophys. Res. Lett. **20**, 2299 (1993).

JETP Letters, Vol. 72, No. 7, 2000, pp. 369–372. Translated from Pis'ma v Zhurnal Éksperimental'noĭ i Teoreticheskoĭ Fiziki, Vol. 72, No. 7, 2000, pp. 530–535.

Dipolar Broadening and Exchange Narrowing of EPR Lines from the Paramagnetic Centers Distributed on a Solid Surface

V. A. Atsarkin*, G. A. Vasneva*, V. V. Demidov*,, F. S. Dzheparov***, B. M. Odintsov*,****, and R. B. Clarkson******

** Institute of Radio Engineering and Electronics, Russian Academy of Sciences, Mokhovaya ul. 11, Moscow, 103907 Russia*

*** e-mail: demidov@mail.cplire.ru*

**** Institute of Theoretical and Experimental Physics, Bol'shaya Cheremushkinskaya ul. 25, Moscow, 117259 Russia*

***** Illinois Research EPR Center, University of Illinois, Urbana, IL 61801, USA*

Received September 5, 2000

Experiments with char samples provide support for the theory of EPR line shape in a system of surface paramagnetic centers with dipole–dipole interactions. It is also demonstrated that, if a strong Heisenberg exchange dominates over the dipole–dipole interactions, the EPR line of a two-dimensional system narrows and acquires Lorentzian shape, similar to the three-dimensional case. © *2000 MAIK "Nauka/Interperiodica".*

PACS numbers: 76.20.+q; 76.30.-v

The problem of magnetic resonance line shape is too extensive to list all the works published over a period of decades. Restricting oneself to electron paramagnetic resonance in nonconducting solids, one can cite, as an example, the works on the line shape in magnetically diluted systems with dipole–dipole interactions between the paramagnetic centers (PCs) [1–3]. However, the cited works refer to three-dimensional systems. As to the experimental studies on the line shapes in diluted two-dimensional systems with dipole–dipole interactions, we did not find relevant data in the literature. At the same time, study of the two-dimensional case is not an abstract exercise. The EPR spectra of stable free radicals in developed porous structures, such as activated carbons and other catalysts, are rather popular examples for demonstrating the two-dimensional distribution of paramagnetic impurities. In particular, chars obtained by pyrolysis of various carbon-containing materials have been much investigated in recent years [4]. These chars in an oxygen-free medium give exceedingly narrow EPR lines with widths strongly depending on the concentration of surrounding oxygen over a very wide range [5]. It is these materials which are dealt with in this work. The EPR line shape of the impurity PCs distributed on a solid surface (i.e., two-dimensional system) is consistently studied in the work.

To describe line shape in the magnetically diluted systems, Anderson's model [6] is widely used, in which only the *z–z* part of the total dipole–dipole interaction is taken into account. For the random distribution of spins in a space of dimensionality D = 1, 2, and 3, a simple expression [7] is obtained for the free induction decay curve $S(t)$:

$$S(t) = S_0 \exp[-(t/T_2)^{D/3}], \quad (1)$$

where T_2 is the transverse relaxation time. As is known [6], the absorption line shape $g(\omega)$ is the Fourier transform of the free induction decay:

$$g(\omega) = \int_{-\infty}^{\infty} S(t)\exp(i\omega t)dt/2\pi S_0. \quad (2)$$

General analysis [2, 3] shows that Anderson's model rigorously reproduces line wings and satisfactorily describes its central portion. For strongly diluted three-dimensional systems, Eq. (2) gives a Lorentzian shape but one fails to deduce an analytical expression for the two-dimensional case. In [8], an analytical expression is presented only for a far wing of the line; for D = 2, it decreases as $\omega^{-5/3}$.

For the quantitative comparison of Eqs. (1) and (2) with experiment, it is necessary to know the explicit expression for T_2. In the D = 2 case of interest, this expression depends on the angle θ_p between the external magnetic field **H** and the normal $\mathbf{n_p}$ to the plane in which the paramagnetic centers are situated. In [7], the corresponding expression was obtained only for $\theta_p = 0$, whereas our experimental conditions require the averaging over the random orientations of the chars surface. To solve this problem, let us turn back to the original premises in the theoretical calculations of Anderson's model.

0021-3640/00/7207-0369$20.00

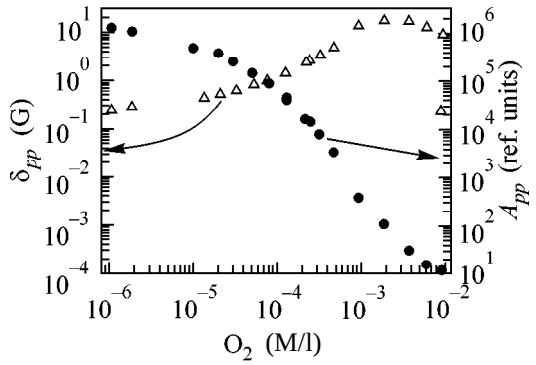

Fig. 1. (△) Separation between the peaks and (●) peak-to-peak amplitude in the derivative of the EPR line of carbonized fructose as functions of the concentration of ambient oxygen.

The standard method of calculation [2] yields the following general expression:

$$F_D(t) \equiv S(t)/S_0$$

$$= \exp\left(-n_D\int d^D r\left\{1-\cos\left[\frac{b_0 t}{r^3}P_2(\theta)\right]\right\}\right),$$

where $b_0 = 3\gamma^2\hbar^2/2$, $P_2(\theta) = (3\cos^2\theta - 1)/2$, θ is the angle between $\mathbf{r}$ and $\mathbf{H}_0$, and n_D is the D-dimensional density of PCs. In the two-dimensional case,

$$F_2(t) = \exp\left(-n_2\int d^2 r\left\{1-\cos\left[\frac{b_0 t}{r^3}P_2(\theta)\right]\right\}\right)$$

$$= \exp(-n_2(b_0 t)^{2/3}J_1(\theta_p)J_2).$$

The last expression in this formula is obtained by the substitution of integration variable $r \longrightarrow r|(b_0 t P_2(\theta))|^{1/3}$, and

$$J_1(\theta_p) = \int_0^{2\pi} d\varphi|P_2(\theta)|^{2/3},$$

$$J_2 = \int_0^{\infty} r dr\left[1-\cos\left(\frac{1}{r^3}\right)\right] = \Gamma\left(\frac{1}{3}\right)/4.$$

The $F_2(t, \theta_p)$ function can only be numerically calculated. It is convenient to direct the in-plane x axis along $\mathbf{n}_x = [\mathbf{n}_p\mathbf{H}]/|[\mathbf{n}_p\mathbf{H}]|$ and set $\mathbf{n}_y = [\mathbf{n}_p\mathbf{n}_x]$. Defining an arbitrary in-plane vector as $\mathbf{r} = \mathbf{r}(\cos\varphi, \sin\varphi)$, one obtains $\cos\theta = \sin\varphi\sin\theta_p$. Now, averaging over the plane orientations yields

$$\langle J_1\rangle = \frac{1}{2}\int_0^{\pi}\sin\theta_p d\theta_p J_1(\theta_p) = 3.173,$$

and $\delta J_1^2 = \langle(J_1 - \langle J_1\rangle)^2\rangle/\langle J_1\rangle^2 = 0.164$. The relative smallness of the latter value allows one to use further the simple formula

$$F_2(t) = \exp(-n_2(b_0 t)^{2/3}\langle J_1(\theta_p)\rangle J_2) = \exp(-(\beta_2 t)^{2/3})$$

coinciding with Eq. (1) for $D = 2$, with

$$\beta_2 = T_2^{-1} = 4.64 n_2^{3/2}\gamma^2\hbar, \qquad (3)$$

where γ is the gyromagnetic ratio. Equations (1)–(3) provide a basis for the subsequent processing of the experimental data.

Experiments were carried out with carbonized carbon-containing natural materials prepared at the University of Illinois (Urbana–Champaign, USA) by the method described in [4]. Powder samples with particle sizes 75–100 μm were placed in quartz cells with controlled pressure of ambient air. This allowed the EPR line shapes to be determined as functions of the concentration c of surrounding oxygen over a very wide range (several orders of magnitude) of c values. The EPR spectra were recorded at room temperature. The concentration of paramagnetic centers was determined from a comparison of the EPR line area with a signal from one of the Mn^{2+} HFS components of a reference MgO:Mn sample placed in the same cavity but outside the cell containing the sample under study. The experimental data presented below refer to the sample of carbonized fructose with PC concentration $n = 1.07 \times 10^{20}$ g^{-1} and mass $m = 3.6 \times 10^{-3}$ g. Similar results were also obtained for other chars [9].

The peak-to-peak width δ^{pp} and amplitude A_{pp} of the derivative of EPR line are shown in Fig. 1 as functions of the concentration of ambient oxygen. Examples of EPR spectra are presented in Fig. 2 for air pressures $P = 1$ and 1.07×10^{-3} bar, which corresponds to the ambient oxygen concentrations $c = 9.3 \times 10^{-3}$ and 10^{-5} M/l, respectively. One can see from Figs. 1 and 2 that the pressure variation drastically changes the separation, the amplitude, and the EPR line shape. At the same time, our measurements showed that the PC concentration remained constant in these experiments. The dependence of EPR spectra on the concentration of ambient oxygen is reversible, with the time of establishing stationary state not exceeding 1 s.

It is seen from Fig. 2a that the experimental EPR spectrum at $c = 9.3 \times 10^{-3}$ M/l ($P = 1$ bar) is described well by the sum of two lines corresponding to the two-dimensional spatial distribution of paramagnetic impurities with dipole–dipole interactions between them. The same figure illustrates an attempt at fitting the experimental spectrum by the sum of two Lorentzian curves typical of the three-dimensional spatial distribution of the paramagnetic centers with dipolar interactions. One can clearly see that the two-dimensional description provides much better agreement with the experiment.

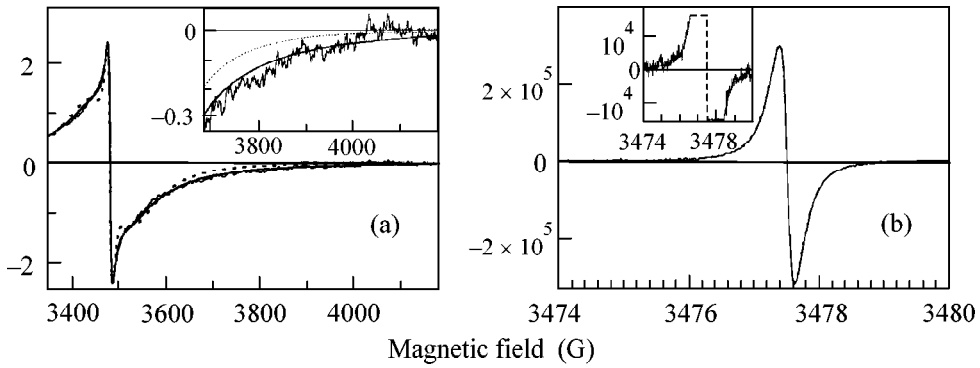

Fig. 2. Experimental EPR signals and curve fitting for carbonized fructose at the concentrations of ambient oxygen c = (a) 9.3×10^{-3} and (b) 10^{-5} M/l. Solid lines are the sums of two "two-dimensional" curves with dipole–dipole interactions between the PCs [see Eq. (1)]; dots are the sums of two Lorentzian curves. Far wings of the signal are shown in the insets.

The two-dimensional fit proved to be successful only for high concentrations of ambient oxygen ($c > 10^{-3}$ M/l), whereas at low concentrations ($c < 10^{-3}$ M/l) the experimental spectrum was nicely described by the sum of two Lorentzians (Fig. 2b).

The agreement between the experimental EPR line shape and the theoretical models was checked by using the chi-square test, i.e., by the degree of correspondence to the standard condition $\chi^2 = m \pm (2m)^{1/2}$ [10], where m is the number of experimental points. Note that an even better description of the two-dimensional (2D) experimental data is achieved with the model [3, 11] allowing for both the disorder in the PC distribution and, in the simplest form, the flip-flop transitions between the PCs. In this case,

$$F_D(t) = \exp(-(\Phi(t))^{D/6}),$$

$$\Phi(t) = 2\beta_D^2 \int_0^t d\tau (t-\tau) f(\tau), \quad f(\tau) = \exp(-\kappa\tau).$$

The curve fitting yields $\kappa \approx 0.05\beta_2$. Although such a small κ value cannot be considered as a direct estimate of the flip-flop rate, it is in line with the previous theoretical conclusion [3] that the flip-flop processes only slightly modify Anderson's free induction decay in the three-dimensional systems.

The two curves used for the interpretation of the experimental spectra correspond to the presence of two types of PCs, *A* and *B*. Their nature was discussed in detail in our work [9]. We merely note here that the *A* centers are affected by the adsorbed oxygen more strongly than the *B* centers are. As c increases, the fraction of *A* increases, while that of *B* decreases, with the sum of their concentrations being unchanged. Note that the observed mutual transformation of the two PC types is one more piece of evidence of their surface nature.

It is remarkable that the EPR line is exceedingly narrow at a low content of ambient oxygen. The estimates of the magnetic dipole–dipole broadening for the PC concentration used in our experiment give a value of no less than 10 G. However, the measured values (Fig. 1) are an order of magnitude smaller. This can naturally be explained by the exchange narrowing. This hypothesis is consistent with the Lorentzian shapes observed for the *A* and *B* lines at low oxygen concentrations (see above). It is well known that the strong (compared to the dipolar interactions) exchange leads to the Lorentzian shapes of EPR lines in ordinary three-dimensional systems [6]. One can show that the exchange interaction brings about the same result for the two-dimensional PC distribution. In this case, the transition from the Lorentzian curves to the dipolar broadening occurring for 2D at $c > 10^{-3}$ M/l can naturally be explained by the distortion of PC orbitals under the action of adsorbed oxygen molecules and the ensuing collapse of the exchange interaction between the PCs (for details, see our work [9]).

Figure 3 shows the variation of the T_2 parameter for the curves describing the experimental EPR spectra over the whole range of oxygen concentrations. It is of interest to compare the curves in Figs. 1 and 3. In the first case, the extreme point is clearly seen at $c = 2 \times 10^{-3}$ M/l, whereas in the latter case both dependences are monotonic. The fact is that the relationship between δ^{pp} and T_2 is given by

$$\delta_{Lor}^{pp} = \left(\frac{\sqrt{3}}{2}\gamma T_2\right)^{-1} \quad (4)$$

for the Lorentzian curve and

$$\delta_2^{pp} = (2.54\gamma T_2)^{-1} \quad (5)$$

for the 2D curve determined by Eq. (3). It is seen from Eqs. (4) and (5) that, for the same T_2, the difference between the peaks in the derivative of the two-dimensional EPR line is tangibly smaller than for the Lorentzian curve.

Let us use the model described above and make some quantitative estimates for this sample. One can see in Fig. 3 that the T_2 time for the *B*-type centers

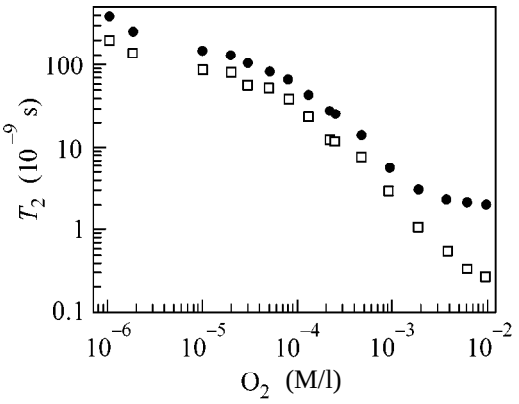

Fig. 3. The T_2 value as a function of the concentration of ambient oxygen; (□) are for the *A* centers, and (●) are for the *B* centers.

ceases to depend on the adsorption of oxygen molecules after the collapse of exchange narrowing and takes the value $T_2 = 2.0 \times 10^{-9}$ s. It is natural to assume that this value is caused by the dipole–dipole interactions between the PCs. Then, using Eq. (3), one arrives at the $n_2(\text{PC}) = 0.48 \times 10^{14}$ cm^{-2} estimation for the surface number density of PCs. With the known total PC concentration (see above), it is straightforward to determine the specific surface area occupied by all PCs: $S_\Sigma = 220$ m^2/g. The resulting S_Σ value agrees well with the estimates made in [12] ($S_\Sigma \sim 100$ m^2/g), where this quantity was determined for analogous samples independently by the adsorption methods. Moreover, the fact that the experimental spectrum coincides with the two-dimensional model up to detunings of a hundred widths (Fig. 2a) indicates that $r_{av}/100^{1/3}$ is as small as 3.2 Å. This value is comparable with the interatomic distances; consequently, all PCs belong to the surface layer.

As to the centers of type *A*, their transverse relaxation, as can be judged from the line shape, is also due to the dipole–dipole interactions, but the T_2 value continues to decrease with increasing number of adsorbed oxygen molecules. Therefore, one can assume that the dipole–dipole interactions of the *A* centers with the adsorbed oxygen molecules [having orbital magnetic moment $\mu(O_2) = 2.84\mu_B$] sizably contribute to the transverse relaxation of these centers. Estimates by Eq. (3) indicate that the oxygen surface concentration at atmospheric pressure is on the order of $n_2(O_2) = 0.9 \times 10^{14}$ cm^{-2}, which seems to be quite reasonable for the adsorption of oxygen molecules on the surface of carbons under normal conditions [13].

Summarizing the results of this study, one can draw the following conclusions. The experiments with paramagnetic centers distributed over the surface and coupled via the dipole–dipole interactions confirm theoretical predictions about the EPR line shapes in such systems. In the presence of a strong Heisenberg exchange dominating over the dipole–dipole interactions, the EPR line in a two-dimensional system narrows and acquires the Lorentzian shape, similar to the three-dimensional case.

We are grateful to Paul Siroki from the University of Illinois (Urbana, USA) for sample preparation. This work was supported by the Russian Foundation for Basic Research (project nos. 99-02- 16024 and 99-02-17440B) and the Fogarty International Foundation (grant no. 1RO3 TW00998-01).

REFERENCES

1. P. W. Anderson, Phys. Rev. **82**, 342 (1951).
2. F. S. Dzheparov, A. A. Lundin, and T. N. Khazanovich, Zh. Éksp. Teor. Fiz. **92**, 554 (1987) [Sov. Phys. JETP **65**, 314 (1987)].
3. F. S. Dzheparov, I. V. Kaganov, and E. K. Khenner, Zh. Éksp. Teor. Fiz. **112**, 596 (1997) [JETP **85**, 325 (1997)].
4. F. P. Auteri, R. L. Belford, and R. B. Clarkson, Appl. Magn. Reson. **6**, 287 (1994).
5. S. J. Boyer and R. B. Clarkson, Colloids Surf. **82**, 217 (1994).
6. A. Abragam, *The Principles of Nuclear Magnetism* (Clarendon, Oxford, 1961; Mir, Moscow, 1963).
7. E. B. Fel'dman and S. Lacelle, J. Chem. Phys. **104**, 2000 (1996).
8. A. A. Lundin, in *Abstracts of the 5th All-Union Conference on Modern NMR and EPR Methods in Solid State Chemistry, 1990*, p. 137.
9. V. A. Atsarkin, V. V. Demidov, G. A. Vasneva, *et al.*, unpublished.
10. D. J. Hudson, *Statistics Lectures on Elementary Statistics and Probability*, CERN Report (Geneva, 1964; Mir, Moscow, 1970).
11. E. S. Grinberg, B. I. Kochelaev, and G. G. Khaliullin, Fiz. Tverd. Tela (Leningrad) **23**, 397 (1981) [Sov. Phys. Solid State **23**, 224 (1981)].
12. R. Sh. Vartapet'yan, B. M. Odintsov, A. V. Filippov, *et al.*, Colloid J. **3** (2000) (in press).
13. A. Adamson, *Physical Chemistry of Surfaces* (Wiley, New York, 1976; Mir, Moscow, 1979).

Translated by V. Sakun

JETP Letters, Vol. 72, No. 7, 2000, pp. 373–376. Translated from Pis'ma v Zhurnal Éksperimental'noĭ i Teoreticheskoĭ Fiziki, Vol. 72, No. 7, 2000, pp. 536–541.

Reversible Structural Phase Transition in Ni–Mn–Ga Alloys in a Magnetic Field

I. E. Dikshteĭn*, D. I. Ermakov*, V. V. Koledov*,*, L. V. Koledov*, T. Takagi****, A. A. Tulaĭkova*, A. A. Cherechukin*,***, and V. G. Shavrov*,****

** Institute of Radio Engineering and Electronics, Russian Academy of Sciences, Mokhovaya ul. 18, Moscow, 103907 Russia*
***e-mail: shavrov@mail.cplire.ru*
**** Laboratory of Strong Magnetic Fields and Low Temperatures, Wroclaw, Poland*
***** Tohoku University, Sendai, Japan*
Received August 18, 2000

In $Ni_{2+x}Mn_{1-x}Ga$ shape-memory ferromagnetic alloys with coincident magnetic and structural phase transitions, a reversible structural field-induced phase transition was observed at constant temperature and pressure in magnetic fields of about 10 T. Computational results are in qualitative agreement with experiment. © *2000 MAIK "Nauka/Interperiodica".*

PACS numbers: 64.70.Kb; 75.30.Kz

Heusler alloy Ni_2MnGa combining ferromagnetic properties with shape memory attracts considerable interest in connection with the search for new kinds of the effect of external fields on the dimensions and shape of materials [1–6]. Recent studies showed both theoretically and experimentally that the phase diagram of nonstoichiometric $Ni_{2+x}Mn_{1-x}Ga$ compositions with partial substitution of Ni for Mn includes a region of concentrations x where the magnetic and structural (martensitic) phase transitions are close to each other or coincide (x = 0.16–0.19). Such alloys were found to exhibit a considerable increase in the temperature of the structural phase transition (SPT) in magnetic fields (up to 1 T), as well as the initiation of the SPT as a result of switching on the magnetic field [5]. However, the question of whether a magnetic-field-driven reversible SPT is possible at constant temperature and pressure is still an open question. The purpose of this study is to investigate experimentally and theoretically the reversible SPT induced by a magnetic field in samples with coincident structural and magnetic phase transitions.

The realization of a reversible SPT in a magnetic field at a given temperature is hindered by the temperature hysteresis of the first-order SPT. The idea of the experiment is as follows. In an external magnetic field, both ends of the temperature hysteresis loop (its width is about several degrees) are shifted to higher temperatures of the SPT with a coefficient of about 1 K/T [5]. Hence, in a magnetic field of about 10 T, the whole loop will be shifted along the temperature axis by a distance exceeding the loop width. In this case, the transition from high-temperature (austenite) to low-temperature (martensite) phase will occur at a higher temperature $T_{AM}(H)$ than the reverse transition in the absence of the magnetic field, $T_{MA}(0)$. Then, by switching the magnetic field on and off at a given temperature within the interval $T_{MA}(0) < T < T_{AM}(H)$, it is possible to induce a reversible SPT. We will call the temperature interval $\Delta\tilde{T} = T_{AM}(H) - T_{MA}(0)$ the magnetic control interval for the SPT.

In the experiment, we used polycrystalline $Ni_{2+x}Mn_{1-x}Ga$ samples prepared by arc melting in argon on a cold bottom. The structural phase state of the samples was studied in magnetic fields of 0–14 T by the optical method [5]. The optical technique allows one to observe the nucleation and motion of the SPT boundaries and the twin boundaries of structural domains in the direct experiment and, on the basis of these observations, to measure the temperatures of the direct and reverse SPT, with the sample surface resolution depending on the external magnetic field. To study the SPT, the sample is polished in the austenitic state and mounted on a substrate in a transparent two-contour thermostat; the magnetic field is produced by a Bitter magnet. The observations are performed using a microscope with a TV camera for individual crystal grains of the polycrystal. This allows one to take into account the natural inhomogeneity of polycrystalline samples, which is mainly responsible for the error in determining the transition point.

Figure 1 shows the $T_{AM}(H)$ and $T_{MA}(H)$ dependences for samples with an excess concentration of Ni (x = 0.16, 0.18, and 0.19). The curves were obtained by averaging the transition temperature over the surface of a polycrystalline sample. One can see that the dependences $T_{AM}(H)$ and $T_{MA}(H)$ are approximately linear for all samples. The coefficients dT_{AM}/dH and dT_{MA}/dH are close to each other and increase with increasing x up to

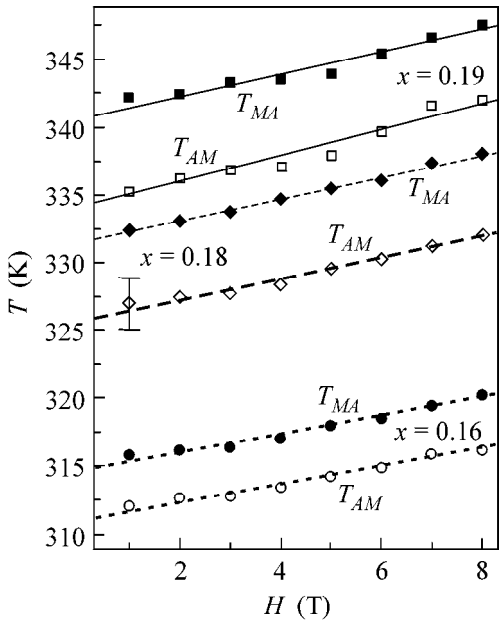

Fig. 1. Field dependences of the temperatures of the direct T_{AM} and reverse T_{MA} structural phase transitions in $Ni_{2+x}Mn_{1-x}Ga$ samples with $x = 0.16$, 0.18, and 0.19.

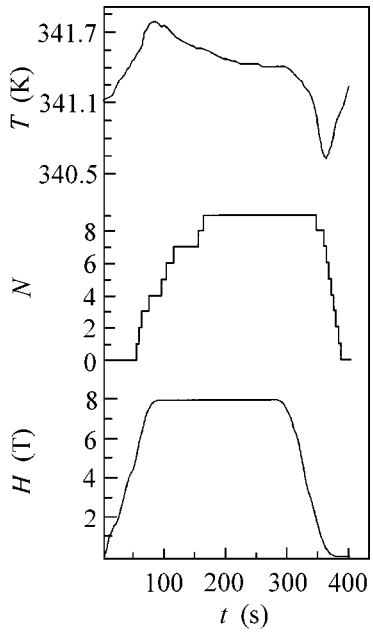

Fig. 2. Time dependences of the temperature *T*, the magnetic field *H*, and the number of crystal grains *N* that undergo a structural transformation in the course of the reversible SPT.

the value $x = 0.19$ at which the magnetic and structural phase transitions merge [5]. As x grows, the temperature hysteresis of the SPT, $T_{MA}(H) - T_{AM}(H)$, also grows. The magnetic control interval averaged over the sample surface is $\Delta\tilde{T} \sim 1$ K.

Figure 2 illustrates the experiment on the reversible SPT induced by a magnetic field at constant temperature and external pressure. This figure presents the time dependences of the magnetic field, the temperature of the sample, and the number N of crystal grains that changed their structural phase state in the course of the experiment. The initial temperature of the sample was selected within the magnetic control interval of the SPT, and all grains in the field of vision of the microscope were initially in the austenitic state. With an increase in the magnetic field, a spontaneous increase in the sample temperature is observed with the formation of martensite in magnetic fields $H > 6$ T. When the field ceases to increase, the temperature relaxes, while the martensite proportion continues growing for some time. As the magnetic field decreases, the temperature also decreases and, starting at 4 T, the martensite phase vanishes. Its total disappearance is observed after the field is switched off in the course of the temperature returning to its original value.

The instability of the sample temperature is explained by the release and absorption of the latent heat of the first-order SPT in the sample. Each time, an increase in temperature occurs simultaneously with the transition to the low-temperature phase, and a decrease in temperature accompanies the transition to the high-temperature phase.

To analyze the phase diagram of the $Ni_{2+x}Mn_{1-x}Ga$ ferromagnet in a magnetic field, we use the Landau phenomenological model of phase transition. We consider a cubic ferromagnet belonging to the O_h point symmetry group and characterized by a magnetic phase transition, which is accompanied by the appearance of a spontaneous magnetization M, and an inherent ferroelastic phase transition to the D_{4h} tetragonal phase, the latter transition being accompanied by the appearance of spontaneous strains. In this case, the order parameters describing the SPT are the components of the macroscopic strain tensor e_{ik}. We will describe the magnetic phase transitions by the components of the macroscopic magnetization M. For the ferromagnet free energy, after its minimization with respect to the strain tensor components not responsible for the SPT, we obtain the expression

$$\begin{aligned} F = F_0 &+ \frac{1}{2}a(e_2^2 + e_3^2) + \frac{1}{3}be_3(e_3^2 - 3e_2^2) + \frac{1}{4}c(e_2^2 + e_3^2)^2 \\ &+ B_2\left[\frac{1}{\sqrt{2}}e_2(m_1^2 - m_2^2) + \frac{1}{\sqrt{6}}e_3(3m_3^2 - m^2)\right] \\ &+ \frac{1}{2}\alpha(m_1^2 + m_2^2 + m_3^2) + \frac{1}{4}\delta(m_1^2 + m_2^2 + m_3^2)^2 \\ &+ K(m_1^2m_2^2 + m_2^2m_3^2 + m_3^2m_1^2) - H_3M_3. \end{aligned} \quad (1)$$

Here, $\alpha = \alpha_0(T - T_c)$, δ, and K are magnetostriction-renormalized exchange constants and the first constant of cubic anisotropy; B is the relativistic magnetostriction constant; a, b, and c are linear combinations of the components of the second-, third-, and fourth-order elastic moduli, respectively: $a = c_{11} - c_{12}$, $b = (c_{111} - c_{112} + c_{123})/6\sqrt{6}$; e_i are linear combinations of the strain tensor components $e_2 = (e_{xx} - e_{yy})/\sqrt{2}$, $e_3 = (2e_{zz} - e_{xx} - e_{yy})/\sqrt{6}$; and $m = M/M_0$, where M_0 is the saturation magnetization away from the Curie point T_C. As the SPT from cubic to tetragonal phase with a two-component order parameter e_2, e_3 is approached, the elastic modulus $a = c_{11} - c_{12}$ tends to zero, and, near the transition point T_{M0}, it can be represented in the form $a = a_0(T - T_{M0})$. The presence of the third-order terms in the thermodynamic potential determines the first-order SPT.

Let us consider the case $b > 0$, $c > 0$, and $K < 0$, which corresponds to the compound under study. In the absence of a magnetic field, five different phases occur in this material [4, 5, 7]: the paramagnetic and ferromagnetic cubic phases, the paramagnetic tetragonal phase, and the ferromagnetic angular and collinear tetragonal phases. In a magnetic field, the Curie point ceases to be a phase transition point, because, for $H \neq 0$, the magnetization remains finite at temperatures $T > T_C$ owing to the paraprocess. In addition, a magnetic field leads to tetragonal distortions of the cubic lattice. Then, in magnetic fields higher than that of magnetic anisotropy $H > H_A = K/M_0$, two different ferromagnetic phases will occur: the martensitic phase with heavy tetragonal distortions and the austenitic phase with weak tetragonal distortions produced by the field.

Minimizing the potential given by Eq. (1) with respect to the variables e_2, e_3, m_1, m_2, and m_3, we obtain the equations of state for describing the distribution of magnetization and elastic strains in the ferromagnet under study, along with the conditions of their stability in the approximation of relatively high magnetic fields $H > H_A$:

$$\begin{aligned} m_1 = m_2 = 0, \quad e_2 = 0, \\ m_3(\alpha + \delta m_3^2 + \sqrt{8/3}Be_3) = M_0H, \end{aligned} \tag{2}$$

$$\begin{aligned} e_3(a + be_3 + ce_3^2) + \sqrt{2/3}Bm_3^2 = 0, \\ (2\delta m_3^3 + M_0H)(a + 2be_3 + 3ce_3^2) - \frac{8}{3}B^2m_3^3 \geq 0. \end{aligned} \tag{3}$$

For $x < x_C$ (x_C is the critical concentration at which the temperatures of the magnetic and structural phase transitions coincide), we obtain from Eqs. (2) and (3) the field dependences of the stability loss temperatures T_{MA} and T_{AM} (see Fig. 3):

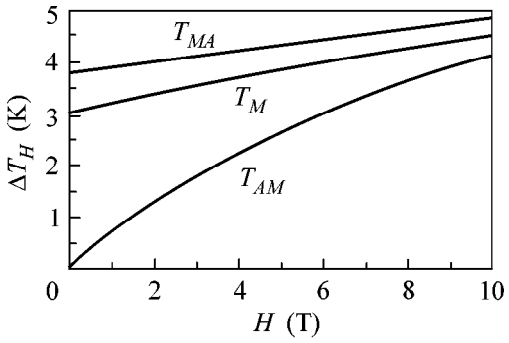

Fig. 3. Section of the T–H–x phase diagram by the plane $x = 0.16$: $\Delta T_H = T_i(H) - T_{AM}(H = 0)$, where $T_i = T_M$, T_{MA}, and T_{AM}.

$$T_{MA} = T_{M0} \times \left\{1 + \frac{b}{a_0}\left[\frac{1}{36}\frac{b}{c} - \sqrt{6}\frac{cB}{b^2}\left(\tau_{M0} - \frac{2}{3}m^2(\tau_{MA})\right)\right]\right\}, \tag{4}$$

$$T_{AM} = T_{M0} \times \left\{1 - \frac{b}{a_0}\left[\frac{2}{9}\frac{b}{c} + \sqrt{6}\frac{cB}{b^2}\tau_{M0} + \left(\sqrt{\frac{32}{3}}\frac{B}{b}\right)^{1/2} m(\tau_{M0})\right]\right\}, \tag{5}$$

where $m(\tau) = [h + (h^2 - \tau^3/27)^{1/2}]^{1/3} + [h - (h^2 - \tau^3/27)^{1/2}]^{1/3}$ for $h > (\tau/3)^{3/2}$ and $m(\tau) = 2\sqrt{\tau/3}\cos(\varphi(\tau)/3)$ for $h < (\tau/3)^{3/2}$; $\varphi(\tau) = \arccos[h(3/\tau)^{3/2}]$; $\tau_{M0} = (T_C - T_{M0})/T_C$; $\tau_{MA} = \tau_{M0} + \sqrt{2/3}\,(bB/c\delta)$; and $h = MH/2\delta$.

The field dependence of the SPT temperature T_M (Fig. 3), which is determined from the condition of equal energies of the phases, has the form

$$T_M = T_{M0}\left\{1 + \frac{b}{a_0}\left[\frac{9}{8}\frac{\delta c^2}{b^3}\{m^4(\tau_M) - m^4(\tau_{M0}) + 4h[m(\tau_M) - m(\tau_{M0})]\} - \sqrt{6}\frac{cB}{b^2}\tau_{M0} - \frac{4}{3}\frac{B^2}{\delta b}\right]\right\}, \tag{6}$$

$$\tau_M = \tau_{M0} + \sqrt{\frac{32}{27}}\frac{bB}{c\delta}.$$

For $h \ll (\tau_{M0}/3)^{3/2}$, the field dependences of T_{MA}, T_{AM}, and T_M are simplified. For example, T_M becomes a linear function of H:

$$T_M(H) = T_M(0) + HT_{M0}M(\sqrt{\tau_M} - \sqrt{\tau_{M0}})/Q, \tag{7}$$

where $Q = 2a_0b^2/9c^2$ is the specific latent heat of the SPT at temperature $T_M(0)$. This corresponds to the results obtained earlier from the thermodynamic theory [4, 5].

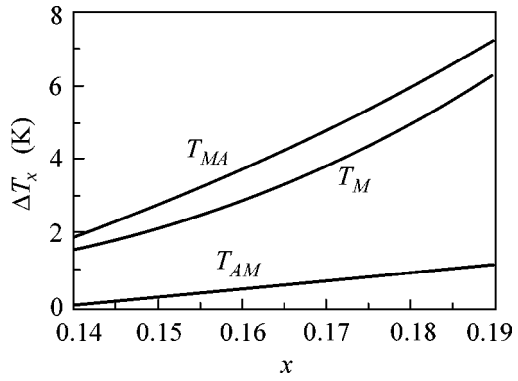

Fig. 4. Section of the T–H–x phase diagram by the plane $H = 0$: $\Delta T_x = T_i(x) - T_{AM}(x = 0.14)$, where $T_i = T_M$, T_{MA}, and T_{AM}.

To construct the phase diagram of the ferromagnet in the T–H–x coordinates, we assume (as in [4, 5]) that both T_{M0} and T_C linearly depend on the concentration:

$$T_{M0} = \tilde{T}_{M0} + \kappa x, \quad T_C = \tilde{T}_C - \gamma x, \tag{8}$$

where κ and γ are the proportionality coefficients.

The sections of the T–H–x phase diagram by planes $x = 0.16$ and $H = 0$ are shown in Figs. 3 and 4, respectively. We present the dependences $\Delta T_H(H)$ and $\Delta T_x(x)$. Here, $\Delta T_H = T_i(H) - T_{AM}(H = 0)$ and $\Delta T_x = T_i(x) - T_{AM}(x = 0.14)$, where $T_i = T_M$, T_{MA}, and T_{AM}. Since many parameters of the problem are unknown, the comparison between the theoretical diagrams and the experimental dependences shown in Fig. 1 can only be qualitative. The diagrams presented in Figs. 3 and 4 were obtained for the following values of the parameters: $\tilde{T}_C = 375$ K, $\tilde{T}_{M0} = 200$ K, $a_0 = b/\tilde{T}_{M0}$, $\alpha_0 = \delta/\tilde{T}_C$, $\delta = 10^8$ Erg/cm^3, $c/b = 11.1$, $b = 2.54 \times 10^{12}$ Erg/cm^3, $B = 2 \times 10^8$ Erg/cm^3, $\gamma = 175$ K, and $\kappa = 700$ K.

From the comparison of Figs. 1, 3, and 4 it follows that, in the concentration interval $0.16 < x < 0.19$, the field and concentration dependences of T_{AM} and T_{MA} obtained in the experiment are in qualitative agreement with the computational results. Specifically, the temperatures T_{AM} and T_{MA} increase with increasing H and x, and the width of the temperature hysteresis loop increases with x. The theory justifies the existence of the temperature and field regions in which a reversible magnetic-field-induced SPT is possible.

Note that an irreversible magnetic-field-induced SPT is known for many magnetic substances (see, e.g., [8, 9]). As far as we know, a reversible field-induced SPT occurs in no other substances except the one described above. However, one should expect that the magnetic-field-driven reversible SPT observed in our experiments in $Ni_{2+x}Mn_{1-x}Ga$ may also occur in sufficiently high magnetic fields in other high-magnetostriction magnetic compounds which undergo a structural phase transformation in the ferromagnetic state.

This work was supported by the Russian Foundation for Basic Research, project no. 99-02-18247.

REFERENCES

1. K. Ullakko, J. K. Huang, C. Kantner, *et al.*, Appl. Phys. Lett. **69**, 1966 (1996).
2. R. C. O'Handley, J. Appl. Phys. **83**, 3263 (1998).
3. R. D. James and M. Wutting, Philos. Mag. A **77**, 1273 (1998).
4. A. N. Vasil'ev, A. D. Bozhko, V. V. Khovailo, *et al.*, Phys. Rev. B **59**, 1113 (1999).
5. A. D. Bozhko, A. N. Vasil'ev, V. V. Khovaĭlo, *et al.*, Zh. Éksp. Teor. Fiz. **115**, 1740 (1999) [JETP **88**, 954 (1999)].
6. G. H. Wu, C. H. Yu, L. Q. Meng, *et al.*, Appl. Phys. Lett. **75**, 2990 (1999).
7. A. D. Bozhko, V. D. Buchel'nikov, A. N. Vasil'ev, *et al.*, Pis'ma Zh. Éksp. Teor. Fiz. **67**, 212 (1998) [JETP Lett. **67**, 227 (1998)].
8. M. A. Krivoglaz and V. D. Sadovskiĭ, Fiz. Met. Metalloved. **18**, 502 (1964).
9. D. A. Mirzaev and V. M. Schastlivtsev, Fiz. Met. Metalloved. **63**, 1105 (1987).

Translated by E. Golyamina

JETP Letters, Vol. 72, No. 7, 2000, pp. 377–380. Translated from Pis'ma v Zhurnal Éksperimental'noĭ i Teoreticheskoĭ Fiziki, Vol. 72, No. 7, 2000, pp. 542–546.

Mechanism of Charge Exchange at a Liquid Crystal–Electrode Interface

A. V. Koval'chuk

Institute of Physics, National Academy of Sciences of Ukraine, pr. Nauki 144, Kiev, 03650 Ukraine

Received August 29, 2000

It is shown that liquid crystal–electrode charge exchange is accomplished via the mechanism of Schottky emission through a thin dielectric layer. The thin dielectric layer (several nanometers) is formed by adsorption of neutral molecules that either are introduced on purpose or occur in even well-purified liquid crystals. The main part of the barrier determining the charge exchange process is due to the ionization of the cation losing an electron and its transformation to the anion. The barrier parameters and the dielectric layer thickness are estimated for the planar and homeotropic alignments of molecules. © *2000 MAIK "Nauka/Interperiodica".*

PACS numbers: 61.30.Gd; 82.30.Fi

1. It is known that, in organic liquids with a high concentration of ions (electrolytes), charge exchange at a liquid–electrode interface proceeds mainly via redox processes [1]. Such a mechanism of charge transfer was considered as the basic one in the majority of works on the electric properties of liquid crystals (LCs). Different charge-transfer mechanisms were also proposed: injection from the electrode [2, 3] and dissociation of available [2] or added [4] impurities. However, the mechanism of current flow through the LC–electrode interface has not been analyzed in detail as yet.

2. In order to enhance the effects of the alignment of molecules on the process of charge exchange, ZL1-4803-000 (Z) liquid crystals (Merck Ltd.) with a high dielectric anisotropy $\Delta\varepsilon$ were used in the investigations. At a temperature of 20°C, Z is characterized by $\varepsilon_\perp = 11.3$ and $\Delta\varepsilon = +51.5$. Investigations showed that pure Z, as well as other liquid crystals, changes its parameters under the action of an external electric field. Molecules of the dye D were added to the LCs in order to stabilize the parameters. The structural formula of D is given in Fig. 1. The main results were obtained for a (Z + 2 wt % D) mixture. The design of the measuring cell and the way of filling it were the same as in [5]. The planar alignment of the LC molecules was generated with the use of electrodes with rubbed polyimide (P electrodes). The homeotropic alignment of the LC molecules was generated with the use of Cu electrodes. The sample thickness d was varied over the range 10–50 μm. The main measurements were performed for samples with $d \approx 30$ μm. The mechanism of current flow in the samples studied was determined from an analysis of current–voltage characteristics (I–V). The density of the steady-state current I_{ST} was analyzed as a function of the voltage U. In addition, the density of the maximum reverse current I_{RM} was determined for each value of U. For this purpose, a sample in which the current reached a steady-state value I_{ST} was terminated in a measuring device. The effect of redox processes on the mechanism of charge exchange was determined by cyclic voltammetry [1]. The parameters of relaxation processes in the electrode regions were investigated by low-frequency dielectric spectroscopy [5, 6]. The alternating current conductivity of samples σ_{AC} was also determined by low-frequency dielectric spectroscopy. The change of its value upon adding the dye indicated that the D molecules in the LCs were virtually neutral. The temperature was stabilized with an accuracy of no worse than 0.2 K using a specially designed thermostat with a sufficiently low level of electromagnetic interference.

3. At the initial stage of the investigations, it was most important to reveal how the redox processes affect the electrode–LC charge transfer process. Structures with asymmetric P–Cu electrodes were used for the investigations. Cyclic voltammograms were obtained by the action of linearly increasing and decreasing voltage pulses. The rates of voltage rise and decrease were the same and equal to 0.46 mV/s. The voltage was varied through the range from 0 to 2.3 V. The measurements were carried out for different polarities at each of the electrodes. In none of the cases, was a current maximum typical for a redox process [1] obtained. The voltage dependence of the current had the form of dynamic I–V characteristics of diode structures.

With barriers, the electric field strength in a sample becomes inhomogeneous. The voltage applied across

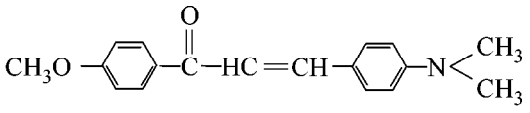

Fig. 1. Structural formula of the dye D.

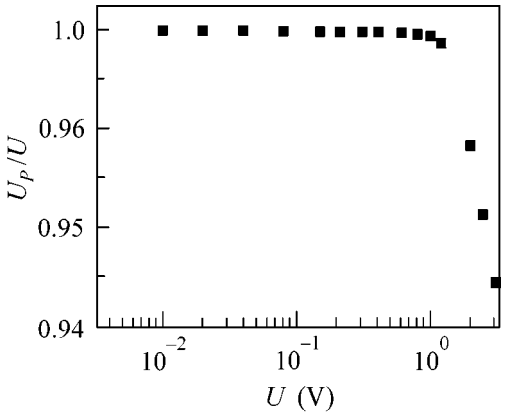

Fig. 2. Dependence of U_P/U on U for a 2% solution of D in Z. Samples with symmetric P electrodes, d = 20.5 μm, and T = 294 K.

the electrode regions (polarization voltage U_p) was determined from the equation [2]

$$U_P = U\frac{I_{RM}}{I_{RM} + I_{ST}}. \quad (1)$$

Figure 2 demonstrates the dependence of U_P/U on U for structures with symmetric P electrodes. It is evident that, at $U < 1$ V, $U_P = 0.998U$; that is, the current is fully determined by the properties of the electrode region for the given range of voltage values. For the given voltage values, the I–V characteristics are nonlinear. The reasons for this nonlinearity were analyzed using various models (space charge limited current, diode mechanism of current flow through electric double layers, etc.). However, Fig. 3 and an analysis of I–V characteristics obtained for other LCs indicate that the experimental data are approximated with the smallest error by the equation

$$I = I_0\exp(\alpha\sqrt{U}), \quad (2)$$

Parameters characterizing charge transfer through the Cu–LC interface (homeotropic alignment) and the P–LC interface (planar alignment) obtained for a 2% solution of D in Z with Cu–P electrodes. The sample thickness was 29.4 μm, and T = 294 K

Electrode	α, $V^{-1.2}$	d_d, nm	φ_{BN}, V	φ_{BI}, V
Cu	6.3	0.92	0.88 ± 0.55	0.70 ± 0.05
P	6.8	4.5	0.37 ± 0.05	0.92 ± 0.05

where I_0 and α are constants whose physical meaning will be considered below. It is known that Eq. (2) may correspond to two different mechanisms of current flow: Schottky emission and Pool–Frenkel emission [7, 8]. To determine which of the above mechanisms can describe charge transfer through the LC–electrode interface, we studied the temperature dependence of I/T^2 at various values of U. The temperature dependence of I/T^2 for samples with asymmetric Cu–P electrodes is shown in Fig. 4 for different polarities of the applied voltage. It follows from the data obtained that $\log(I/T^2)$ depends linearly on $1/T$ in the temperature domain of mesophase existence. Therefore, the mechanism of current flow through the electrode–LC interface corresponds to Schottky emission. In this case,

$$I_0 = A^*T^2\exp(-e\varphi_B/kT), \quad (3)$$

where A^* is the Richardson constant, e is the electron charge, φ_B is the barrier height, and k is the Boltzmann constant.

For $U < 1$ V, almost the total voltage is applied across the electrode regions. Therefore,

$$U = Ed_d, \quad (4)$$

where E is the electric field strength and d_d is the thickness of the electrode region.

Therefore [8]

$$\alpha = \frac{e}{kT}\sqrt{\frac{e}{4\pi\varepsilon_0\varepsilon d_d}}, \quad (5)$$

where ε_0 is the permittivity of free space and ε is the permittivity of the substance.

Schottky emission is emission through a thin dielectric layer. Therefore, it must first be determined at which electrode (depending on the applied voltage polarity) such a barrier forms. For this purpose, we compared the temperature dependence of I/T^2 obtained for samples with Cu–P electrodes to the similar dependence obtained for samples with P electrodes. It was found that the slopes of the temperature dependence of I/T^2 for samples with P electrodes fully coincide with the data for "–" Cu–P "+." From here, it follows that the barrier for the transfer of charge carriers is formed at the anode. Therefore, the data in Fig. 4a characterize charge transfer through the Cu–LC interface (homeotropic alignment of molecules), and the data in Fig. 4b characterize charge transfer through the P–LC interface (planar alignment of molecules). The barrier heights for the isotropic φ_{BI} and nematic φ_{BN} phases are given in the table for the planar and homeotropic alignments of molecules. It is evident that the values of φ_{BN} for the planar and homeotropic alignments differ significantly. From here it follows that the properties of the LC determine the value of φ_B for the LC–electrode contact. However, the difference between the values of φ_{BI} indi-

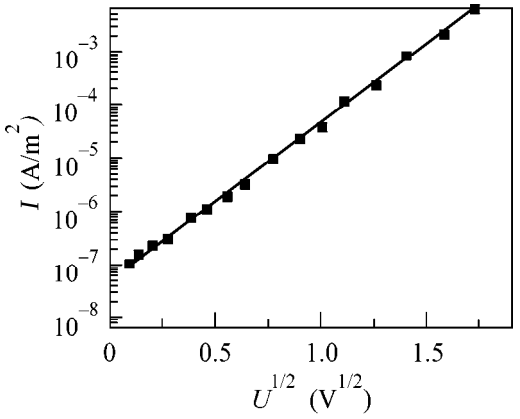

Fig. 3. *I–V* characteristics of a 2% solution of D in Z. Samples with symmetric P electrodes, d = 20.5 μm, and T = 294 K.

cates that the electrode material also affects the barrier height.

With a dielectric layer present, charge transfer through the LC–anode interface can be carried out only by electron emission from the LCs. If it is assumed that such an electron is gained by an ion at the cathode, the question immediately arises as to how charge exchange between the electrodes proceeds continuously in time. Therefore, it may be suggested that, when an cation approaches the anode, it loses not only the "foreign" electron (transforming to a neutral molecule) but also "its own" electron (transforming to an anion). It is the transformation of a neutral molecule to an anion that is responsible for the main part of the barrier. The ionization of a neutral molecule can be described by a dipole with the dipole moment growing until the instance of electron detachment. In the process of ionization, such a dipole will polarize the surrounding molecules. If it is assumed that the energy of this interaction is proportional to the polarizability of molecules and fully determines the value of φ_{BN}, then the ratio of φ_{BN} for the homeotropic alignment of molecules to φ_{BN} for the planar alignment of molecules must be close to $(\varepsilon_\parallel/\varepsilon_\perp)^{1/2}$. For Z, $(\varepsilon_\parallel/\varepsilon_\perp)^{1/2} \approx 2.36$ and virtually coincides with the ratio of φ_{BN}.

Schottky emission is emission through a dielectric layer. Therefore, it is important to elucidate what processes at the electrode surface are responsible for the formation of such a layer. In the case when the LC phase contains almost neutral dye molecules dissolved in it, the question of the reasons for the formation of the dielectric layer is trivial. It is more difficult to find reasons for the formation of a dielectric layer at the electrode surface in pure LCs. It is considered that, as well as in electrolytes, the reason for the formation of the electric double layer in LCs is the adsorption of ions. Our estimates made for pure 5CB showed that, if all the available ions from the bulk of a sample 20 μm thick were adsorbed at the electrode surface, then a layer only 0.01 nm thick would be formed. In the case of better conducting Z, this value is an order of magnitude higher. It follows from the table that the experimental values of d_d are more than an order of magnitude higher. Therefore, it should be assumed that even pure LCs contain neutral impurities whose concentration is considerably higher than the concentration of ions. Such impurities, being adsorbed together with ions, form a dielectric layer, which restricts the direct contact of charge carriers with the electrode and determines the mechanism (Schottky emission) of charge transfer. The neutral impurities in pure LCs may differ in their nature (gas molecules, photooxidation products, synthesis products, etc.). Therefore, the dielectric strength of such a layer with respect to an external electric field is low. Adding dye molecules leads to the formation of an adsorbed layer that is more homogeneous in composition; therefore, its dielectric strength increases.

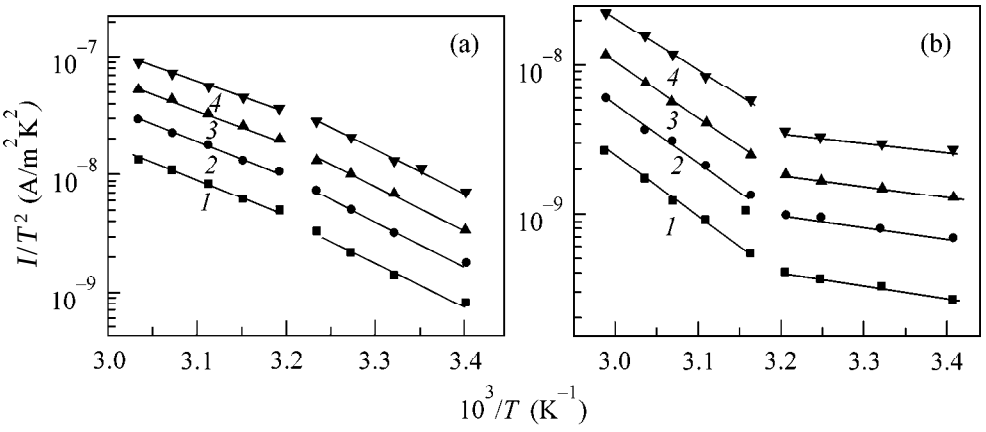

Fig. 4. Temperature dependence of I/T^2 for a 2% solution of D in Z and a sample with Cu–P electrodes at various voltage values (V): (*1*) 0.61, (*2*) 0.81, (*3*) 1.0, and (*4*) 1.2. Measurements were made at the (a) negative and (b) positive polarities of the voltage applied across the P electrode. The sample thickness was 29.4 μm.

REFERENCES

1. *Organic Electrochemistry*, Ed. by M. M. Baizer (Marcel Dekker, New York, 1973; Mir, Moscow, 1978).
2. L. M. Blinov, *Electro-optical and Magneto-optical Properties of Liquid Crystals* (Nauka, Moscow, 1978; Wiley, New York, 1983).
3. N. I. Gritsenko and N. V. Moshel', Ukr. Fiz. Zh. **25**, 1830 (1980).
4. S. V. Serak, A. A. Kovalev, and A. V. Agashkov, Zh. Tekh. Fiz. **70**, 44 (2000) [Tech. Phys. **45**, 858 (2000)].
5. O. V. Koval'chuk, Ukr. Fiz. Zh. **44**, 1376 (1999).
6. A. V. Koval'chuk, Funct. Mater. **5**, 426 (1998).
7. S. M. Sze, *Physics of Semiconductor Devices* (Wiley, New York, 1981; Mir, Moscow, 1984).
8. V. G. Litovchenko and A. P. Gorban', *Fundamentals of the Physics of Metal–Dielectric–Semiconductor Microelectronic Systems* (Naukova Dumka, Kiev, 1978)

Translated by A. Bagatur'yants

JETP Letters, Vol. 72, No. 7, 2000, pp. 381–384. Translated from Pis'ma v Zhurnal Éksperimental'noĭ i Teoreticheskoĭ Fiziki, Vol. 72, No. 7, 2000, pp. 547–552.

1D–3D Crossover in Hopping Conduction of Carbynes

S. V. Demishev*,, A. A. Pronin*, N. E. Sluchanko*, N. A. Samarin*, A. G. Lyapin***, V. V. Brazhkin***, T. D. Varfolomeeva***, and S. V. Popova*****

** Institute of General Physics, Russian Academy of Sciences, ul. Vavilova 38, Moscow, 117942 Russia*

*** e-mail: demis@lt.gpi.ru*

**** Institute of High-Pressure Physics, Russian Academy of Sciences, Troitsk, Moscow region, 142092 Russia*

Received September 4, 2000

D.C. and A.C. conductivities of carbyne samples were studied over the temperature range 1.8–300 K at frequencies 10 MHz–1 GHz. It was established that a variation in the fraction of sp^2 bonds in carbynes induces transition from one- to two- and then to three-dimensional conduction. In the one-dimensional hopping conduction regime, the resistivity of carbynes depends on temperature as $\rho = \rho_0 \exp[(T_0/T)^{1/2}]$, whereas Coulomb correlations are insignificant. The Hunt model of one-dimensional A.C. conductivity is experimentally confirmed.

PACS numbers: 72.20.Ee; 72.30.+q; 72.80.-r

1. The problem of one-dimensional hopping conduction occupies a special place in the theory of disordered media [1, 2]. According to Mott's original approach [1] based on the maximization of transition probability, the resistivity in the variable-range hopping conduction regime in *d*-dimensional space depends on temperature as

$$\rho(T) = \rho_0 \exp[(T_0/T)^{\alpha}], \quad (1)$$

where

$$\alpha = 1/(d + 1). \quad (2)$$

This result was rigorously substantiated for $d = 3$ and 2 in the percolation theory, which, however, does not apply to the one-dimensional (1D) case [2–4], because one cannot define optimum percolation paths bypassing high-resistivity regions of the Miller–Abrahams network in the $d = 1$ case. It is assumed in [2] that, as a result, the α index is equal to 1 rather than 1/2, as it follows from Eq. (2). Nevertheless, Mott's value $\alpha = 1/2$ should again be expected for a 1D system of finite size L [2, 5, 6].

Note that the $\alpha = 1/2$ value in a low-dimensional system can also be caused by the formation of a Coulomb gap [4] or by the nonoptimal hopping regime [7]. The $\alpha = 1$ value (characteristic of $d = 1$ and $L \longrightarrow \infty$) may also appear for finite chains with the Hubbard correlations [3]. One should also take into account that at $T \neq 0$ the hopping distance in a disordered system is limited from above by the wave-function phase coherence length [7], so that the problem of hopping conduction should always be considered for regions of finite sizes.

Hence, from the theoretical point of view, the question of exponent α for 1D hopping conduction is still an open question. When experimentally investigating this issue, it is desirable to deal with a system of "variable" dimensionality that could transform from a three-dimensional (3D) random network to a system of 1D disordered linear chains. Such a situation occurs in carbyne samples synthesized under high pressure [8].

Carbyne is an allotropic carbon form based on *sp*-type bonds and possessing a clear-cut linear-chain structure [9, 10]. Contrary to other allotropic modifications with sp^2 (graphite) or sp^3 (diamond) bonds, carbyne cannot be synthesized as a perfect crystal, because its chains contain "built-in" disorder, probably due to the instability of large linear carbon clusters [10]. Although up to now there is no commonly accepted model structure of carbyne, it is customarily believed that linear *sp* segments of the polymeric carbon molecule in carbyne alternate with sp^2-hybridized carbon atoms [8–10]. The sp^2 centers give rise to chain kinks, and the dangling bonds appearing at the kinks may attach impurity atoms or form interchain links (in the absence of the sp^2 defects, the carbon chains are bonded by weak van der Waals forces). As a result, the carbon chains may form complex globular structures.

The fraction of sp^2 bonds in carbyne can be varied smoothly by applying high pressure and temperature [8]. An increase in the synthesis temperature T_{syn} under pressure induces the $sp \longrightarrow sp^2$ transition, i.e., the formation of a disordered graphite-like network from the structure dominated by 1D chains. The samples synthesized at T_{syn} = 670–780°C exhibited low-temperature hopping conduction with exponent 1/3 characteristic of the two-dimensional (2D) case [8].

It follows from the above that carbynes synthesized under high pressure may become promising objects for

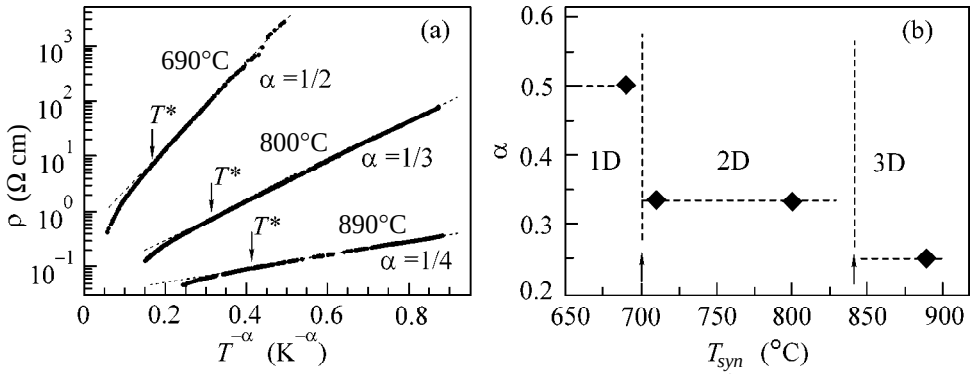

Fig. 1. (a) Temperature dependence of conductivity and (b) hopping conduction exponent for carbyne samples synthesized at different temperatures.

the experimental study of the influence of space dimensionality on hopping conduction. Moreover, the study of hopping transport sensitive to the topology of a disordered system may provide more insight into the structure of carbines, which is now still a controversial subject. In this respect, the purpose of this work was to investigate D.C. and A.C. hopping conduction of carbines prepared under pressure under different synthesis conditions.

2. Carbyne with chains …=C=C=C=C=… of the cumulene type was synthesized at the Nesmeyanov Institute of Organoelement Compounds, Russian Academy of Sciences, and used as starting material. Samples were prepared by the method used in [8]. Synthesis was carried out at a pressure of 7.7 GPa. At different T_{syn} values, the sample structure was identical to that described in [8]. The temperature dependences of D.C. conductivity were studied in the range $1.8 < T < 300$ K; A.C. conductivity was measured at $6 < T < 300$ K in the frequency range $\omega/2\pi$ = 10 MHz–1 GHz. The measurement technique is described in detail in [11].

3. The temperature dependences $\rho(T)$ for different T_{syn} temperatures are shown in Fig. 1a. In coordinates $\log(\rho) = f(T^{-\alpha})$, linear segments are clearly seen in the curves at $T < T^* \sim 40$ K down to $T \sim 1.8$ K. The index α increases with decreasing synthesis temperature (Fig. 1). A value of 1/4 found for this parameter for T_{syn} = 890°C corresponds to the 3D Mott's law, while the reduction in T_{syn} to 800°C increases α to 1/3, which is characteristic of 2D hopping conduction [Eq. (2)]. In the vicinity of $T_{syn} \sim 700$°C, the hopping conduction exponent changes to 1/2 (Fig. 1, T_{syn} = 690°C).

Thus, based on Eqs. (1) and (2), one can assume that the rise in the temperature of synthesis under pressure induces crossover from 1D to 3D hopping conduction. In the transition region $700 < T_{syn} < 800$°C, the carbyne matrix represents a set of mutually noninteracting 2D carbon layers. Such an interpretation qualitatively agrees with the data [8] on the $sp \longrightarrow sp^2$ transition, because the "degree of cross-linking" between the carbon chains increases with T_{syn} and the effective dimensionality of the system should increase. Note that, according to [8], carbyne samples undergo "graphitization" at $T_{syn} \sim 700$°C, so that the crossover to 2D conduction at $T_{syn} > 700$°C seems to be quite natural.

At the same time, it was assumed in [8] that a quasi-one-dimensional structure occurs in carbyne at $T_{syn} <$ 500°C, while in the samples obtained at higher temperatures the fraction of sp^2 bonds is appreciable. Because of this, the interpretation of the data in Fig. 1 as a 1D $\longrightarrow$ 2D $\longrightarrow$ 3D transition is not unique. For example, the $\alpha = 1/2$ value may be explained by the appearance of a Coulomb gap in a system with 2D conduction (note that such an interpretation of the $\alpha = 1/2$ index is most frequent at the present time).

To clarify this issue, the temperature and frequency dependences of the real σ' and imaginary σ'' parts of conductivity were measured for a sample with $\alpha = 1/2$ (T_{syn} = 690°C). One can easily show that $\sigma'(\omega, T)$ of a $d = 2$ system dominated by the Coulomb correlations is described in the pair approximation by the expression analogous to the Pollak–Geballe formula [3, 11, 12]:

$$\sigma'(\omega, T) \approx \sigma_0 \frac{\omega}{\nu_{ph}} \ln^3\left(\frac{\nu_{ph}}{\omega}\right)\left[k_B T + \frac{2e^2}{\varepsilon a \ln(\nu_{ph}/\omega)}\right], \quad (3)$$

where a is the localization radius, ε is the dielectric constant, and ν_{ph} is the characteristic phonon frequency. For this reason, if the data on A.C. hopping conduction are analyzed within the framework of the standard approximation

$$\sigma'(\omega, T) \propto \omega^s T^q, \quad (4)$$

then the case of Coulomb gap should correspond to $s < 1$ and $q < 1$. However, the experiment does not show such a dependence. It is seen from Fig. 2 that the low-temperature asymptotic form of $\sigma'(\omega, T)$ is $\sigma'(\omega, T) \propto T^{1.5–1.8}$; i.e., $q > 1$. Moreover, the temperature dependence $\sigma''(\omega, T) \propto T^{0.6–0.7}$ observed for the imaginary part of the conductivity differs substantially from the behavior of $\sigma'(\omega, T)$ (Fig. 2).

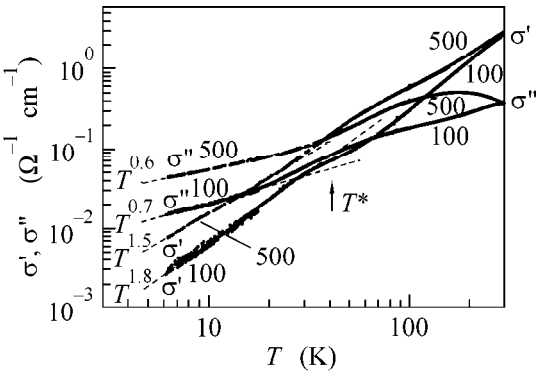

Fig. 2. Temperature dependence of real and imaginary parts of A.C. conductivity at different frequencies for the sample synthesized at T_{syn} = 690°C. Numbers at the curves correspond to frequencies in MHz.

Let us analyze the reasons for this discrepancy in more detail. For the power-law asymptotic behavior (4) the Kramers–Kronig relation gives [3]

$$\sigma''/\sigma' = \tan(\pi s/2). \quad (5)$$

Hence it follows that the different temperature dependences of σ' and σ" can only be observed if the exponent *s* strongly depends on temperature. It follows from Fig. 3a that Eqs. (4) and (5) can be used for the description of hopping conduction in carbynes. Indeed, the exponent *s* should not depend on frequency at T = const and, hence, σ"/σ' should be constant, which is in fact observed with a reasonable accuracy in the range $\omega/2\pi < 500$ MHz at $T < 70$ K. In what follows, we restrict ourselves to the analysis of the data in Figs. 2 and 3 at this frequency interval and leave the decrease in the σ"/σ' ratio at $\omega/2\pi > 500$ MHz and $T < 10$ K for further publications.

Let us use Eq. (5) and define "empirical" exponent *s* as $s(T) = (2/\pi)\arctan(\sigma''/\sigma')$. The results of the calculation of $s(T)$ using the data in Fig. 2 are presented in Fig. 3b (curves *1*, *2*). It is noticeable that the *s* index decreases from $s \sim 0.9$ to $s \sim 0.5$, i.e., by a factor of 1.8, as the temperature changes from T = 6 K to $T = T^* \sim$ 40 K. Such a large change in *s* cannot be provided by Eq. (3), where $s(T) \approx$ const within an asymptotic accuracy (Fig. 3b, curve *3*). When calculating $s = \partial \ln\sigma/\partial \ln\omega$ [Eqs. (3) and (4)], we used the $\nu_{ph} \sim 10^{13}$ s^{-1} value, the experimental value T_0 = 340 K obtained from the data in Fig. 1, and the explicit expression $k_B T_o \approx 6.2e^2/\varepsilon a$ given by the 2D Coulomb gap model [13]. Note that analogous calculations with the other known models of A.C. hopping conduction in 2D and 3D systems [3, 11], including multiple and nonoptimal hopping, also yield $s(T) \approx$ const.

At the same time, a strong temperature dependence $s(T)$ is characteristic of in the 1D systems. According to the Hunt calculation for a 1D system [5, 6],

$$\sigma' \approx f(T)\omega^{s(T)}, \quad (6)$$

$$s(T) \approx \frac{(AT_0/T)^{1/2} - 2}{(AT_0/T)^{1/2} + 2}, \quad (7)$$

where T_0 is the same as in Eq. (1) and the parameter A depends on the ratio between the system size and the localization radius: $A \approx \exp(2)L/a$. Curve *4* in Fig. 3b is obtained for Eq. (7) with $A = 5 \times 10^3$ corresponding to the ratio $L/a \sim 680$. One can see that the theoretical dependence (7) adequately describes the shape and the amplitude of the $s(T)$ curve for a reasonable L/a ratio. Considering that the Hunt model [5, 6] is approximate, such an agreement between the theory and the experiment seems to be quite satisfactory.

4. In summary, we have shown that a change in the hopping conduction exponent α in carbynes synthesized under high pressure is caused by a change in the dimensionality of the system. A decrease in the synthesis temperature induces 3D ⟶ 1D crossover. In the intermediate range $700 < T_{syn} < 800$°C, the hopping conduction is two-dimensional, with the Coulomb correlations not affecting, to a first approximation, the conductivity.

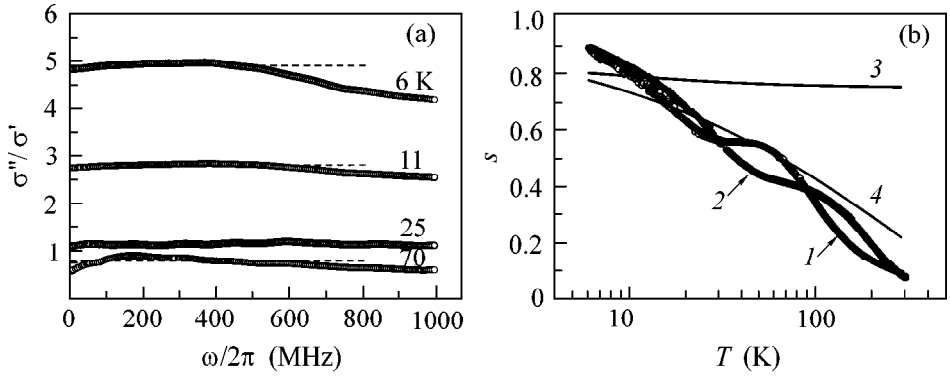

Fig. 3. Analysis of the frequency and temperature dependences of A.C. conductivity using Eqs. (4)–(7) for the samples synthesized at T_{syn} = 690°C. (a) Frequency-dependent σ"/σ' ratio for different temperatures. (b) Temperature-dependent exponent *s*: (*1*) experiment with 100 MHz, (*2*) experiment with 500 MHz, (*3*) model of Coulomb correlations for d = 2, and (*4*) Hunt model for d = 1.

This result allows one to refine the scenario of the $sp \longrightarrow sp^2$ transition [8]. Since the 1D conduction persists up to $T_{syn} \sim 700$°C, the appearance of new sp^2 centers likely leads to the disorder and bending of individual chains in this range of synthesis temperatures. At $T_{syn} > 700$°C, the increase in the fraction of the sp^2 bonds induces cross-linking between the chains, rendering the conduction two-dimensional. On a further increase in T_{syn} and a rise in the concentration of sp^2 centers in the carbyne matrix, the topology of quasi-two-dimensional carbon layers becomes more complicated and they start to interact with each other, leading to the 3D character of conduction.

From the viewpoint of one-dimensional hopping conduction, the data obtained in this work suggest that, first, the α value for a 1D system is 1/2 rather than 1. Second, the A.C. conductivity is adequately described by the Hunt model, so that the results obtained can be regarded as the first experimental confirmation of the theoretical calculation with this model. Third, carbynes represent an important methodological example of an experimental situation where the $\alpha = 1/2$ value is not caused by the appearance of a Coulomb gap in the density of localized states.

This work was supported by the Russian Foundation for Basic Research (project nos. 00-02-16403 and 99-02-17408) and the programs of the Ministry of Industry, Science, and Technology "Fullerenes and Atomic Clusters," "Physics of Microwaves," and "Fundamental Spectroscopy." We are grateful to Yu.P. Kudryavtsev† for providing the carbyne powder.

† Deceased.

REFERENCES

1. N. F. Mott and E. A. Davis, *Electronic Processes in Noncrystalline Materials* (Clarendon, Oxford, 1979; Mir, Moscow, 1982), Vol. 1.
2. W. Brening, G. H. Dohler, and H. Heuszenau, Philos. Mag. **27**, 1093 (1973).
3. I. P. Zvyagin, *Kinetic Phenomena in Disordered Semiconductors* (Mosk. Gos. Univ., Moscow, 1984).
4. B. I. Shklovskiĭ and A. L. Efros, *Electronic Properties of Doped Semiconductors* (Nauka, Moscow, 1979; Springer-Verlag, New York, 1984).
5. A. Hunt, Solid State Commun. **86**, 765 (1993).
6. A. Hunt, in *Proceedings of the 5th International Conference on Hopping and Related Phenomena*, Ed. by C. J. Adkins, A. R. Long, and J. A. McInnes (World Scientific, Singapore, 1994), p. 65.
7. I. P. Zvyagin, Phys. Status Solidi B **120**, 503 (1983).
8. A. G. Lyapin, V. V. Brazhkin, S. G. Lyapin, *et al.*, Phys. Status Solidi B **211**, 401 (1999).
9. Yu. P. Kudryavtsev, S. E. Evsyukov, M. V. Guseva, *et al.*, Izv. Akad. Nauk, Ser. Khim., No. 3, 450 (1993).
10. B. M. Bulychev and I. A. Udod, Ross. Khim. Zh. **39**, 9 (1995).
11. S. V. Demishev, A. A. Pronin, N. E. Sluchanko, *et al.*, Pis'ma Zh. Éksp. Teor. Fiz. **65**, 322 (1997) [JETP Lett. **65**, 342 (1997)].
12. B. I. Shklovskiĭ and A. L. Efros, *Proceedings of the All-Union Conference on Physics of Semiconductors* (ÉLM, Baku, 1982), Vol. 1, p. 65.
13. I. L. Aleiner and B. I. Shklovskii, Phys. Rev. B **49**, 13721 (1994).

Translated by V. Sakun

JETP Letters, Vol. 72, No. 7, 2000, pp. 385–392. Translated from Pis'ma v Zhurnal Éksperimental'noĭ i Teoreticheskoĭ Fiziki, Vol. 72, No. 7, 2000, pp. 553–565.

Attention Readers

The papers of M.A. Baranov "Superfluid Phase Transition in Trapped Atomic Fermi Gas" and Yu.M. Makeenko "Reduced Models and Noncommutative Gauge Theories" continue a new heading "Scientific Summaries" in the journal *JETP Letters*. Under this heading will be published ordered reviews of a moderate size on the basis of the results obtained within the framework of completed projects supported by the Russian Foundation for Basic Research. The editorial board intends to publish 10–12 reviews per year and hopes that this initiative will be supported by the scientific community.

Superfluid Phase Transition in Trapped Atomic Fermi Gas

M. A. Baranov

Kurchatov Institute Russian Research Centre, pl. Kurchatova 1, Moscow, 123182 Russia

e-mail: baranov@kapitza.ras.ru

Received September 13, 2000

Superfluid phase transition in an atomic Fermi gas confined to a harmonic trap is studied. The critical transition temperature and the temperature dependence and spatial shape of the order parameter are determined. The spectrum and wave functions of single-particle and collective excitations are obtained for a gas in the superfluid phase. The excitation eigenfrequencies exhibit a pronounced temperature dependence, allowing, e.g., identification of the superfluid phase. © *2000 MAIK "Nauka/Interperiodica".*

PACS numbers: 03.75.Fi; 05.30.Fk

Successful experiments on the Bose condensation of alkaline atomic gases in magnetic traps [1–3] have stimulated unprecedented interest in studying the coherent quantum phenomena in ultracold spatially inhomogeneous gas systems (see, e.g., review [4]). This is caused by a number of reasons, whose combination renders these systems absolutely unique objects for investigations, both theoretical and experimental. On the one hand, such systems are rarefied by their nature, so that all effects of interatomic interaction are governed by a single small parameter—gas parameter—and, thus, can be calculated by the standard methods of perturbation theory. Moreover, the use of the Feshbach effect enables one to change, in some cases, the magnitude of interatomic interaction (scattering length) over a rather wide range, up to a change in its sign [5]. On the other hand, the presence of comparatively simple and well-elaborated optical methods for manipulating gas samples of alkaline elements (which are used in the overwhelming majority of experiments), in conjunction with the well-elaborated methods of measuring their physical properties, allows one to set up experiments which are a dream for physics of condensed matter.

Although the great majority of experiments to date have been carried out with Bose gases, interest in studying Fermi gases (such as, e.g., ^{6}Li, ^{40}K, and metastable triplet ^{3}He) has become more and more evident in recent years. The main problem in the experimental studies of atomic Fermi gases is associated with the difficulty of cooling them below the quantum degeneracy temperature; though successfully utilized as a final step in reaching temperatures on the nano-Kelvin scale in the case of Bose gases, the evaporative cooling method proves to be much less efficient for fermions, because, due to the Pauli exclusion principle, the collisional frequency decreases with lowering temperature. As a result, one is forced into contrivances of various kinds and, thus, to add complexity to the experiment (for details, see [6–8]). Nevertheless, it was reported in 1999 [9] that a two-component Fermi-gas sample containing 7×10^5 ^{40}K atoms was successfully cooled in a magnetic trap down to a temperature of 300 nK, which comprises approximately one-half of the quantum degeneracy temperature (Fermi temperature) for this number of atoms in the experimentally used trap. At present, experiments of this type are being projected and implemented at most laboratories involved in studying the physical properties of ultracold gases.

The presently available theoretical developments may be conventionally divided into two groups. The

0021-3640/00/7207-0385$20.00

works devoted to studying the properties of Fermi gases in the normal state and the manifestations of the effects of quantum statistics (Pauli's principle) in the optical and dynamical characteristics of gas samples comprise the first group. In this regard, the prediction of the spontaneous emission inhibition [10, 11] and line narrowing for laser radiation transmitted through a gas sample [12] in the quantum degeneracy regime, as well as the effect of a substantial decrease in the collisional damping of the periodic motion executed by a probe particle in a gas cloud [13], is noteworthy. Collective oscillations of different symmetry were studied for a gas cloud in both hydrodynamic and collisionless regimes in [14] and [15, 16], respectively. {It should be noted that the hydrodynamic regime is possible for ^{6}Li because of the occurrence of a rather large triplet *s*-scattering length ($a = -1140$ Å [17]) in comparatively weak magnetic fields (Feshbach effect)}.

And yet of the greatest interest, from both theoretical and experimental points of view, is the investigation of a phase transition to the superfluid state in the Fermi-gas systems considered. This transition, in principle, may occur in ^{6}Li [18] and ^{40}K [19], because the scattering length a in both may become negative (i.e., corresponding to attraction) and large (~10^3 Å) in the presence of the Feshbach effect. (Large scattering lengths are crucial for the gas systems considered, because they hold out a hope of obtaining the experimentally attainable superfluid transition temperatures.) The possibility of superfluid pairing in a two-component atomic ^{6}Li system with completely polarized electron spins was pointed out in [18, 20], where the "singlet" *s*-pairing between the atoms from different hyperfine components was considered for the systems with negative scattering length. The estimates carried out for the critical temperature using the well-known formulas for spatially homogeneous systems yielded an experimentally attainable value of the order of 30 nK for a gas density of 4×10^{12} cm^{-3}. Another scenario of the superfluid transition under the same conditions (in the presence of only the triplet *s*-scattering) is associated with the formation of the "triplet" Cooper pairs with orbital angular momentum $l = 1$ [21]. Although the mechanism of formation of the Cooper pairs in this case is insensitive to the interaction sign, realistic values of critical temperature can only be attained for gas samples with an appreciably higher density. Note also that the *p*-pairing in the presence of dipole–dipole interactions was discussed in [22].

By full analogy with the spatially homogeneous case, the transition of a Fermi gas to the superfluid phase profoundly modifies its properties, which may serve by itself as an indication of the formation of a new phase. Below, the specific features of the superfluid phase transition in a Fermi gas under the conditions of confined trap geometry and the properties (single-particle and collective excitations) of a gas sample in the superfluid phase are analyzed in detail (see works [23–26]). For simplicity, only the systems with singlet pairing will be considered, because the extension to the triplet pairing presents a few problems.

The Hamiltonian of a two-component atomic Fermi gas (α and β atoms) confined to an isotropic harmonic potential has the form ($\hbar = 1$)

$$H = \sum_{i=\alpha,\beta} \int d\mathbf{r} \psi_i^\dagger(\mathbf{r}) H_0 \psi_i(\mathbf{r}) + V \int d\mathbf{r} \psi_\alpha^\dagger(\mathbf{r}) \psi_\alpha(\mathbf{r}) \psi_\beta^\dagger(\mathbf{r}) \psi_\beta(\mathbf{r}). \quad (1)$$

Here, $\psi_i(\mathbf{r})$ are the field operators for the α and β components, whose concentrations are assumed to be equal; $H_0 = -\nabla^2/2m + m\Omega^2 r^2/2 - \mu$; Ω is the trap frequency; m is the atomic mass; and μ is the chemical potential. The second term in Eq. (1) corresponds to the attractive short-range interaction between the α and β atoms (*s*-scattering length $a < 0$) with coupling constant $V = 4\pi a/m$. The interaction between the $\alpha\alpha$ and $\beta\beta$ atoms is ignored in Hamiltonian (1), because it corresponds to the scattering of fermions with angular momentum $l \geq 1$.

The attractive interaction between the different components of the *s*-scattering channel gives rise to the superfluid phase transition [18], with the complex function $\Delta_0(\mathbf{r}) = |V|\langle\psi_\alpha(\mathbf{r})\psi_\beta(\mathbf{r})\rangle$ as the order parameter. For a spatially homogeneous Fermi gas of density coinciding with the maximum density n_0 of a trapped gas, the critical temperature $T_c^{(0)}$ of superfluid phase transition would be [27]

$$T_c^{(0)} = 0.28\varepsilon_F \exp\{-1/\lambda\},$$

where $\lambda = 2|a|p_F/\pi \ll 1$ is a small parameter (gas parameter), $p_F = mv_F = (3\pi^2 n_0)^{1/3}$ is the Fermi momentum, and $\varepsilon_F = p_F^2/2m \approx \mu$ is the Fermi energy. The situation where $T_c^{(0)}$ is much greater than the trap frequency, $T_c^{(0)} \gg \Omega$, is of prime interest for the experiment. It is natural to expect that the critical temperature T_c of superfluid transition in a trap will only slightly differ from $T_c^{(0)}$. The relevant correction can be most conveniently found from the Ginzburg–Landau equation incorporating the potential $U_{trap} = m\Omega^2 r^2/2$ of an external harmonic trap (for details, see [23]):

$$\left[-\kappa^2 \partial_{\mathbf{R}}^2 + \frac{1+2\lambda}{2\lambda} R^2 - \ln\frac{T_c^{(0)}}{T}\right]\Delta + \frac{7\zeta(3)}{8\pi^2}\frac{|\Delta|^2}{T^2}\Delta = 0, \quad (2)$$

which holds at near-critical temperatures T, $(T_c - T)/T_c \ll 1$. In this equation, $\kappa = \sqrt{7\zeta(3)/48\pi^2}\,(\Omega/T) = 0.13(\Omega/T) \ll 1$ [$\zeta(z)$ is the Riemann zeta function] and $R = r/R_{TF}$ is the distance from the center of the trap in units of the Thomas–Fermi gas-cloud radius $R_{TF} = v_F/\Omega$. As usual, the critical temperature corresponds to

the appearance of a nontrivial solution of Eq. (2); in this temperature range, the nonlinear term can be ignored, because $\Delta \longrightarrow 0$ as $T \longrightarrow T_c$. Linearized Eq. (2) formally coincides with the Schrödinger equation for a particle with mass $1/2\kappa^2$ in a spherically symmetric harmonic potential with frequency $2\tilde{\kappa} = 2\kappa(1 + 1/2\lambda)^{1/2}$. One can then straightforwardly obtain

$$\frac{T_c^{(0)} - T_c}{T_c^{(0)}} \approx \ln\frac{T_c^{(0)}}{T_c} = 3\tilde{\kappa} \ll 1 \qquad (3)$$

for the correction to the critical temperature of superfluid transition in a trap. The corresponding order parameter is proportional to the ground-state wave function of an oscillator:

$$\Delta_c(\mathbf{R}) \sim \varphi_0(R) \equiv (\pi l_\Delta^2)^{-3/4} \exp(-R^2/2l_\Delta^2),$$

where $l_\Delta = \kappa/\sqrt{\tilde{\kappa}} \ll 1$ is finite at $T \longrightarrow 0$ and determines the size (in units of R_{TF}) of a region where the superfluid phase appears. At the same time, the size l_Δ proves to be much greater than the characteristic decay length $\xi_K \sim R_{TF}\Omega/T_c$ of the normal-phase correlators at temperature T_c: $l_\Delta \gg \xi_K/R_{TF}$, thereby justifying the expansion in gradients of the order parameter when deriving Ginzburg–Landau Eq. (2). To determine the temperature-dependent coefficient in the expression for the order parameter, it is convenient to write the latter as $\Delta(\mathbf{R}, T) = \alpha(T)\,(\varphi_0(R) + \delta\varphi(\mathbf{R}, T))$, where $\varphi = \varphi_0 + \delta\varphi$ satisfies the normalization condition $\int_{\mathbf{R}}|\varphi(\mathbf{R}, T)|^2 = 1$ and α and $\delta\varphi \longrightarrow 0$ as $T \longrightarrow T_c$. Equation (2) can then be used to determine α and $\delta\varphi$ in the form of expansions in rational powers of $\ln(T_c/T) \approx \delta T/T_c \ll 1$. Finally, to the leading order, one has

$$\Delta(\mathbf{R}, T) \approx \Delta_0(\mathbf{R}, T) = T_c\sqrt{\frac{16\pi^2\sqrt{2}}{7\zeta(3)}\ln\frac{T_c}{T}} \times \exp\left(-\frac{R^2}{2l_\Delta^2}\right) \approx 5.15T_c\sqrt{\frac{T_c - T}{T_c}}\exp\left(-\frac{R^2}{2l_\Delta^2}\right). \qquad (4)$$

Figure 1 presents the approximate solutions Δ_0 (solid lines) and the corresponding numerical solutions (dashed lines) of Eq. (2) for $T_c^{(0)}/\Omega = 5$; $\lambda = 0.3$; and $\delta T/T_c = 0.001$, 0.01, and 0.03. For these $T_c^{(0)}/\Omega$ and λ values, one has $\tilde{\kappa} = 4.4 \times 10^{-2}$; the corresponding value of $T_c = 0.87\,T_c^{(0)}$ found for the critical temperature from Eq. (3) is only 1% higher than the T_c value obtained by the numerical solution of Eq. (2).

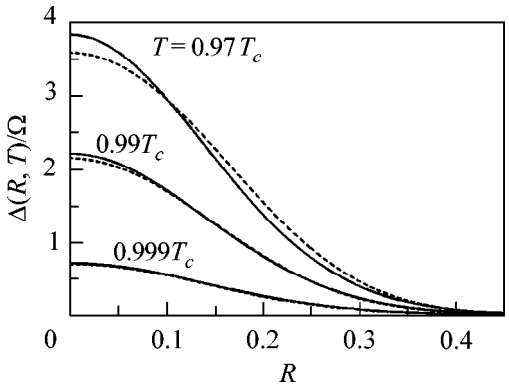

Fig. 1. Order parameter as a function of R at different temperatures. The solid lines correspond to $\Delta_0(R, T)$ from Eq. (4), and the dashed lines correspond to the numerical solution of Eq. (2).

At an arbitrary temperature lower than critical one, the order parameter should be determined self-consistently either from the Gorkov equation for the Green's functions or, which is the same, from the Bogoliubov–de Gennes equations

$$H_0\begin{pmatrix}U_\nu\\V_\nu\end{pmatrix} + \begin{pmatrix}\Delta(\mathbf{R})V_\nu\\-\Delta^*(\mathbf{R})U_\nu\end{pmatrix} = \varepsilon_\nu\begin{pmatrix}U_\nu\\-V_\nu\end{pmatrix} \qquad (5)$$

with the self-consistency condition

$$\Delta(\mathbf{R}) = |V|\sum_\nu U_\nu(\mathbf{R})V_\nu^*(\mathbf{R})\tanh\frac{\varepsilon_\nu}{2T}. \qquad (6)$$

In these equations, $\varepsilon_\nu \geq 0$ are the energies of single-particle excitations and $U_\nu(\mathbf{R})$ and $V_\nu(\mathbf{R})$ are their wave functions. The latter specify the Bogoliubov canonical transformation

$$\begin{pmatrix}\psi_\alpha(\mathbf{R})\\\psi_\beta(\mathbf{R})\end{pmatrix} = \sum_\nu\left[U_\nu(\mathbf{R})\begin{pmatrix}\alpha_\nu\\\beta_\nu\end{pmatrix} + V_\nu^*(\mathbf{R})\begin{pmatrix}\beta_\nu^\dagger\\-\alpha_\nu^\dagger\end{pmatrix}\right]$$

from the initial field operators $\psi_\alpha(\mathbf{R})$ and $\psi_\beta(\mathbf{R})$ to the operators of single-particle excitations α_ν and β_ν. In the case of interest, $T_c \gg \Omega$, the solution of this problem can be found by using Eilenberger's equations [28]. As a result, one obtains the following closed equation for the order parameter $\Delta(R)$ [24]:

$$\frac{\Delta}{\sqrt{1-R^2}} = \Delta\tilde{S}_{1/2} + S_{5/2}\frac{1-R^2}{12}\left[\frac{d^2\Delta}{dR^2} + \frac{1}{R}\frac{d\Delta}{dR}\frac{2-3R^2}{1-R^2}\right] - S_{7/2}\frac{5(1-R^2)}{24\Omega^2}\left(\frac{d\Delta}{dR}\right)^2\Delta, \qquad (7)$$

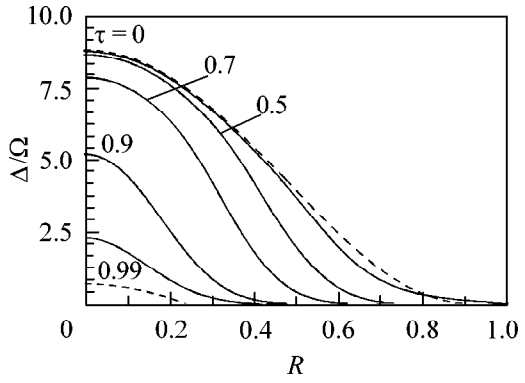

Fig. 2. (solid lines) Order parameter $\Delta(R)$ at different temperatures $\tau = T/T_c$. Dashed lines correspond to $\Delta(R)$ in the local-density approximation for τ = (upper curve) 0 and (lower curve) 0.99.

where $S_\alpha \equiv \pi T \sum_n \omega_n^2/(\omega_n^2 + \Delta^2)^\alpha$ for $\alpha = 5/2$ and 7/2 [$\omega_n = \pi T(2n + 1)$ is the Matsubara frequency] and

$$\tilde{S}_{1/2} = \frac{1}{\lambda} - \gamma - \ln\frac{\Delta}{\pi T_c^{(0)}(1 - R^2)} - \int_0^\infty \frac{2dx}{\exp\left(\frac{\Delta}{T}\cosh(x)\right) + 1},$$

where $\gamma = 0.5772$ is the Euler constant.

For temperatures T close to T_c, Eq. (7) reduces to Ginzburg–Landau Eq. (2). For lower temperatures, Eq. (7) can be solved numerically with boundary conditions $\Delta'(0) = 0$ and $\Delta(1) = 0$. The numerical solutions for $\Delta(R)$ are shown in Fig. 2 for $\lambda = 0.3$, $T_c^{(0)} = 5\,\Omega$ ($T_c = 0.86\,T_c^{(0)}$), and different temperatures (solid lines). For comparison, the results obtained for $\Delta(R)$ in the local-density approximation are also shown in Fig. 2 by the dashed lines for $\tau = 0$ and 0.99 [18]. One can see that this approximation is adequate only at low temperatures. This is due to the fact that the region where Δ is nonzero increases with lowering temperature and, hence, the spatial derivatives of Δ, which are completely neglected in the local-density approximation, become less important.

In the spherically symmetric case of interest, the elementary excitations can conveniently be characterized by the radial quantum number n, angular momentum l, and its projection m onto a chosen quantization axis (z axis). The wave functions of single-particle excitations can then be written as $(U_\nu, V_\nu) = R^{-1}Y_{lm}(\hat{\mathbf{R}})(u_{nl}(R),\ v_{nl}(R))$, where the functions $(u,\ v)$ are normalized as

$$\int_0^\infty (u_{nl}u^*_{n'l} + v_{nl}v^*_{n'l})dR = \delta_{nn'}.$$

The equations for the $u,\ v$ functions immediately follow from the Bogoliubov–de Gennes Eqs. (5) and can be solved numerically. The corresponding $\Delta(R)$ value is given by Eq. (4). However, for the physically most interesting states near the Fermi level, Eqs. (5) can be solved by using the WKB approximation. Namely, in the classically accessible region, the wave functions of these states rapidly oscillate with a period of order $p_F^{-1}(R) \ll R_{TF}$ and a slowly varying amplitude $\tilde{u}_{nl}(R)$, $\tilde{v}_{nl}(R)$:

$$\begin{pmatrix} u_{nl} \\ v_{nl} \end{pmatrix} = \frac{\exp\left(i\tilde{\mu}\int_{R_1}^R p_{Fl}dR\right)}{\sqrt{p_{Fl}(R)}}\begin{pmatrix} \tilde{u}_{nl} \\ \tilde{v}_{nl} \end{pmatrix} + \text{h.c.} \qquad (8)$$

Here, the partial Fermi momentum is defined as $p_{Fl}(R) = (1 - R^2 - (l + 1/2)^2/\tilde{\mu}^2R^2)^{1/2}$, with $\tilde{\mu} = 2\mu/\Omega \gg 1$, and the turning points $R_{1,2}$ specifying the classically accessible region $R_1 < R < R_2$ are found from the equation $p_{Fl}(R_{1,2}) = 0$. Neglecting the terms of the order of $\tilde{\mu}^{-1}$ in Eqs. (5), one gets two decoupled equations for the amplitudes $f_\pm = \tilde{u} \pm i\tilde{v}$:

$$\left[-\left(p_{Fl}\frac{d}{dR}\right)^2 + \hat{\Delta}^2 \pm p_{Fl}\frac{d\hat{\Delta}}{dR} - \hat{\varepsilon}_{nl}^2\right]f_{nl\pm} = 0, \qquad (9)$$

where $\hat{\varepsilon}_{nl} = \varepsilon_{nl}/\Omega \geq 0$ and $\hat{\Delta} = \Delta/\Omega$.

In the classically inaccessible regions $0 < R < R_1$ (due to the centrifugal potential) and $R > R_2$ (due to the trapping potential), Eqs. (8) and (9) should be modified by substituting, respectively, $\mp i|p_{Fl}(R)|$ for $p_{Fl}(R)$, in order that the solutions be decreasing.

At temperatures above T_c, the order parameter is zero; by writing the chemical potential μ as $\mu = (j + 3/2)\Omega$ with some integer j, one can readily obtain from Eq. (9) the well-known result $\varepsilon_{nl}^{(0)} = |2n + l - j|\Omega$ for the energies of particle ($2n + l \geq j$, $\tilde{v}_{nl} = 0$) and hole ($2n + l \leq j$, $\tilde{u}_{nl} = 0$) excitations.

The appearance of a nonzero order parameter $\Delta(R)$ below the transition temperature modifies the energy spectrum. At temperatures close to T_c, the order parameter is small and is nonzero only in a small central part of radius $l_\Delta \ll 1$ in the gas cloud [see Eq. (4)]. Because of this, the presence of nonzero $\Delta(R)$ only affects the excitations with small orbital angular momenta l, only slightly increasing their eigenvalues. The correspond-

ing shift is on the order of $\delta = \Delta(R_1)l_\Delta$, i.e., much smaller than the maximum value $\Delta(0)$ of the spatially inhomogeneous gap $\Delta(R)$, for which reason the lowest energy excitations (for which $\varepsilon_{nl}^{(0)} = 0$ at $T > T_c$) fall inside the gap: $\varepsilon_{nl} \sim \delta \ll \Delta(0)$.

At lower temperatures, the spatial scale of the order parameter becomes comparable with the gas-cloud size R_{TF}, so that all essential excitations ($l \lesssim \tilde{\mu}/2$) are modified in the presence of the order parameter $\Delta(R)$. The wave functions of the above-gap excitations [$\varepsilon_{nl} > \Delta(R_1)$] are nonzero over the whole classically accessible region $R_1 < R < R_2$, whereas those of the in-gap excitations with energies ε_{nl} much lower than $\Delta(R_1)$ are "extruded" from the central region; these excitations are mainly localized in a potential well formed by the order parameter $\Delta(R)$ (from the inside) and by the trap potential (from the outside, Fig. 3).

Leaving aside rather cumbersome expressions for the wave functions (for details, see [24]), let us write the WKB quantization conditions for the spectrum of single-particle excitations. For the above-gap excitations [$\varepsilon_{nl} > \Delta(R)$], the corresponding condition reads

$$\frac{2}{\pi}\int_{R_1}^{R_2}\frac{\sqrt{\varepsilon_{nl}^2 - \Delta^2(R)}}{p_{Fl}(R)}dR = \varepsilon_{nl}^{(0)}. \qquad (10)$$

For the in-gap excitations, a new critical turning point R_c arises, which is determined from the condition $\varepsilon_{nl} = \Delta(R_c)$ and where the particle undergoes Andreev reflection [29] from the spatially inhomogeneous gap $\Delta(R)$ to transform into a hole and vice versa. Because of this, the quantization conditions become more complicated:

$$(-1)^{j-1}\cos(2\phi) = 2Z^2/(Z^4+1), \qquad (11)$$

where

$$Z = \sqrt{2}\exp\left\{\int_{R_1}^{R_c}\sqrt{\Delta^2(R) - \varepsilon_{nl}^2}/p_{Fl}(R)dR\right\},$$

$$\phi = \int_{R_c}^{R_2}\sqrt{\varepsilon_{nl}^2 - \Delta^2(R)}/p_{Fl}(R)dR.$$

The wave functions of these states are mainly concentrated in the region $R_c < R < R_2$, where the amplitudes $\tilde{u}_{nl}$ and $\tilde{v}_{nl}$ oscillate, and exponentially decrease at $R_1 < R < R_c$ (Fig. 3). Note that the appearance of the in-gap excitations is entirely due to the spatial inhomogeneity of $\Delta(R)$, so that, to some degree, they are analogous to the in-vortex localized states in usual superconductors [30].

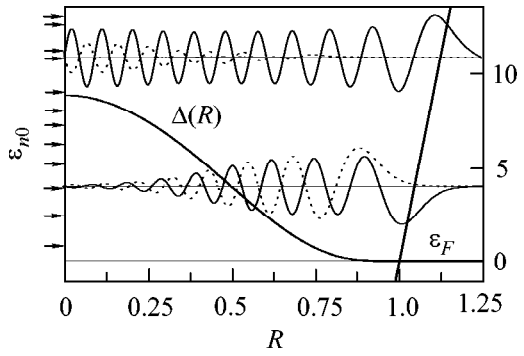

Fig. 3. Wave functions (solid lines) U_{n0} and (dotted lines) V_{n0} for the above-gap and in-gap excitations, as obtained by the numerical solution of Eq. (5) for $l = 0$ at $T = 0$. To reduce the number of oscillations, $\tilde{\mu} = 63$ is taken instead of the actual $\tilde{\mu} \approx 970$ value corresponding to $T_c^{(0)}/\Omega = 5$ and $\lambda = 0.3$. The arrows at the vertical axis indicate the energy eigenvalues for single-particle excitations.

One can see from the above formulas that the energies of single-particle excitations become temperature-dependent below the transition temperature and are no longer multiples of the trap frequency Ω. Because of this, if the response of the gas cloud to an external periodic perturbation is mostly determined by the single-particle excitations, the above-transition resonance structure of this response will be smeared upon passing through the transition point, the lower the temperature the larger the smearing (see, e.g., [31]).

Let us now turn to the low-energy collective excitations. It is natural to expect that, at low temperatures (but higher than the superfluid transition point), the collisionless regime prevails in a Fermi gas. This implies that the period $2\pi/\Omega$ of oscillations in the trap is much shorter than the characteristic collisional frequency in a degenerate Fermi gas. In order of magnitude, this frequency is equal to $\tau^{-1} \sim na^2 v_F (T_c/\varepsilon_F)^2 \sim \lambda^2 T_c^2/\varepsilon_F$, where $na^2 v_F$ is the collisional frequency in a classical gas and the factor $(T_c/\varepsilon_F)^2$ arises due to the Pauli exclusion principle. For this reason, a criterion for the collisionless regime takes the form $\Omega\tau \sim \lambda^{-2}(\Omega/T_c)\exp(1/\lambda) \gg 1$.

The corresponding collective excitations in a normal phase (zero sound) were analyzed using the sum rule in [15] (see also [16]), where, in particular, the eigenfrequencies ω_{nl} were calculated for the lowest monopole $\omega_{00} \approx 2\Omega$ and quadrupole $\omega_{02} \approx \sqrt{2}\,\Omega$ modes. Small deviations from equilibrium in a superfluid gas can

be studied [25] based on the steady-state Bogoliubov–de Gennes equations

$$i\frac{\partial}{\partial t}\begin{pmatrix} U_\nu(\mathbf{r}, t) \\ V_\nu(\mathbf{r}, t)\end{pmatrix} = H_0\begin{pmatrix} U_\nu(\mathbf{r}, t) \\ -V_\nu(\mathbf{r}, t)\end{pmatrix} - \Delta(\mathbf{r}, t)\begin{pmatrix} V_\nu(\mathbf{r}, t) \\ U_\nu(\mathbf{r}, t)\end{pmatrix} \quad (12)$$

in combination with the self-consistency condition

$$\Delta(\mathbf{r}, t) = |V|\sum_\nu U_\nu(\mathbf{r}, t)V_\nu^*(\mathbf{r}, t)\tanh\frac{\varepsilon_\nu}{2T}. \quad (13)$$

It is assumed that the time-dependent order parameter and wave functions tend with $t \longrightarrow -\infty$ to their equilibrium values $\Delta(\mathbf{r}, t) \longrightarrow \Delta_0(\mathbf{r})$ and $(U_\nu(\mathbf{r}, t), V_\nu(\mathbf{r}, t)) \longrightarrow (U_\nu(\mathbf{r}), V_\nu(\mathbf{r}))\exp(-i\varepsilon_\nu t)$, respectively, where $U_\nu(\mathbf{r})$ and $V_\nu(\mathbf{r})$ are the wave functions of single-particle excitations with energies $\varepsilon_\nu \geq 0$ [the solutions of the steady-state Bogoliubov–de Gennes Eq. (5) with $\Delta = \Delta_0(\mathbf{r})$].

The low-energy collective excitations correspond to small fluctuations in the phase of the order parameter (Bogoliubov sound). In this case, $\Delta(\mathbf{r}, t) = \Delta_0(\mathbf{r})\exp(2i\varphi(\mathbf{r}, t)) \approx \Delta_0(\mathbf{r})(1 + 2i\varphi(\mathbf{r}, t))$, where $\varphi(\mathbf{r}, t) \ll 1$ is a real function slowly varying in space and with time. Equation (13) can be solved using perturbation theory, after which the substitution of the resulting solution into Eq. (12) brings about the following equation for $\varphi_\omega(\mathbf{r}) = \int dt\, \varphi(\mathbf{r}, t)\exp(i\omega t)$:

$$\Delta_0(\mathbf{r})\varphi_\omega(\mathbf{r}) = |V| \times \sum_{\nu, \nu_1}\left\{\frac{U_{\nu_1}(\mathbf{r})V_\nu^*(\mathbf{r})}{\omega - \varepsilon_{\nu_1} + \varepsilon_\nu + i0}M^{(1)}_{\nu_1\nu}(\omega)\left[\tanh\frac{\varepsilon_{\nu_1}}{2T} - \tanh\frac{\varepsilon_\nu}{2T}\right] + \left[\frac{U_{\nu_1}(\mathbf{r})U_\nu(\mathbf{r})}{\omega - \varepsilon_{\nu_1} - \varepsilon_\nu + i0}M^{(2)*}_{\nu_1\nu}(-\omega) - \frac{V_{\nu_1}^*(\mathbf{r})V_\nu^*(\mathbf{r})}{\omega + \varepsilon_{\nu_1} + \varepsilon_\nu + i0}M^{(2)}_{\nu_1\nu}(\omega)\right]\tanh\frac{\varepsilon_\nu}{2T}\right\}, \quad (14)$$

where

$$M^{(2)}_{\nu_1\nu}(\omega) = \int_{\mathbf{r}}\Delta_0\varphi_\omega(U_{\nu_1}U_\nu + V_{\nu_1}V_\nu),$$

$$M^{(1)}_{\nu_1\nu}(\omega) = \int_{\mathbf{r}}\Delta_0\varphi_\omega(U^*_{\nu_1}V_\nu - V^*_{\nu_1}U_\nu) = -M^{(1)*}_{\nu\nu_1}(-\omega).$$

At $(T_c - T)/T_c \ll 1$, Eq. (14) can be transformed to

$$-\frac{7\zeta(3)}{6\pi^3}\frac{\Omega^2}{T_c}\left(\frac{1}{\sqrt{1-R^2}}\nabla_{\mathbf{R}}[(1-R^2)^{3/2}\nabla_{\mathbf{R}}\varphi(\mathbf{R})] + 2(1-R^2)\nabla_{\mathbf{R}}\ln\Delta_0\nabla_{\mathbf{R}}\varphi(\mathbf{R})\right) = i\omega\varphi(\mathbf{R}), \quad (15)$$

where $\mathbf{R} = \mathbf{r}/R_{TF}$, whence it follows that the eigenfrequencies ω are purely imaginary at $T \approx T_c$. This signifies that the collective modes rapidly decay into pairs of single-particle excitations.

For $T \ll T_c$, Eq. (14) can be recast in the form

$$-\frac{\Omega^2}{3}\frac{1}{\sqrt{1-R^2}}\nabla_{\mathbf{R}}[(1-R^2)^{3/2}\nabla_{\mathbf{R}}\varphi] = \omega^2\varphi, \quad (16)$$

where only the leading terms are retained in the expansion in powers of gradients and frequency. One can see from this equation that the eigenfrequencies of the collective modes are real and equal, in order of magnitude, to the trap frequency Ω. When excited at $T \ll T_c$, these collective modes bring about oscillations of the superfluid current $\mathbf{j} = (i/m)\sum_\nu(V_\nu^*\nabla V_\nu - V_\nu\nabla V_\nu^*) = (n/m)\nabla\varphi$ and density $n = 2\sum_\nu|V_\nu|^2 = n_0 + \delta n$. The latter are related by the particle number equation $\partial\delta n/\partial t + \mathrm{div}\mathbf{j} = 0$, which directly follows from Eqs. (12) and (13). As a result, the gas cloud oscillates as a whole:

$$n(\mathbf{r}, t) = n_0(\mathbf{r}) + \delta n(\mathbf{r}, t) \approx \left[1 + \frac{1}{m}\nabla^2 f\right]n_0\left(\mathbf{r} + \frac{1}{m}\nabla f\right),$$

where $f(\mathbf{r}, t) = \int^t \varphi(\mathbf{r}, t')dt'$.

Equation (16) does not describe the damping of collective modes. This damping is mainly caused by the inelastic scattering of low-energy in-gap excitations from the collective modes or by the decay of a collective mode into two in-gap single-particle excitations (for a more detailed discussion of analogous mechanisms in a trapped Bose gas, see [32]). In both cases, the energy of the collective mode transforms into the normal component (composed of the in-gap excitations) at the periphery of the gas cloud. Inasmuch as the wave functions of in-gap excitations exponentially decay in the central part of the gas cloud, where the superfluid component is mainly concentrated, the coupling between the fluctuations of order parameter and the in- gap single-particle excitations is exponentially weak [$\sim\exp(-T_c/\Omega)$]. One can thus expect that the damping of collective modes will be weak.

Equation (16) can also be obtained by the quantization of the hydrodynamic motion of a superfluid Fermi gas. For a low superfluid velocity $\mathbf{v}_s = m^{-1}\nabla\varphi$ and small

deviation δn of the particle number density from its equilibrium distribution $n_0(r)$, the corresponding Hamiltonian has the form

$$H_h = \int d\mathbf{r}\left\{\frac{1}{2}mn\mathbf{v}_s^2 + U(n)\right\} \approx \int d\mathbf{r}\left\{\frac{1}{2m}n_0(\nabla\varphi)^2 + \frac{1}{2}U''(n_0)\delta n^2 + U(n_0)\right\}, \quad (17)$$

where $U(n)$ is the density-dependent part of the energy, with the equilibrium distribution n_0 satisfying the condition $U'(n_0) = 0$. In the Thomas–Fermi approximation, one has

$$U(n) = \frac{3}{10}(3\pi^2)^{2/3}\frac{n^{5/3}}{m} + \left(\frac{m\Omega^2 r^2}{2} - \mu\right)n, \quad (18)$$

where the first term corresponds to the energy of a filled Fermi sphere. One then arrives at the following expression for the equilibrium distribution: $n_0(r) = (p_F^3/3\pi^2)(1 - (r/R_{TF})^2)^{3/2}$. Note that the interparticle interaction and Cooper pairing effects are omitted in Eq. (18), because they are proportional to the small parameters λ and $(T_c/\varepsilon_F)^2$, respectively. For the $U''(n_0)$ quantity in Eq. (17), one has $U''(n_0) = (3\pi^2)^{-2/3}N(r)^{-1}$, where $N(r) = (mp_F/\pi^2)\sqrt{1 - (r/R_{TF})^2}$ is the density of states at the local Fermi surface. Using standard commutation relations $[\delta n(\mathbf{r}_1), \varphi(\mathbf{r}_2)] = i\delta(\mathbf{r}_1 - \mathbf{r}_2)$, one gets

$$\partial\varphi/\partial t = i[H_h, \varphi] = U''(n_0)\delta n,$$

$$\partial(\delta n)/\partial t = i[H_h, \delta n] = -\nabla(n_0\nabla\varphi).$$

It is then straightforward to obtain Eq. (16) for the phase fluctuation and the equation

$$\frac{\partial^2}{\partial t^2}\delta n + \frac{\Omega^2}{3}\nabla_{\mathbf{R}}\left[(1 - R^2)^{3/2}\nabla_{\mathbf{R}}\frac{\delta n}{\sqrt{1 - R^2}}\right] = 0 \quad (19)$$

for the density fluctuation.

Equation (16) [or (19)], together with the condition for finiteness of φ (or δn) at any $R \le 1$, determines the energy spectrum of the collective modes

$$(\omega_{nl}/\Omega)^2 = l + \frac{4}{3}n(n + l + 2), \quad l = 0, 1, 2, \ldots \quad (20)$$

and the corresponding eigenfunctions

$$\varphi_{nl}(\mathbf{R}) \propto R^l {}_2F_1\left(-n, n + l + 2; \frac{3}{2} + l; R^2\right)Y_{lm}(\theta, \phi), \quad (21)$$

where ${}_2F_1$ is the hypergeometric function, l is the orbital angular momentum of the collective mode, and n is an integer ($n = 0, 1, 2, \ldots$ for nonzero l, and $n = 1, 2, \ldots$ for $l = 0$). Note that eigenfunctions (21) are mutually orthogonal with weight $1/\sqrt{1 - R^2}$. It is also worth noting that spectrum (20) coincides with the eigenfrequency spectrum of a normal Fermi gas in the hydrodynamic (collisional) regime [14]. This is not surprising because the contribution of the superfluid pairing, to hydrodynamic Hamiltonian (17), as already noted, is small.

We are now in a position to compare the eigenfrequencies of the collective modes of a normal Fermi gas in the collisionless regime above T_c with the eigenfrequencies of the collective modes of a superfluid gas at $T \ll T_c$. Of particular experimental interest are the lowest energy modes, because they can easily be excited by modulating the trap frequencies. [A small perturbation of the external potential $V_{\text{ext}}\exp(-i\omega t)$ appears as an additional term $-i\omega V_{\text{ext}}\exp(-i\omega t)$ on the right-hand side of Eq. (16)]. It follows from Eq. (20) that the lowest eigenfrequency ω_{10} of a monopole "breathing" mode ($l = 0$ and $n = 1$) in the superfluid phase is equal to 2Ω (this result can also be derived from the sum rule),[1] while the lowest frequency ω_{01} of a dipole mode ($l = 1$ and $n = 0$), as expected, is equal to the trap frequency Ω (this mode corresponds to the gas-cloud motion as a whole in the external harmonic trap potential). Therefore, these eigenfrequencies coincide with the frequencies of collective oscillations calculated in [15] for a normal Fermi gas in the collisionless regime. At the same time, the frequencies of the energetically lowest quadrupole modes are different: for the superfluid phase, Eq. (20) gives $\omega_{02} = \sqrt{2}\,\Omega$, whereas for the normal phase in the collisionless regime, this value is 2Ω [15]. Experimentally, the quadruple mode can be excited by a weak out-of-phase modulation of the trap frequency, e.g., in the x and y directions: $V_{\text{ext}}(\mathbf{r}, t) = (m\Omega^2/2)(x^2 - y^2)\zeta\cos(\omega t)$, where $\zeta \ll 1$. In this case, the gas response will exhibit resonances in the amplitude of density oscillations at frequencies corresponding to the collective oscillations. For $T > T_c$, the energetically lowest resonance will occur at a frequency of 2Ω, whereas for $T \ll T_c$ it will be seen at $\sqrt{2}\,\Omega$. (At temperatures close to critical, the resonance peak will be strongly smeared, because the damping of collective modes in this region is strong). Such a behavior of the resonance line will serve as strong evidence for the appearance of superfluid ordering in the system. (As pointed out above, additional evidence could be provided by a change in the behavior of single-particle excitations).

It should be emphasized that the problem of experimental detection of the appearance of a superfluid phase in a trapped Fermi-gas system is not as obvious as it might seem, because, contrary to the Bose gas, where the Bose condensation is accompanied by a clearly defined change in the density distribution, a change in the density distribution upon the superfluid transition in a Fermi gas is quite insignificant, so that

[1] A.J. Leggett, private communication.

direct optical detection of the transition is hardly possible. Apart from the two above-mentioned methods, possible methods of revealing the presence of a superfluid phase were also discussed in works [33, 34]. In the first of them, the superfluid transition was suggested to be detected by a change in small-angle scattering of a nonresonant laser beam from a gas cloud, and in the second work, by a change in its moment of inertia.

I am grateful to J.T.M. Walraven, L. Vichi, Yu. Kagan, M.Yu. Kagan, A.J. Leggett, D.S. Petrov, and G.V. Shlyapnikov for helpful and stimulating discussions. This work was supported by the Russian Foundation for Basic Research, project no. 97-02- 16532.

REFERENCES

1. M. H. Anderson, J. R. Ensher, M. R. Matthews, *et al.*, Science **269**, 198 (1995).
2. C. C. Bradley, C. A. Sackett, J. J. Tolett, and R. G. Hulet, Phys. Rev. Lett. **75**, 1687 (1995).
3. K. B. Davis, M.-O. Mewes, M. R. Andrews, *et al.*, Phys. Rev. Lett. **75**, 3969 (1995).
4. F. Dalfovo, S. Giorgini, L. P. Pitaevskii, and S. Stringari, Rev. Mod. Phys. **71**, 463 (1999).
5. W. C. Stwalley, Phys. Rev. Lett. **37**, 1628 (1976); E. Tiesinga, D. J. Verhaar, and H. T. C. Stoof, Phys. Rev. A **47**, 4114 (1993); P. O. Fedichev, Yu. Kagan, G. V. Shlyapnikov, and J. T. M. Walraven, Phys. Rev. Lett. **77**, 2913 (1996).
6. B. DeMarco, J. L. Bohn, J. P. Burke, Jr., *et al.*, Phys. Rev. Lett. **82**, 4208 (1999).
7. M. J. Holland, B. DeMarco, and D. S. Jin, Phys. Rev. A **61**, 053610 (2000).
8. L. Viverit, S. Giorgini, L. P. Pitaevskii, and S. Stringari, cond-mat/0005517.
9. B. DeMarco and D. S. Jin, Science **285**, 1703 (1999).
10. Th. Busch, J. R. Anglin, J. I. Cirac, and P. Zoller, Europhys. Lett. **44**, 1 (1998).
11. B. DeMarco and D. S. Jin, Phys. Rev. A **58**, R4267 (1998).
12. J. Ruostekoski and J. Javanainen, Phys. Rev. Lett. **82**, 4741 (1999).
13. G. Ferrari, Phys. Rev. A **59**, R4125 (1999).
14. G. M. Bruun and C. W. Clark, Phys. Rev. Lett. **83**, 5415 (1999).
15. L. Vichi and S. Stringari, Phys. Rev. A **60**, 4734 (1999).
16. L. Vichi, cond-mat/0006305.
17. E. R. I. Abraham, W. I. McAlexander, J. M. Gerton, *et al.*, Phys. Rev. A **55**, R3299 (1997).
18. H. T. C. Stoof, M. Houbiers, C. A. Sackett, and R. G. Hulet, Phys. Rev. Lett. **76**, 10 (1996).
19. J. L. Bohn, cond-mat/9911132.
20. M. Houbiers, R. Ferwerda, H. T. C. Stoof, *et al.*, Phys. Rev. A **56**, 4864 (1997).
21. M. A. Baranov, Yu. Kagan, and M. Yu. Kagan, Pis'ma Zh. Éksp. Teor. Fiz. **64**, 273 (1996) [JETP Lett. **64**, 301 (1996)].
22. L. You and M. Marinescu, Phys. Rev. A **60**, 2324 (1999).
23. M. A. Baranov and D. S. Petrov, Phys. Rev. A **58**, R801 (1998).
24. M. A. Baranov, Pis'ma Zh. Éksp. Teor. Fiz. **70**, 392 (1999) [JETP Lett. **70**, 396 (1999)]; cond-mat/9801142.
25. M. A. Baranov and D. S. Petrov, Phys. Rev. A **62**, 041601 (2000).
26. G. M. Bruun, Y. Castin, R. Dum, and K. Burnett, Eur. Phys. J. D **7**, 433 (1999).
27. L. P. Gor'kov and T. K. Melik-Barkhudarov, Zh. Éksp. Teor. Fiz. **40**, 1452 (1961) [Sov. Phys. JETP **13**, 1018 (1961)].
28. G. Eilenberger, Z. Phys. B **214**, 195 (1968).
29. A. F. Andreev, Zh. Éksp. Teor. Fiz. **46**, 1823 (1964) [Sov. Phys. JETP **19**, 1228 (1964)].
30. C. Caroli, P. G. de Gennes, and J. Matricon, Phys. Lett. **9**, 307 (1964).
31. G. M. Bruun and C. W. Clark, cond-mat/9906392.
32. P. O. Fedichev, G. V. Shlyapnikov, and J. T. M. Walraven, Phys. Rev. Lett. **80**, 2269 (1998), and references therein.
33. F. Weig and W. Zwerger, Europhys. Lett. **49**, 282 (2000).
34. F. Zambelli and S. Stringari, cond-mat/0004325.

Translated by V. Sakun

JETP Letters, Vol. 72, No. 7, 2000, pp. 393–399. Translated from Pis'ma v Zhurnal Éksperimental'noĭ i Teoreticheskoĭ Fiziki, Vol. 72, No. 7, 2000, pp. 566–576.

Reduced Models and Noncommutative Gauge Theories

Yu. M. Makeenko

Institute of Theoretical and Experimental Physics, Bol'shaya Cheremushkinskaya ul. 25, Moscow, 117259 Russia

e-mail: makeenko@itep.ru

Received September 12, 2000

A brief review of the relation between reduced models and noncommutative Yang–Mills (NCYM) theory is given. The twisted Eguchi–Kawai model, the mapping onto NCYM, the Morita equivalence, the fundamental matter, the Wilson loops in NCYM, and the *D*-brane interpretation are considered. © *2000 MAIK "Nauka/Interperiodica".*

PACS numbers: 11.15.Pg; 11.25.Sq

The interest that has arisen recently in the noncommutative gauge theories was inspired by the paper [1] devoted to the compactification of matrix theory [2, 3].[1] Matrix theory belongs to the class of reduced models [5] for which the (infinite) matrices are independent of space coordinates, whereas this dependence appears upon the expansion in the vicinity of a classical vacuum. For the reduced models to be equivalent at large N to the quantum field theory in the t'Hooft continuous space–time limit, they must be either "frozen" [6] or twisted [7–10].

It was recently realized [11] that the twisted reduced models have a limit where they describe quantum field theories on a noncommutative space with coordinate operators $\hat{x}^\mu$, satisfying commutation relations

$$[\hat{x}^\mu, \hat{x}^\nu] = i\theta^{\mu\nu}\hat{1}. \quad (1)$$

Field multiplication is specified by a product,

$$\phi_1(x) * \phi_2(x) \stackrel{\text{def}}{=} \phi_1(x)\exp\left\{\frac{i}{2}\overleftarrow{\partial}_\mu\theta_{\mu\nu}\overrightarrow{\partial}_\nu\right\}\phi_2(x), \quad (2)$$

possessing the associativity property. The action of the noncommutative $U_\theta(1)$ gauge theory is defined as

$$S = \frac{1}{4e^2}\int \mathcal{F}^2, \quad (3)$$

where

$$\mathcal{F}_{\mu\nu} = \partial_\mu A_\nu - \partial_\nu A_\mu - i(A_\mu * A_\nu - A_\nu * A_\mu) \quad (4)$$

is the noncommutative gauge field strength. The planar limit of the Yang–Mills $U(N)$ theory corresponds to $\theta \longrightarrow \infty$ [9]. This relation between the twisted reduced models and the noncommutative gauge theories was revealed in [12–16]. In particular, the appropriate observables were constructed for the noncommutative gauge theories.

In this paper, a review of the relation between the twisted reduced models and the noncommutative gauge theories is presented. Special attention is given to the equivalence of some noncommutative and ordinary (or "commutative") gauge theories, which is known as Morita equivalence [17]. The simplest example is provided by the above-mentioned equivalence of the noncommutative $U_\theta(1)$ gauge theory in the limit of large θ to the ordinary Yang–Mills $U(N)$ theory in the limit of large N. Another example is that the noncommutative $U_\theta(1)$ gauge theory in a box with periodic boundary conditions and rational values of the dimensionless noncommutativity parameter is equivalent to the ordinary Yang–Mills theory in a box of a smaller size with twisted boundary conditions that define the non-Abelian gauge field flux, known as t'Hooft flux [18]. These results are based on a twisted reduced finite-N model mapped onto the noncommutative gauge theory on a finite-space lattice, for which reason they are rigorous for the regularized quantum field theory. Twisted reduced model [19] is used for the generalization of the Morita equivalence to the case when the matter fields are given in the fundamental representation of the gauge group. The observables in the noncommutative gauge theory are expressed through continual integrals over the fundamental matter fields for both closed and open Wilson loops. The Morita equivalence is described as a T-duality in *D*-brane terms.

TWISTED EGUCHI–KAWAI MODEL

1. Definition [9]. The twisted Eguchi–Kawai (TEK) model is constructed of D unitary $N \times N$ matrices U_μ^{ij}

[1] For a review of matrix theory, see [4].

($\mu = 1, \ldots, D$). The partition function

$$Z_{\mathrm{TEK}} = \int \prod_{\mu} dU_{\mu} \times \exp\left\{ \frac{1}{2g^2} \sum_{\mu \neq \nu} Z^*_{\mu\nu} \mathrm{tr} U_{\mu} U_{\nu} U^{\dagger}_{\mu} U^{\dagger}_{\nu} + \mathrm{h.c.} \right\} \tag{5}$$

belongs to the type of Wilson lattice gauge theory[2] on a unit hypercube with twisted boundary conditions. The $Z_{\mu\nu}$ factor has the form

$$Z_{\mu\nu} = e^{4\pi i n_{\mu\nu}/N} \in \mathbb{Z}_N \quad (\text{integer } n_{\mu\nu} = -n_{\nu\mu}), \tag{6}$$

where N is assumed to be odd.

The TEK model possesses the following symmetries:

$$\text{gauge:} \quad U_{\mu} \longrightarrow \Omega U_{\mu} \Omega^{\dagger}, \tag{7}$$

$$\mathbb{Z}_N^D: \quad U_{\mu} \longrightarrow Z_{\mu} U_{\mu} \quad (Z_{\mu} \in \mathbb{Z}_N). \tag{8}$$

To a gauge transformation, the vacuum state is specified by the matrices

$$U^{\mathrm{cl}}_{\mu} = \Gamma_{\mu}, \tag{9}$$

where Γ_{μ} are twistors satisfying the Weyl–t'Hooft commutation relation

$$\Gamma_{\mu} \Gamma_{\nu} = Z_{\mu\nu} \Gamma_{\mu} \Gamma_{\nu}. \tag{10}$$

Their explicit forms are known for any $n_{\mu\nu}$.

The simplest twist corresponds to

$$n_{\mu\nu} = L^{D/2-1} \varepsilon_{\mu\nu}, \quad \varepsilon_{\mu\nu} = \begin{pmatrix} 0 & +1 & & & \\ -1 & 0 & & & \\ & & 0 & +1 & \\ & & -1 & 0 & \\ & & & & \ddots \end{pmatrix} \tag{11}$$

and $N = L^{D/2}$. The $SU(N)$ group can be represented as a direct product $SU(N) \supset \prod_1^{D/2} \otimes SU(L)$, so that Γ_i, Γ_{i+1} ($i = 1, \ldots, D/2$) can be chosen in the form of Weyl unitary matrices $h^{jk} = \delta^{j+1,k}$ and $g^{jk} = e^{4\pi i(j-1)/L} \delta^{jk}$ for each $SU(L)$. For this simplest twist, $\Gamma_{\mu}^L = 1$.

2. Continuous limit of the TEK model [10]. This limit is achieved when the lattice constant $a \longrightarrow 0$ ($N \longrightarrow \infty$), so that

$$U_{\mu} = e^{iaA_{\mu}}, \quad \Gamma_{\mu} = e^{ia\gamma_{\mu}}, \tag{12}$$

where A_{μ} and γ_{μ} are (infinite) Hermitian matrices. Then, Eq. (10) transforms to the Heisenberg commutator:

$$[\gamma_{\mu}, \gamma_{\nu}] = iB_{\mu\nu}, \quad B_{\mu\nu} = 4\pi n_{\mu\nu}/Na^2. \tag{13}$$

The action in the continuous TEK model becomes

$$S = \frac{1}{4g^2} \mathrm{tr}([A_{\mu}, A_{\nu}] - iB_{\mu\nu})^2, \tag{14}$$

and the vacuum configuration takes the form

$$A^{\mathrm{cl}}_{\mu} = \gamma_{\mu}, \tag{15}$$

to a gauge transformation $A_{\mu} \longrightarrow \Omega A_{\mu} \Omega^{\dagger}$. At large N, the Wilson loops in the Yang–Mills theory are represented as

$$W(C) = \left\langle \frac{1}{N} \mathrm{tr} \mathrm{P} \exp\left\{ -i \int_C \mathrm{d}\xi^{\mu} \gamma_{\mu} \right\} \times \frac{1}{N} \mathrm{tr} \mathrm{P} \exp\left\{ i \int_C \mathrm{d}\xi^{\mu} A_{\mu} \right\} \right\rangle_{\mathrm{TEK}}, \tag{16}$$

where averaging means integration over the (infinite) A_{μ} matrices with action given by Eq. (14). The Wilson loops are nontrivial, because the A_{μ} matrices do not commute with each other. For open loops, the first trace on the right-hand side of Eq. (16) vanishes. For closed loops, it takes the form of an exponential function of the $B_{\mu\nu}$ field flux through a surface bounded by the contour C.

3. Compactification of the reduced models. Compactification of the reduced models on a D-dimensional torus $\mathbb{T}^D$ can be described [1] by imposing the following condition on A_{μ}:

$$A_{\mu} + 2\pi R_{\mu} \delta_{\mu\nu} = \Omega_{\nu} A_{\mu} \Omega^{\dagger}_{\nu}, \tag{17}$$

where Ω_{ν} are unitary matrices. After calculating matrix traces of both sides of Eq. (17), one can see that the solution is possible only for the infinite matrices (=Hermitian operators).

Taking the exponential of Eq. (17) multiplied by a dimensional parameter a, one obtains

$$e^{2\pi i a \delta_{\mu\nu} R_{\mu}} U_{\mu} = \Omega_{\nu} U_{\mu} \Omega^{\dagger}_{\nu}, \tag{18}$$

where matrices A_{μ} appear in the exponent in accordance with Eq. (12) and matrices U_{μ} are unitary. Equation (18) is the $N \times N$-matrix discretization of Eq. (17); it has solutions at finite N (the simplest of them is presented below).

Taking matrix traces of both sides of Eq. (18), we see that matrices U_{μ} must be traceless, as is the case for twistors. Calculating the determinant of both sides of Eq. (18), we conclude that $aR_{\mu}N$ must be an integer. Self-consistency of Eq.(18) also requires that

$$\Omega_{\mu} \Omega_{\nu} = z \Omega_{\nu} \Omega_{\mu} \tag{19}$$

[2] For a review of lattice gauge theories, see [20].

with some $z \in \mathbb{Z}_N$. Condition (18) on the unitary matrices U_μ is compatible with gauge symmetry (7) if the gauge transformation matrix Ω commutes with the Ω_ν matrices.

4. Solution at finite *N* [14]. To describe the solution of Eq. (18), it is convenient to introduce the Weyl basis on $gl(N)$:

$$J_k = \Gamma_1^{k_1}\ldots\Gamma_D^{k_D}\exp\left\{2\pi i\frac{1}{N}\sum_{\mu>\nu} n_{\mu\nu}k_\mu k_\nu\right\}, \qquad (20)$$

where the last multiplier provides the symmetry of the matrix product and $J_{L-k} = J_k^\dagger$. A product of two generators is decomposed in this basis as

$$J_k J_q = J_{k+q}\exp\left\{2\pi i\frac{1}{N}\sum_{\mu,\nu} k_\mu n_{\mu\nu} q_\nu\right\}. \qquad (21)$$

The last multiplier is responsible for the noncommutativity.

To construct the solution, we choose

$$\Omega_\mu = \prod_\nu \Gamma_\nu^{m\varepsilon_{\mu\nu}}, \qquad (22)$$

where m is an integer. Then,

$$U_\mu^{(0)} = \Gamma_\mu \qquad (23)$$

is a partial solution of Eq. (18). The general solution of this equation reads

$$U_\mu = V_\mu\Gamma_\mu, \qquad (24)$$

where V_μ obeys the homogeneous equation

$$V_\mu = \Omega_\nu V_\mu \Omega_\nu^\dagger. \qquad (25)$$

A solution of Eq. (25) can be represented in the form

$$V_\mu^{ij} = \sum_{k\in\mathbb{Z}_m} (J_k^n)^{ij} U_\mu(k), \qquad (26)$$

where $n = L/m$ is an integer and k changes from 1 to m because $\Gamma_\mu^L = 1$. Evidently, the V_μ matrix thus constructed commutes with Ω_ν.

Using the specified c-number coefficients $U_\mu(k)$ describing the dynamical degrees of freedom, one can apply a Fourier transform to construct the field

$$\mathcal{U}_\mu(x) = \sum_{k\in\mathbb{Z}_m}\exp\left\{2\pi i\frac{kx}{am}\right\}U_\mu(k), \qquad (27)$$

which is a periodic function on the edges of a lattice of dimension m^D (or, which is equivalent, on a discrete $\mathbb{T}_m^D$ torus). Thus, the spatial dimension of the lattice is $l = am$. The $\mathcal{U}_\mu(x)$ field describes the same degrees of freedom as does the $N\times N$ U_μ^{ij} matrix obeying condition (18). The unitarity condition $U_\mu U_\mu^\dagger = 1$ takes the form

$$\mathcal{U}_\mu(x) * \mathcal{U}_\mu^*(x) = 1, \qquad (28)$$

where $\mathcal{U}_\mu^*$ denotes complex conjugation, and a noncommutative product of functions on a lattice is defined as

$$f(x) * g(x) = \sum_{y,z}\exp\{2i(\theta^{-1})_{\mu\nu}y_\mu z_\nu\} f(x+y)g(x+z), \qquad (29)$$

where

$$\theta_{\mu\nu} = \frac{a^2 mn}{\pi}\varepsilon_{\mu\nu} = \frac{l^2}{\pi}\frac{n}{m}\varepsilon_{\mu\nu}. \qquad (30)$$

These formulas follow from a comparison of expansions (26) and (27) with regard to Eq. (21). At $a \longrightarrow 0$, Eq. (29) reproduces Eq. (2) for a noncommutative product in the continuous limit.

MAPPING ONTO NCYM

The TEK model [generally, with condition (18)] can identically be rewritten in the form of the noncommutative $U_\theta(1)$ gauge theory on a lattice. Making use of relations (26) and (27) between matrices and fields, the TEK action can be recast as

$$S = \frac{1}{2e^2}\times\sum_{x\in\mathbb{T}_m^D}\sum_{\mu\neq\nu}\mathcal{U}_\mu(x) * \mathcal{U}_\nu(x+a\hat{\mu}) * \mathcal{U}_\mu^\dagger(x+a\hat{\nu}) * \mathcal{U}_\nu^\dagger(x), \qquad (31)$$

where $\hat{\mu}$ denotes a unit vector in the μ direction and the coupling constant of the noncommutative $U_\theta(1)$ gauge theory is $e^2 = g^2N$. Similarly, the matrix integration measure dU_μ [satisfying condition (18)] transforms to the Haar measure

$$\prod_\mu dU_\mu \Rightarrow \prod_{x,\mu} d\mathcal{U}_\mu(x). \qquad (32)$$

Action (31) is invariant about the noncommutative gauge transformations:

$$\mathcal{U}_\mu(x) \longrightarrow \omega(x) * \mathcal{U}_\mu(x) * \omega^*(x+a\hat{\mu}), \qquad (33)$$

where $\omega(x)$ satisfies the condition

$$\omega * \omega^* = \omega^* * \omega = 1. \qquad (34)$$

Equation (33) is a counterpart of Eq. (7), and Eq. (34) is a counterpart of the unitarity condition for the Ω matrix.

The ordinary TEK model corresponds to $n = 1$. Then, $\Omega_\mu = \Gamma_\mu^L = 1$ and Eq. (18) becomes trivial. In this case, the results of [9] are reproduced for $N \longrightarrow \infty$ at a fixed a, because $\theta \longrightarrow \infty$, according to Eq. (30). This limit corresponds to the t'Hooft limit of the Yang–Mills theory at large N, when only the planar diagrams survive.

There is another possible continuous limit in the ordinary TEK model (with $n = 1$), namely, when θ remains finite at $N \longrightarrow \infty$ while $a \sim 1/\sqrt{m} = N^{-1/D}$. In this limit, the torus period is $l = am \sim \sqrt{m} = N^{1/D} \longrightarrow \infty$ and, thus, the noncommutative gauge theory is reproduced on $\mathbb{R}^D$ [11].

For $n > 1$ [i.e., for the TEK model with constraint (18)], noncommutativity parameter (30) may remain finite at $N \longrightarrow \infty$ even for a finite l value, provided that the dimensionless noncommutativity parameter $\Theta = n/m$ is finite in this limit. Hence, the noncommutative theory "lives" on the torus [1]. At finite N, the noncommutative lattice gauge theory with action (31) is a lattice regularization of the continuous theory [14]. Since the lattice dimension $l = am$ is finite, the infrared ($p_{\min} = 2\pi/l$) and ultraviolet ($p_{\max} = \pi/a$) cutoff parameters are related to each other as

$$p_{\max}\theta p_{\min} = 2\pi n, \tag{35}$$

which is similar to the relation [21] obtained by perturbation theory for the $\mathbb{R}^4$ space (which corresponds to the limit $N \longrightarrow \infty$ for $n = 1$, see above).

MORITA EQUIVALENCE

The noncommutative gauge theory with a rational value of dimensionless noncommutativity parameter Θ possesses an interesting feature known as the Morita equivalence [17]. We will describe it for the lattice regularization corresponding to the simplest twist (11), assuming that the ratio $m/n = \tilde{p}$ is an integer. Then, the noncommutative $U_\theta(1)$ gauge theory on a periodic lattice of size m^D is equivalent to the ordinary Yang–Mills $U(p)$ theory with $p = \tilde{p}^{D/2}$ on a lattice of size n^D with twisted boundary conditions and the coupling constant $g^2 = e^2/p$ [where e^2 is the coupling constant in the $U_\theta(1)$ theory].

The twisted boundary conditions on a lattice have the form

$$\tilde{V}_\mu(\tilde{x} + an\hat{\nu}) = \tilde{\Gamma}_\nu \tilde{V}_\mu(\tilde{x})\tilde{\Gamma}_\nu^\dagger, \tag{36}$$

where $\tilde{\Gamma}_\nu$ are the $p \times p$ twistors with commutation relations

$$\tilde{\Gamma}_\mu\tilde{\Gamma}_\nu = \tilde{Z}_{\mu\nu}\tilde{\Gamma}_\nu\tilde{\Gamma}_\mu, \quad \tilde{Z}_{\mu\nu} = e^{4\pi i\varepsilon_{\mu\nu}/\tilde{p}} \tag{37}$$

($\tilde{p}$ is assumed to be odd). The factor $\tilde{Z}_{\mu\nu} \in \mathbb{Z}_p$ cannot be removed, because $\tilde{\Gamma}_\mu$ are $SU(p)$ matrices. It is associated with the non-Abelian t'Hooft flux.

In the preceding section, we already discussed the equivalence of the TEK model [in the general case with condition (18)] for $N = (mn)^{D/2}$ to the noncommutative $U_\theta(1)$ gauge theory on $\tilde{\mathbb{T}}_m^D$. Both possess the same m^D degrees of freedom described by either Eq. (26) or Eq. (27). In matrix terms, the noncommutativity arises because

$$J_k^n J_q^n = J_{k+q}^n \exp\left\{2\pi i\frac{n}{m}k_\mu\varepsilon_{\mu\nu}q_\nu\right\}, \tag{38}$$

as follows from general formula (21) for this simplest twist. In noncommutativity terms, it stems from the noncommutative product

$$\begin{aligned}\exp\left\{2\pi i\frac{kx}{l}\right\} * \exp\left\{2\pi i\frac{qx}{l}\right\} \\ = \exp\left\{2\pi i\frac{(k+q)x}{l}\right\}\exp\left\{2\pi i\frac{n}{m}k_\mu\varepsilon_{\mu\nu}q_\nu\right\},\end{aligned} \tag{39}$$

as follows from definition (29).

If $m = \tilde{p}\,n$, then a third equivalent model exists, in which the same degrees of freedom are described by the $p \times p$-matrix field:

$$\tilde{V}_\mu^{ab}(\tilde{x}) = \sum_{k \in \mathbb{Z}_m} \tilde{J}_k^{ab} \exp\left\{2\pi i\frac{k\tilde{x}}{\tilde{p}an}\right\}U_\mu(k), \tag{40}$$

with

$$\tilde{J}_k = \prod_\mu \tilde{\Gamma}_\mu^{k_\mu} \exp\left\{2\pi i\frac{1}{\tilde{p}}\sum_{\mu>\nu}\varepsilon_{\mu\nu}k_\mu k_\nu\right\} \tag{41}$$

similar to Eq. (20). The number of degrees of freedom $n^D p^2 = m^D$ coincide at $p = \tilde{p}^{D/2}$. The noncommutativity now stems from the matrix factor rather than from the x dependence, because

$$\tilde{J}_k\tilde{J}_q = \tilde{J}_{k+q}\exp\left\{2\pi i\frac{1}{\tilde{p}}k_\mu\varepsilon_{\mu\nu}q_\nu\right\}. \tag{42}$$

In the third model, the action coincides with the ordinary Wilson lattice action:

$$\begin{aligned}S = \frac{p}{2e^2}\sum_{\tilde{x}\in\tilde{\mathbb{T}}_n^D}\sum_{\mu\neq\nu}\mathrm{tr}_{(p)}\tilde{V}_\mu(\tilde{x})\tilde{V}_\nu(\tilde{x}+a\hat{\mu}) \\ \times\tilde{V}_\mu^\dagger(\tilde{x}+a\hat{\nu})\tilde{V}_\nu^\dagger(\tilde{x}).\end{aligned} \tag{43}$$

The $\tilde{V}_\mu(\tilde{x})$ field is quasi-periodic on $\tilde{\mathbb{T}}^D_n$ and satisfies twisted boundary conditions (36), because

$$\tilde{\Gamma}_\mu \tilde{J}_k \tilde{\Gamma}^\dagger_\mu = \tilde{J}_k e^{2\pi i k_\mu/\tilde{p}}. \quad (44)$$

For $n = 1$, when $\tilde{p} = m$ and $p = N$, the third model lives on a unit hypercube with twisted boundary conditions and coincides with the TEK model. This becomes evident after the substitution $U_\mu = \tilde{V}_\mu \tilde{\Gamma}_\mu$. As a matter of fact, the TEK model was originally motivated in [9] precisely by this formulation. Therefore, the deduction of the noncommutative gauge theories from the TEK model is the simplest example of the Morita equivalence.

In the continuous limit ($N \longrightarrow \infty$), when the TEK model is formulated through operators, the noncommutative $U_\theta(1)$ gauge theory lives on $\mathbb{T}^D$ with a period of l. At a rational value of Θ, it is Morita-equivalent to the ordinary $U(p)$ gauge theory on a smaller torus $\tilde{\mathbb{T}}^D$ with twisted boundary conditions and a period of $\tilde{l} = l/\tilde{p}$. The lattice regularization renders these results rigorous [15]. For a twist of a more general type, one can obtain an arbitrary (rational or irrational) value of Θ. It is also shown in [16] that, rather than imposing constraint (18), the theories on torus can be obtained from the TEK model by choosing a more complex twist.

FUNDAMENTAL MATTER [15]

One can generalize the results of the two preceding sections by including matter. Let $\phi(x)$ be a scalar field of the matter in the fundamental representation of $U_\theta(1)$. The corresponding term in the action

$$S_{matter} = -\sum_{x,\mu} \phi^*(x) * \mathcal{U}_\mu(x) * \phi(x + a\hat{\mu}) + M^2 \sum_x \phi^*(x)\phi(x) \quad (45)$$

is invariant about the noncommutative gauge transformations

$$\phi(x) \longrightarrow \omega(x) * \phi(x), \quad \phi^*(x) \longrightarrow \phi^*(x) * \omega^*(x) \quad (46)$$

and transformation (33) for $\mathcal{U}_\mu(x)$.

For rational Θ values, action (45) on a torus is Morita-equivalent to the action

$$S_{matter} = -\sum_{\tilde{x},\mu} \mathrm{tr}_{(p)} \Phi^*(\tilde{x}) \tilde{V}_\mu(\tilde{x}) \Phi(\tilde{x} + a\hat{\mu}) + M^2 \sum_{\tilde{x}} \mathrm{tr}_{(p)} \Phi^*(\tilde{x})\Phi(\tilde{x}), \quad (47)$$

where the notations are as in the preceding section and the $p \times p$-matrix field $\Phi^{ij}(\tilde{x})$ satisfies the twisted boundary conditions

$$\Phi(\tilde{x} + \tilde{l}\hat{\nu}) = \tilde{\Gamma}_\nu \Phi(\tilde{x}) \tilde{\Gamma}^\dagger_\nu \quad (48)$$

similar to Eq. (36) for the gauge field. The indices i and j at the Φ^{ij} matrix stand for color and flavor, respectively (distinguishing between the quark types in the standard QCD notations). The color symmetry is local, whereas the flavor symmetry is global. In particular, for n =1, model (47) coincides with the TEK model for the fundamental matter considered in [19].

The continuous limit for the foregoing formulas is evident. The continuous $U_\theta(1)$ gauge theory with fundamental matter (noncommutative QED) is reproduced at $N \longrightarrow \infty$. In the $\theta \longrightarrow \infty$ limit, it is equivalent to QCD on $\mathbb{R}^D$ at large N in the Veneziano limit, for which the flavor number of the fundamental matter fields is proportional to the color number, so that the matter survives at large N. These results are also rigorous, because they are obtained for the regularized theory.

WILSON LOOPS IN NCYM

In the ordinary Yang–Mills theory, the observables can be expressed through the Wilson loops. The standard way of deducing the corresponding formulas consists of averaging over matter fields by calculating a Gaussian continual integral. This approach can also be applied to the noncommutative gauge theory with fundamental matter specified by action (45). On a lattice, one can also use an expansion in $1/M^2$ powers. In this section, we describe the types of Wilson loops appearing for such a procedure.

The contour C composed of J lattice edges is defined as a (ordered) set of unit vectors $\hat{\mu}_j$ directed along the edges j ($j = 1, \ldots, J$) forming the contour. In the presence of the gauge field, a parallel translation from the point x to the point $x + \ell$ ($\ell = a\sum_j \hat{\mu}_j$) along the contour C is described by the expression

$$\mathcal{U}(x; C) = \mathcal{U}_{\mu_1}(x) * \mathcal{U}_{\mu_2}(x + a\hat{\mu}_1) * \mathcal{U}_{\mu_J}\left(x + a\sum_{j=1}^{J-1} \hat{\mu}_j\right), \quad (49)$$

which is covariant about the noncommutative gauge transformation (33):

$$\mathcal{U}(x; C) \longrightarrow \omega(x) * \mathcal{U}(x; C) * \omega^*(x + \ell). \quad (50)$$

If a function $S_\ell(x)$ has the property

$$S_\ell(x) * \omega(x) * S^*_\ell(x) = \omega(x + \ell), \quad (51)$$

then one can easily show that

$$W(C) = \sum_x S_\ell(x) * {}^{\mathcal{O}}\mathcal{U}(x; C) \tag{52}$$

is invariant about the noncommutative gauge transformations. The solution of Eq. (51) reads

$$S_\ell(x) = \exp\{i\ell_\mu \theta^{-1}_{\mu\nu} x_\nu\}, \tag{53}$$

where $\ell_\mu = anj_\mu$ with an integer vector j_μ (with an accuracy of possible winding round the torus).

The continuous limit of Eq. (52) defines the Wilson loops (invariant about the noncommutative gauge transformations) for the noncommutative Wilson theory. Apart from the closed loops on $\mathbb{R}^D$, there are open loops described by Eq. (52) with an arbitrary value of ℓ [12]. The open Wilson loops on $\mathbb{T}^D$ are invariant about the noncommutative gauge transformations only for discrete $\mathbb{T}^D$ values that are multiples of $\pi\theta/l$ [14]. The closed Wilson loops appear in the representation of the average $\langle\phi^*(x) * \phi(x)\rangle_\phi$ as a path sum. The open Wilson loops appear for $\langle\phi^*(x) * S_\ell(x) * \phi(x + \ell)\rangle_\phi$ [15]. For integer ratios $m/n = \tilde{p}$, the open Wilson loops in the noncommutative $U_\theta(1)$ gauge theory become the Pol'akov loops wound round a $\tilde{\mathbb{T}}^D$ torus in the Morita-equivalent Yang–Mills $U(p)$ theory with twisted boundary conditions.

D-BRANE INTERPRETATION [22]

The results concerning the Morita equivalence allow a simple interpretation as a T-duality transformation in terms of D-branes. Let us consider a twist of a more general type in $D = 4$, for which the $SU(p)$ group is represented in the form $SU(p) \supset 1_{\tilde{p}_0} \otimes SU(\tilde{p}_1) \otimes SU(\tilde{p}_2)$ ($p = \tilde{p}_0\,\tilde{p}_1\,\tilde{p}_2$). The simplest twist (11) considered above corresponds to $\tilde{p}_0 = 1$ and $\tilde{p}_1 = \tilde{p}_2 = \tilde{p}$.

Consider a system composed of $\tilde{p}_0$ $D3$-branes populated by $\tilde{p}_0\,\tilde{p}_1$ $D1$-branes localized in the plane 1–2, $\tilde{p}_0\,\tilde{p}_2$ $D1$-branes localized in the plane 3–4, and $p = \tilde{p}_0\,\tilde{p}_1\,\tilde{p}_2$ D-instantons. This system corresponds to the noncommutative $U_\theta(\tilde{p}_0)$ gauge theory with dimensionless noncommutativity parameters equal to [23]

$$\Theta_{12} = \frac{\#D3}{\#D1} = \frac{1}{\tilde{p}_1}, \quad \Theta_{34} = \frac{\#D3}{\#D1} = \frac{1}{\tilde{p}_2}. \tag{54}$$

After the T-duality transformation in both 1–2 and 3–4 planes, we obtain a system composed of p $D3$-branes populated by $\tilde{p}_0\,\tilde{p}_1$ $D1$-branes oriented in the 1–2 plane, $\tilde{p}_0\,\tilde{p}_2$ $D1$-branes oriented in the 3–4 plane, and $\tilde{p}_0$ instantons. Now,

$$\tilde{\Theta}_{12} = \frac{\#D3}{\#D1} = \tilde{p}_1, \quad \tilde{\Theta}_{34} = \frac{\#D3}{\#D1} = \tilde{p}_2 \tag{55}$$

corresponds to magnetic fluxes in the ordinary $U(p)$ gauge theory. The matrix of periods becomes equal to $\tilde{\Sigma} = \mathrm{diag}(l/\tilde{p}_1, l/\tilde{p}_2)$ because of the presence of magnetic fluxes.

An interesting feature of the system obtained through the T-duality transformation is the presence of $\tilde{p}_0$ D-instantons. They provide zero topological charge, $Q = \#D3\#D(-1) - \#D1\#D1 = 0$, as it must be for this twist, because the action for the vacuum configuration is zero.

Note that the above interpretation of the Morita equivalence is only valid for the gauge field. Its extension to the case of fundamental matter is still lacking.

CONCLUSION

This work demonstrates how the noncommutative gauge theories arise from the twisted reduced models. In my opinion, the noncommutative gauge theories could have been discovered in the early 1980s, if the question had been answered at that time as to which quantum theory the TEK model corresponds to at finite N. Now we realize that it is the lattice noncommutative gauge theory.

At the present time, the use of the noncommutative gauge theories is associated with the description of the D-branes. In matrix theory [2, 3], D-branes are classical configurations satisfying Eq. (1). In the superstring theory, the noncommutative gauge theories appear [24] as effective action for D-branes in the Neview–Schwarz external field. The knowledge of the properties of the Yang–Mills theory and the reduced models is quite helpful in studying these theories.

One can also put the reverse question as to what new knowledge about the Yang–Mills theory and the reduced models we gain with the help of the noncommutative gauge theories. The first and quite evident answer is that the Yang–Mills theory in a box with twisted boundary conditions, which was suggested by t'Hooft [18] in connection with the confinement problem, is represented in the form of the TEK model with constraint (18). This theory is Morita-equivalent to the noncommutative gauge theory with a rational Θ value. However, the present-day understanding of the noncommutative gauge theories is still insufficient to assist in solving the confinement problem. In this connection, a multitude of new classical solutions [25–27] found recently in the noncommutative theories are of indubitable interest.

This work was supported in part by the Russian Foundation for Basic Research (project no. 97-02-17927).

REFERENCES

1. A. Connes, M. R. Douglas, and A. Schwarz, JHEP **9802**, 003 (1998); hep-th/9711162.
2. T. Banks, W. Fischler, S. H. Shenker, and L. Susskind, Phys. Rev. D **55**, 5112 (1997); hep-th/9610043.
3. N. Ishibashi, H. Kawai, Y. Kitazawa, and A. Tsuchiya, Nucl. Phys. B **498**, 467 (1997); hep-th/9612115.
4. K. L. Zarembo and Yu. M. Makeenko, Usp. Fiz. Nauk **168** (1), 3 (1998) [Phys. Usp. **41**, 1 (1998)].
5. T. Eguchi and H. Kawai, Phys. Rev. Lett. **48**, 1063 (1982).
6. G. Bhanot, U. M. Heller, and H. Neuberger, Phys. Lett. B **113B**, 47 (1982).
7. A. González-Arroyo and M. Okawa, Phys. Lett. B **120B**, 174 (1983).
8. T. Eguchi and R. Nakayama, Phys. Lett. B **122B**, 59 (1983).
9. A. González-Arroyo and M. Okawa, Phys. Rev. D **27**, 2397 (1983).
10. A. González-Arroyo and C. P. Korthals Altes, Phys. Lett. B **131B**, 396 (1983).
11. H. Aoki, N. Ishibashi, S. Iso, *et al.*, Nucl. Phys. B **565**, 176 (2000); hep-th/9908141.
12. N. Ishibashi, S. Iso, H. Kawai, and Y. Kitazawa, Nucl. Phys. B **573**, 573 (2000); hep-th/9910004.
13. I. Bars and D. Minic, hep-th/9910091.
14. J. Ambjørn, Y. M. Makeenko, J. Nishimura, and R. J. Szabo, JHEP **9911**, 029 (1999); hep-th/9911041.
15. J. Ambjørn, Y. M. Makeenko, J. Nishimura, and R. J. Szabo, Phys. Lett. B **480B**, 399 (2000); hep-th/0002158.
16. J. Ambjørn, Y. M. Makeenko, J. Nishimura, and R. J. Szabo, JHEP **0005**, 023 (2000); hep-th/0004147.
17. A. Schwarz, Nucl. Phys. B **534**, 720 (1998); hep-th/9805034.
18. G. 't Hooft, Nucl. Phys. B **153**, 141 (1979).
19. S. R. Das, Phys. Lett. B **132B**, 155 (1983).
20. Yu. M. Makeenko, Usp. Fiz. Nauk **143**, 161 (1984) [Sov. Phys. Usp. **27**, 401 (1984)].
21. S. Minwalla, M. Van Raamsdonk, and N. Seiberg, hep-th/9912072.
22. A. S. Gorsky and Y. M. Makeenko, unpublished.
23. R.-G. Cai and N. Ohta, JHEP **0003**, 009 (2000); hep-th/0001213.
24. N. Seiberg and E. Witten, JHEP **9909**, 032 (1999); hep-th/9908142.
25. N. Nekrasov and A. Schwarz, Commun. Math. Phys. **198**, 689 (1998); hep-th/9802068.
26. R. Gopakumar, S. Minwalla, and A. Strominger, JHEP **0005**, 020 (2000); hep-th/0003160.
27. D. J. Gross and N. A. Nekrasov, hep-th/0005204.

Translated by I. Rožzen

JETP Letters, Vol. 72, No. 7, 2000, p. 400.

Erratum: "Scaling Law for a Low-Pressure Gas Breakdown in a Homogeneous DC Electric Field" [*JETP Lett.* 72, 2, 34–37 (2000)]

V. A. Lisovsky and S. D. Yakovin

The name of the first author should read V. A. Lisovskiy.